

---

1 **This manuscript is a revised preprint** and has been re-submitted for publication in **Basin**  
2 **Research**. The current version covers two rounds of peer review but is **not yet accepted**  
3 **for publication**. Subsequent versions of this manuscript may differ due to additional peer  
4 review or the editorial process. If accepted for publication, the final version will be available  
5 through the “Peer-reviewed publication DOI” link on EarthArxiv.  
6 We hope you find this paper interesting and would welcome your feedback on it. Kindly  
7 contact Folarin Kolawole ([folarin.kol@gmail.com](mailto:folarin.kol@gmail.com)) with your feedback.  
8

---

9 **Rift Interaction Zones and the Stages of Rift Linkage in Active Segmented**  
10 **Continental Rift Systems**

11 Folarin Kolawole<sup>1,2\*</sup>, Max C. Firkins<sup>1</sup>, Thuwaiba S. Al Wahaibi<sup>1</sup>, Estella A. Atekwana<sup>3</sup>,  
12 Michael J. Soreghan<sup>1</sup>

13

14 <sup>1</sup>School of Geosciences, University of Oklahoma, 100 East Boyd Street, RM 710, Norman, OK 73019

15 <sup>2</sup>Now at BP America, 501 Westlake Park Blvd, Houston, TX 77079

16 <sup>3</sup>Department of Earth Sciences, University of Delaware, 101 Penny Hall, Newark, DE 19718

17

18 *\*Corresponding Author: Folarin Kolawole ([folarin.kol@gmail.com](mailto:folarin.kol@gmail.com))*

19

20

21 **Abstract**

22 Although much is known about the interaction of faulting and sedimentation within the  
23 basins of active segmented continental rift systems, little is known about these processes  
24 within the interaction zones of varying geometries that separate the young interacting  
25 segments. We address this problem in the humid, magma-poor juvenile western branch of  
26 the East African Rift System (WB-EARS). First, we present a broader classification of rift  
27 interaction zone (RIZ) geometries that accommodate both the plan-view geometries and  
28 border fault polarity patterns of the interacting rift segments. Within the framework of the  
29 RIZ geometries, we explore the large-scale cross-over relief profiles, and the relationships  
30 with the spatiotemporal development of rift-linking faults (breaching faults) and axial  
31 stream patterns. Our results show that: 1.) distinct long-wavelength 2-D cross-over  
32 topographic relief shapes, directionality of axial stream flow (sediment routing patterns),  
33 and breaching fault patterns characterize RIZs at the various stages of the linkage of  
34 interacting rift basins; 2.) these stages include unbreached, partially-breached, recently-  
35 breached, and breached RIZs; 3.) deforming RIZs exhibit different styles of directionality of  
36 breaching, including a unidirectional (distinct propagator and receiver segments), bi-

37 directional propagation (both segments act as propagators and receivers), and nucleation  
38 and outward propagation of a narrow intra-RIZ subsidiary rift basin; 4.) RIZ breaching is  
39 facilitated by overlap rift-flank deformation, and/or rift tip propagation structures in the  
40 form of rift splaying, border fault rotation (rift-tip rotation), and fault cluster networks; 5.)  
41 the lateral propagation of breaching faults at the rift tips and flanks, facilitated by localized  
42 stress concentrations, is modulated by the extension direction and inherited basement  
43 structures. Our findings offer a broader insight into the geometries and structural evolution  
44 of rift interaction zones, and provide first-order predictions of large-scale sedimentation  
45 patterns of humid early-stage continental rift environments. Our models provide testable  
46 hypotheses for linking rift architecture and patterns of early-stage sedimentation applicable  
47 to ancient rift basins.

48

49 *Keywords: Continental rifting; Rift interaction; Rift linkage; Normal faults; Sedimentation*

50

## 51 **1. Introduction**

52 Continental extension proceeds, first by the nucleation of discrete, isolated rift basin  
53 segments which subsequently propagate laterally towards one another and link-up to form  
54 continuous chains of rift basins (Figure 1, e.g., Nelson, et al., 1992; Corti, 2012; Allken et al.,  
55 2011, 2012; Zwaan et al., 2016; Molnar et al., 2019; Zwaan and Schreurs, 2020). The cross-  
56 over zone of mechanical interaction between the propagating rift segments and rift  
57 structures leading to rift segment linkage has been referred to by different terms, which  
58 include rift interaction zone (Nelson, et al., 1992; Zwaan et al., 2016), rift accommodation  
59 zone (Rosendahl, 1987; Faulds and Varga; 1998; Lambiase and Bosworth, 1995), transfer  
60 zone (Morley et al., 1990; Gawthorpe and Leeder, 2000; Corti, 2004; Aanyu and Koehn, 2011;  
61 Heilman et al., 2019), and graben stepover zone (Fossen et al., 2010). Here, we adopt the  
62 term “Rift Interaction Zone (RIZ)” to describe the large-scale region of rift segment  
63 interaction separating individual rift segments within a rift system (following the convention  
64 of Nelson, et al., 1992). Rift interaction zones typically host smaller-scale zones of fault  
65 interaction and strain transfer which are referred to as “transfer zones” or “accommodation  
66 zones” (Rosendahl, 1987; Morley et al., 1990, 1999; Faulds and Varga; 1998; Zwaan and  
67 Schreurs, 2020). In this study, we focus on the larger-scale zone of rift segment interactions  
68 (RIZs).

69 The initial localization and structure of rift interaction zones are determined by a variety of  
70 factors which include the inherited crustal mechanical anisotropies, variation in strain rate,  
71 extension direction, magmatic focusing, border fault and rift geometries etc. (e.g., Bosworth,  
72 1985; Morey et al., 1990; Acocella et al., 1999; Aanyu and Koehn, 2011; Corti, 2012; Heron et

73 al., 2019; Corti et al., 2019). However, rift segment interaction across deforming RIZs occurs  
74 in both the early (stretching) and later (necking and hyper-extension) stages of continental  
75 rift development (e.g., Aanyu and Koehn, 2011; Pagli et al., 2018; Heilman et al., 2019; La  
76 Rosa et al., 2019; Corti et al., 2019; Collanega et al., 2020). At continental break-up, major  
77 paleo-RIZs separating the offset segments of a rifted margin may influence the location of  
78 subsequent oceanic transform fault development (e.g., Cochran and Martinez, 1988; Behn  
79 and Lin, 2000).

80 Rift interaction zones of active segmented continental rifts are areas of relatively elevated  
81 basement which serve as viable source areas for sediment production and supply into the  
82 active rift basins which constitute domains of crustal subsidence (Lambiase and Bosworth,  
83 1995). In addition, rift interaction zones may accommodate intense tectonic stresses,  
84 seismicity, and magmatism associated with tectonic interactions between active rift  
85 segments that are in spatial proximity (Heilman et al., 2019; Corti et al., 2019).

86 Although climate and sea/lake level change play important roles in sedimentation along  
87 continental rifts, the tectonic deformations impose first-order controls on sedimentation  
88 patterns and stratigraphic architecture (e.g., Tiercelin et al., 1992; Lambiase and Bosworth,  
89 1995; Soreghan and Cohen, 1996; Soreghan et al., 1999; Hans Nelson et al., 1999; Gawthorpe  
90 and Leeder, 2000; Jackson et al., 2005; Mack et al., 2006). Within a given climatic condition,  
91 active tectonics impose significant controls on the localization of uplifted zones where  
92 erosion and sediment production occur, as well as on the localization of subsidence which  
93 serve as depocenters for sediment accumulation (e.g., Hovius, 1998; Gawthorpe and Leeder,  
94 2000; Barnes et al., 2011). Within these settings, the routing of sediments from the uplifted

95 areas into the depocenters are determined by the interplay between tectonic deformation  
96 (e.g., spatiotemporal fault interactions), climate, dominant agents of sediment weathering  
97 and transport, and base level change (e.g., Allen, 2008).

98 In evolving continental rift settings, the breaching and burial of cross-over basement-highs  
99 between interacting rift basins (RIZs) constitute the dominant signatures of rift linkage and  
100 transformation of closed rifts into open rift basins (Gawthorpe and Leeder, 2000). However,  
101 there is limited understanding of how the morphology of RIZs evolve with the progression  
102 of tectonic and breaching fault interactions between the flanking rift segment pairs. Also,  
103 there is a need to better understand how this evolution influences the patterns of sediment  
104 routing into the basins, the linkage of the depositional systems, and burial of the pre-existing  
105 basement-high of paleo-RIZs.

106 The first-order characteristic of zones of structural interaction is geometry (Nelson et al.,  
107 1992; Morley et al., 1990; Faulds and Varga, 1998). Therefore, the systematic assessment of  
108 the spatiotemporal evolution of a RIZ requires a consideration of its geometry. However, the  
109 existing geometrical classification of RIZs (Nelson et al., 1992) is inadequate because it does  
110 not encompass the variety of rift interaction zone geometrical patterns that are observable  
111 in several continental rift systems. In this study, first, we revise the existing classification of  
112 RIZ geometries and present a broader classification that provides a better framework for  
113 assessing structure and evolutionary stages of RIZs. Within the framework of the broader  
114 geometries, we investigate key aspects of the surface morphology and structure of non-  
115 magmatic RIZs along the juvenile, humid, magma-poor western branch of the East African  
116 Rift System (WB-EARS; Figure 2). Our analyses assess the first order influence of fault

117 breaching and basin-ward denudation on the progressive deformation and burial of the RIZs,  
118 and the possible cross-over topographic relief geometries associated with each sequential  
119 stage of the RIZ evolution.

120

### 121 **1.1. Geologic Setting: The Western Branch of the East African Rift System (WB-EARS)**

122 The western branch of the Cenozoic East African Rift System (WB-EARS; Figure 2) is defined  
123 by a N-S-trending arcuate-shaped system of elongate rift basin segments separated by  
124 basement rift interaction zones, extending along the Proterozoic mobile belts separating  
125 Archean cratons to the east and the west (e.g., Daly et al., 1989; Corti et al., 2007). This rift  
126 system branch includes reactivated rift segments that had experienced the earlier phases of  
127 Mesozoic extension recorded in east Africa. However, the Cenozoic and Mesozoic rifting  
128 events were preceded by the Proterozoic continental accretion of the pre-rift basement. This  
129 Precambrian basement of eastern Africa is composed of Proterozoic orogenic belts that wrap  
130 around Archean cratonic blocks (Figure 2; Daly et al., 1989; FriRIZ et al., 2013). The rift  
131 system propagates along and across the orogenic belts that flank the Tanzanian Craton to  
132 the west, which include the Madi-Igisi, Ruwenzori, Ubendian, Kibaran, Irumide,  
133 Mozambique, and Zambezi Belts (Figure 2). These mobile belts are dominated by gneisses  
134 with granulite and amphibolite facies metamorphic rocks associated with terranes  
135 separated by steeply-dipping shear zones and suture zones (Daly et al., 1989).

136 In the Phanerozoic, eastern Africa experienced at least three phases of continental extension.  
137 These phases include the Permo-Jurassic 'Karoo' rifting, Cretaceous rifting, and the currently  
138 ongoing Cenozoic phase of rifting (Delvaux, 1989). Some of the currently active segments

139 witnessed the Karoo phase of rifting and were reactivated during the subsequent rifting  
140 episodes (e.g., Rukwa, North Malawi, Shire, Luano, and Luangwa Rifts in Figure 2). The  
141 Cenozoic rift segments that make up the WB-EARS define a juvenile rift system (<25 Ma;  
142 Roberts et al., 2012) extending from the Rhino Rift at its northernmost tip (where the rift  
143 system terminates against the NW-trending Precambrian Aswa Shear Zone), southwards  
144 through the Malawi Rift, Luangwa, Kundelungu, Mweru, and Kariba Rifts (Figure 2). The  
145 southern portions of the western branch (e.g., Luangwa, Kundelungu, Mweru, Mweru-  
146 Wantipa, Upemba, and Kariba Rifts) are also referred to as the ‘southwestern’ segments of  
147 the rift system (Daly et al., 2020). In this paper, for simplicity, we consider these  
148 ‘southwestern’ rift segments to be part of the WB-EARS.

149 The WB-EARS yet remains an enigma, as it is largely magma-poor and its segments have  
150 accommodated multiphase crustal stretching since Mesozoic times (Delvaux, 1989; Specht  
151 and Rosendahl, 1989; Morley et al., 1999; Simon et al., 2017; Muirhead et al., 2018; Wright  
152 et al., 2020). The WB-EARS is currently characterized by a maximum crustal stretching rate  
153 of 2.9 mm/yr which is lower in comparison to that of the largely magma-rich eastern branch  
154 (up to 5.2 mm/yr) of the East African Rift System, (EB-EARS; Saria et al., 2014). A few  
155 magmatic centers occur along the WB-EARS and primarily at the rift interaction zones  
156 (Rungwe Volcanic Province (RVP), South Kivu Volcanic Province (SKVP), Toro-Ankole  
157 Volcanic Province (TAVP), Virunga Volcanic Province (VVP) in Figure 2). However, most of  
158 the interaction zones are generally non-magmatic, showing no evidence of surface  
159 volcanism. The absence of surface volcanism in several of the WB-EARS interaction zones  
160 present a ‘simpler’ setting (i.e., one less tectonic variable) to explore the first-order dynamics  
161 of early-rift linkage that characterize the growth of continental rifts and break-up process.

162

163 **2. Data and Methods**

164 Individual rift zones (single or coalesced segments) represent discrete tectonic elements  
165 within a rift system, which interact spatially when in proximity to one another. Since active  
166 rift basins are zones of active tectonic subsidence, and the intervening cross-over region  
167 separating the rifts prior to linkage (rift interaction zone, RIZ; Figure 1) are regions of  
168 relatively elevated basement, the linkage of the interacting rifts would require progressive  
169 faulting, tectonic subsidence, erosion, and burial of the RIZ cross-over region.

170 For a satisfactory assessment of the temporal evolution of rift linkage in an active continental  
171 rift system as the EARS, we first evaluate the existing classifications of RIZ by examining the  
172 East African Rift system and other continental rift systems to create a more robust and useful  
173 classification scheme. This updated classification scheme provides a basis for delineating the  
174 spatial extent of cross-over region for various RIZ geometries (pink polygons in Figure 3)  
175 within which the assessment of breaching structures and cross-over topography can be  
176 carried out.

177 To assess the status of the rift linkage at paired RIZs, we investigate the large-scale patterns  
178 of active faulting and cross-over relief profiles across the RIZs. More specifically, we evaluate  
179 the similarities and differences in the general patterns of the large-scale cross-over  
180 topographic morphology of the non-magmatic RIZs along the WB-EARS (Figure 4a) to  
181 identify the prominent trends (e.g., Figures 4b-g). Furthermore, we analyze four  
182 representative RIZs that span the possible stages of rift linkage (unbreached, partial  
183 breaching, recent breaching, and breached) and contrast the interactions between the

184 tectonic structures and drainage systems in each case. In addition, since the linkage of  
185 interacting rifts commonly transforms initially closed rift basins into open basins  
186 (Gawthorpe and Leeder, 2000), we extend our assessments to include the first-order trends  
187 and geomorphic characteristics of the axial streams that have catchment areas in the RIZs,  
188 and/or axial streams that flow across the lengths of the RIZs where observable.

189

### 190 **2.1. Cross-Over Topographic Relief Profiles and Axial Stream Morphology**

191 We created topographic profiles of the RIZs from the grids of the Global Multi-Resolution  
192 Topography (GMRT) data (Ryan et al., 2009). The terrestrial component of the GMRT data  
193 (used in this study) has a spatial resolution of  $\sim 30$  m. To assess the long-wavelength cross-  
194 over topographic geometries of the RIZs, we plot topographic profiles extending between  
195 the interacting rift segment pairs, parallel to and orthogonal to the RIZs where appropriate.  
196 We present the long-wavelength 2-D cross-over profiles by both the moving average of the  
197 30 m resolution GMRT data, and a profile of resampled GMRT grid (resampled to 4 km  
198 resolution). The selection of the localities of the longitudinal topographic profiles are  
199 primarily based on the large-scale structure of the examined RIZs. If there exists a zone of  
200 fault-bounded valleys linking the interacting rifts (observable on the hillshade topographic  
201 and fault maps), we extend the profile through the zone such that each end of the profile is  
202 in the axis of one of the two interacting rift basins. If there is no observable linking fault-  
203 bounded valley in the RIZ, we place the topographic relief profile at any arbitrary location  
204 across the RIZ but ensuring that the two ends of the profile are in the axes of the rift basins.

205 Due to the unique geometry of overlapping parallel RIZs, we orient the topographic profiles  
206 in an across-strike manner (orthogonal to the longitudinal trend of the RIZ).

207 We emphasize here that in all the WB-EARS RIZs examined in this study, there is no  
208 significant large-scale variation in the erodibility of the pre-rift basement lithologies as the  
209 areas are primarily dominated by amphibolite-grade gneisses and granulites. In certain  
210 areas, the metamorphic basement rocks have been intruded by pre-EARS igneous ring  
211 complexes which show more resistance to erosion relative to the gneisses (e.g., Southern  
212 Malawi Rift; Nyalugwe et al., 2019a). However, the locations of these igneous intrusions are  
213 known, and they are also easily identifiable in the topographic hillshade and aeromagnetic  
214 maps. In addition, the intrusions define short-wavelength structures and do not influence  
215 the long-wavelength geometries of the important longitudinal topographic relief profiles  
216 examined in our study areas. In areas where our profiles intersect the intrusions (e.g., across-  
217 rift topographic profiles in Southern Malawi Rift), the intrusions are mostly at the rift margin  
218 (border fault domain) and not along the flow path of the axial stream.

219 To investigate the relationships between the RIZ cross-over topographic relief geometry and  
220 the large-scale sediment routing patterns into the interacting rift basins, we plot the  
221 longitudinal profiles of rift axial streams (permanent streams) that have catchments in the  
222 RIZs using elevation data from the GRMT grid. Although both the axial streams and their  
223 tributaries provide sediments from the deforming and eroding RIZ basement-high into the  
224 subsiding rift basins, we envision that the large-scale directionality of axial stream flow will  
225 more likely be controlled by the slope at the flanks of the RIZs.

226 The surface textures of the GMRT hillshade digital elevation model (DEM) maps can help  
227 delineate the locations of recent alluvial sediment accumulation and areas of crystalline  
228 basement exposures (Drury, 2001). Areas characterized by smooth textures on the DEMs are  
229 interpreted as depositional surfaces reflecting primarily sediment accumulation and  
230 aggradation, with erosion or gullyng possibly present, but at a spatial scale lower than the  
231 DEM resolution. Areas characterized by rougher textures on the DEM are interpreted as  
232 regions of crystalline basement exposures where erosion dominates and produces  
233 topographic relief on spatial scales greater than the pixel spacing of the DEM. Thus, to  
234 delineate and map areas of subsidence and alluvial sediment accumulation at the  
235 propagating tips of the active rift segments, we combine DEM hillshade maps and published  
236 surficial geology maps of the study areas (e.g., Choubert et al., 1988). Further, we identify the  
237 dominant border fault of a rift segment as the rift-bounding fault that is in the direction of  
238 the downward tilt of the basin. Where available, we determine the border fault segments  
239 from published seismic reflection images constrained by well log correlation (e.g., Albertine-  
240 Rhino RIZ). However, in areas where such subsurface data are absent, we determine the  
241 direction of basin tilt from the overall direction of slope of the hanging wall of the basin  
242 surface (e.g., Mack et al., 2006).

243

#### 244 *2.1.1. Stream Sinuosity and Channel Width*

245 In humid continental settings such as the WB-EARS, the linkage of rift basin segments will  
246 involve a transformation of at least a part of the RIZ cross-over basement-high (having  
247 significant surface slope gradients at the flanks prior to linkage) into a continuous valley

248 floor with significantly lower surface slope gradient after linkage. Since surface slope  
249 patterns fundamentally control important geomorphic stream elements such as sinuosity  
250 (Lazarus and Constantine, 2013), we assess the patterns of sinuosity along the relevant axial  
251 streams.

252 Our study involves areas of basement exposure and burial along the rift floor near the  
253 interacting rift segment tips, therefore, we quantify the variation of the channel width along  
254 the axial streams to examine some aspects of the influence of rift-floor basement exposure  
255 and RIZ faulting on the large-scale geomorphology of the axial streams within some of the  
256 RIZs (e.g., see South Malawi–Shire and Albertine-Rhino RIZs). Since the South Tanganyika-  
257 Rukwa RIZ is a parallel RIZ we examine two major streams (Kalambo and “R1” Rivers) that  
258 although are not ‘axial’ to the interacting rifts, are equally relevant to the study as they both  
259 initially flow parallel to the RIZ before deflecting into the interacting basins.

260 We manually digitized the active axial streams analyzed in the representative RIZs, and  
261 manually measured the stream widths (perpendicular to the stream channel) at regular  
262 intervals along the stream channels using ArcMap© and Google Earth© satellite images.  
263 However, due to the difference in the complexity of channel geometry between the study  
264 areas (i.e., intensity of channel meandering, presence or absence of braided or anastomosing  
265 sections), we varied the intervals used. We obtained measurements at 2 km regular intervals  
266 in the Tanganyika - Rukwa RIZs (Kavuu and Luegele Rivers; cumulative stream length of 300  
267 km), 4 km regular intervals in the South Malawi - Shire RIZ (Shire River; total stream length  
268 of 200 km), and 1 km regular intervals in the Albertine - Rhino RIZ (Albert Nile River; total  
269 stream length of 105 km). At the braided or anastomosing stream segments, we measure the

270 width of the widest active channel. We estimate channel sinuosity of major segments of the  
271 axial streams using standard approach. To further assess the axial stream morphology  
272 anomalies where relevant, we utilize color composites of Landsat TM optical satellite images  
273 obtained from the USGS Earth Explorer database.

274

## 275 **2.2. Mapping of Sub-aerial and Subsurface Tectonic Structures**

### 276 *2.2.1. Fault Mapping*

277 To assess the structural deformation in active continental rift interaction zones (i.e.,  
278 involving at least one active rift segment), there is need for a detailed mapping of both the  
279 surface and buried faults, as well as the pre-rift basement fabrics which often influence the  
280 patterns of brittle strain localization (e.g., Heilman et al., 2019). In active rift basins, sub-  
281 aerial mapping of faults from topographic hillshade maps and in the field are inherently  
282 limited because they typically only reveal the recent surface-breaking active fault segments,  
283 and are generally not able to delineate the buried active fault segments, which may be  
284 accommodating significant tectonic strain (e.g., Kolawole et al., 2018). However, commonly  
285 available geophysical datasets such as high-resolution aeromagnetic data provide  
286 subsurface imaging of both intra-sedimentary and basement-rooted normal faults (Grauch  
287 and Hudson, 2007; Kolawole et al., 2018). Due to the deep-penetrating nature of potential  
288 field geophysical signals, aeromagnetic data allows us to discriminate between non-  
289 penetrative surface features (such as river and paleo-lake terraces) and mega-scale  
290 penetrative structures such as faults and mega-fractures. Unlike the mega-scale penetrative  
291 brittle deformation, non-penetrative geological features do not create discontinuity

292 lineaments that offset or disrupt the lateral continuity of basement fabrics at the resolution  
293 of the aeromagnetic datasets utilized in this study.

294 In the representative RIZs analyzed in this study, we utilize the GMRT hillshade DEM and  
295 previously published fault maps to delineate the sub-aerial fault segments. For subsurface  
296 fault mapping, we evaluate previously published subsurface fault maps and update the maps  
297 with subsurface fault interpretations from our filtered high-resolution aeromagnetic maps.  
298 For example, in the Tanganyika - Rukwa RIZs, we include and update the previously  
299 published surface fault lineaments mapped from satellite topographic hillshade maps and  
300 field observations (Delvaux et al., 2012; Muirhead et al., 2018). In the Southern Malawi -  
301 Shire RIZ, we include and update previously published surface fault lineaments mapped from  
302 satellite topographic hillshade maps and field observations (Wedmore et al., 2020). Also, in  
303 the Albertine - Rhino RIZ, we include and update the previously published fault lineaments,  
304 some of which were mapped from topographic hillshade maps, seismic reflection datasets,  
305 and in the field (GTK Consortium, 2012; Westerhof et al., 2014; Katumwehe et al., 2015;  
306 Simon et al., 2017). Therefore, in each of the three representative RIZs analyzed in this study,  
307 we identify several subsurface fault segments that are absent in previous publications, and  
308 present updated fault maps which enable a detailed structural evaluation of the RIZ  
309 deformation.

310

### 311 *2.2.2. Mapping of Pre-rift Basement Fabrics*

312 In addition to fault mapping, we utilize the filtered aeromagnetic maps to image and  
313 delineate the sub-aerial and buried pre-rift basement fabrics within the representative rift

314 interaction zones in order to better understand the controls on the breach faulting. In the  
315 study areas, the pre-rift basement is metamorphic, dominated by gneisses and granulites  
316 with mappable foliation trends (Figure 2). In the Tanganyika – Rukwa RIZ, SW Tanzania, we  
317 use an aeromagnetic grid of 250 m spatial resolution, collected between 1977-1980 with  
318 flight height of 200 m and a flight line spacing of 1 km (Supplementary Figure S1). The  
319 Tanzanian aeromagnetic data was provided by the South Africa Development Council  
320 (SADC). In the Southern Malawi – Shire RIZ, we utilize a 62 m-resolution aeromagnetic grid,  
321 acquired in 2013 at a flight height of 80 m and 250 m flight line spacing (Supplementary  
322 Figure S2). The southern Malawi data was provided by the Geological Survey of Malawi (also,  
323 freely obtainable from Interdisciplinary Earth Data Alliance, IEDA; Nyalugwe et al., 2019b).  
324 In the Albertine - Rhino RIZ, we utilize and update previously published basement fabric  
325 interpretations from aeromagnetic data (Supplementary Figure S3; Katumwehe et al., 2015,  
326 2016). Prior to structural interpretation, the Southern Malawi and SW Tanzania  
327 aeromagnetic grids were first reduced to the magnetic pole (RTP), and the NW Uganda  
328 aeromagnetic data reduced to the magnetic equator (RTE) in order to correctly locate the  
329 anomalies over their sources (Arkani-Hamed,1988). After the RTP and RTE corrections, we  
330 apply derivative filters to the grids to resolve the structural features following examples of  
331 Arkani-Hamed (1988), Ma et al. (2012), and Kolawole et al. (2018).

332 For our structural analyses, we generate rose diagrams of the frequency-azimuth  
333 distribution of the faults and basement fabrics. For multimodal distributions, we divide the  
334 data into their modal sets using the frequency minima; and for both the unimodal and  
335 multimodal plots, we calculate the circular vector mean and 95 % confidence interval for the

336 modal sets using the method of Mardia and Jupp (2009). All the frequency-azimuth plots are  
337 area-weighted.

338

### 339 **3. Results**

#### 340 ***3.1. Re-assessment of Rift Interaction Zone Geometries***

341 Based on our observations of relative geometries of rift segments along the East African Rift  
342 System and other continental rift systems, and an evaluation of previously published rift  
343 interaction zone classification (Nelson et al., 1992), we present a new classification of RIZ  
344 geometries (Figure 3). The terminologies adopted in our new classification are descriptive  
345 and refer to the large-scale geometries of the interacting rift segments. Further, where  
346 relevant, we include an additional term that accommodates a secondary geometrical or  
347 structural component e.g., border fault polarity, and transverse strike/oblique-slip faulting  
348 at rift tips.

349 In this new classification, we distinguish between paired rift transfer zones (involving only  
350 2 rift segments) and compound rift transfer zones (involving more than 2 rift segments). For  
351 paired rifts, we account for tip-to-tip, overlapping, and underlapping rift patterns of parallel,  
352 oblique, and orthogonal trends of interacting rift pairs (Figure 3). Also, for compound RIZs,  
353 we account for triple junction (i.e., involving 3 rift segments) and quadruple junction (i.e.,  
354 involving 4 rift segments) geometries. Further, we show three possible sub-categories of  
355 quadruple junction RIZs in which the adjacent rift segments make oblique or orthogonal  
356 angles, or a combination of both with one another. In each class of RIZ geometry, we illustrate  
357 the possible lateral extents of the cross-over region. In Oblique Quadruple Junction RIZ, all  
358 the adjacent rift segments make oblique angles with one another. In Orthogonal Quadruple  
359 Junction RIZ, all the adjacent rift segments make orthogonal angles with one another.  
360 Whereas, in the Complex Quadruple Junction, some of the adjacent rift segments make  
361 oblique angles with other, whereas the others make orthogonal angles.

362 Based on our new classification scheme for paired rift segments, we define profile transects  
363 across the inter-rift cross-over regions in order to assess the general patterns of the RIZ relief  
364 geometries. The following section present our observations of the general patterns of the  
365 relief geometries.

366

### 367 ***3.2. Cross-Over Topographic Relief Profiles of Non-Magmatic Rift Interaction Zones*** 368 ***along the Western Branch of the East African Rift System (WB-EARS)***

369 Long-wavelength cross-over topographic relief profiles across the non-magmatic RIZs of  
370 different RIZ geometries in the WB-EARS (Figure 4a) exhibit a variety of shapes that can be  
371 broadly grouped into four major categories (Type-1 to Type-4) and a sub-category (Type-3-  
372 4). We refer to the major categories as Type-1 to Type-4 morphologies (Figures 4b-f). The  
373 Type-1 morphology is characterized by high relief; a topographic-high surface, flanked on  
374 both sides by generally steep slopes that transition into topographic-low surfaces of the  
375 interacting rift segments (e.g., Figure 4b). Examples of the Type-1 morphology include the  
376 South Tanganyika–Rukwa (STR-RIZ; 8°S, 31.5°E), Kundelungu–Luapula (KL-RIZ; 10.25°S,  
377 27.75°E), and the Central Luangwa–Central Malawi (CLCM-RIZ; 12°S, 33.5°E) RIZs (see  
378 Figure 4a for the locations). The Type-2 morphology is characterized by less pronounced  
379 relief, but still exhibiting a topographic high surface flanked by a steeper slope on one side  
380 and a less steep slope on the other side of the high (e.g., Figure 4c). An example of the Type-  
381 2 morphology includes the North Tanganyika-Rukwa RIZ (NTR-RIZ; 6.25°S, 30.5°E).

382 The topographic profile with Type-3 morphology is characterized by an elevated upper  
383 surface that extends from the axis of one of the interacting rift segments. This surface ramps  
384 steeply down to a lower elevation surface in the adjacent segment (e.g., Figure 4d). Type-3  
385 morphology examples include the Southern Malawi–Shire (SMS-RIZ; 15.75°S, 34.75°E) and

386 the Zambezi-Kafue (ZK-RIZ; 16°S, 28.5°E) RIZs. Finally, the Type-4 morphology features a  
387 considerably flat topographic relief profile that extends between the axis of the two  
388 interacting rift segments (Figure 4f). Examples of Type-4 morphology includes the  
389 Albertine–Rhino (AR-RIZ or BRIZ; 2.7°N, 31.4°E), and the Shire-Urema (SU-RIZ; 16.85°S,  
390 35.35°E) RIZs.

391 However, we also observe another morphology type that has a form of Type-3 morphology  
392 but has more undulations on its ramp than the typical Type-3 morphology (Figure 4e). We  
393 dub this the ‘Type-3-4’ morphology. Except for the Upemba-Kundelungu RIZ (UK-RIZ; 9.15°S,  
394 26.75°E), we commonly observe this morphology at the RIZs where active EARS segments  
395 overlap and overprint unreactivated Karoo rift basins. Examples include the Ruhuhu–  
396 Malawi (RM-RIZ; 10.75°S, 34.75°E), Maniamba–Malawi (MM-RIZ; 12. 5°S, 34.8°E), and  
397 Luama–Tanganyika (LT-RIZ; 5.9°S, 29.2°E) RIZs (Figure 4a). Along the Type-3-4 relief  
398 profile, the unreactivated Karoo basin extends from the ramp into the elevated part of the  
399 RIZ topographic relief profile.

400 Below, we focus on representative Type-1 to Type-4 RIZs along the WB-EARS and present  
401 observations of the pre-rift basement fabrics, faulting patterns, and axial drainage patterns  
402 and anomalies. We focus on the STR-RIZ, NTR-RIZ, SMS-RIZ, and AR-RIZ, due to the presence  
403 of accessible datasets that are relevant to our investigation. Due to the change in the RIZ  
404 geometry along the Tanganyika - Rukwa Rift cross-over zone (caused by along-strike change  
405 in the Tanganyika Rift trend), we separate the RIZ into a northern (NTR-RIZ) and southern  
406 (STR-RIZ) domain.

407

408 **3.3. Representative Type-1 Morphology Rift Interaction Zone: The South**  
409 **Tanganyika-Rukwa Rift Interaction Zone (STR-RIZ)**

410 The STR-RIZ is an overlapping-parallel divergent RIZ that is located between the Rukwa rift  
411 and the NW-trending southernmost segment of the Tanganyika rift (Figure 5a). The RIZ  
412 cross-over region, known as the Ufipa Horst, is essentially the uplifted basement horst  
413 between the Ufipa Fault footwall and the adjacent Tanganyika Rift (Figures 5a-c). This RIZ  
414 has recorded significant seismic activity, ranging from  $M_w < 3.7$  up to  $M_w 7.4$  (Figure 5a;  
415 Vittori et al, 1997).

416

417 **3.3.1. Pre-rift Basement Fabrics and Rift Faulting in the STR-RIZ**

418 The metamorphic foliation (i.e., 'basement fabrics') of the STR-RIZ basement revealed in the  
419 filtered aeromagnetic grid (Figures 5b-c), show dominant NW-SE trends with  $148^\circ \pm 4.3$  mean  
420 orientation (Figure 5d). Likewise, mapped faults (Figure 5c) within the RIZ show the same  
421 prominent trend, with a mean of  $147^\circ \pm 3.2$  (Figure 5e). On a larger-scale, we observe that the  
422 trends of the South Tanganyika Rift and its east bounding faults, as well as trends of the  
423 Rukwa Rift, its west bounding fault (Ufipa Fault), and the Kanda Fault (major fault in the RIZ;  
424 Figure 5f) are parallel to the dominant NW-SE trend of the basement fabrics. However, this  
425 prominent structural trend is sub-orthogonal to the  $\sim 067^\circ$   $S H_{min}$  (Figures 5d-e). In this RIZ,  
426 we do not observe the presence of prominent cross-faulting that directly links the Rukwa  
427 and South Tanganyika Rift basins.

428

429 **3.3.2. Axial Stream Morphology in the STR-RIZ**

430 The axial streams within the RIZ (e.g., Kalambo(KIR), Momba (MR), Mfuizi (MfR), and R1  
431 Rivers) generally flow parallel to the long-axis of the RIZ and are confined to narrow valleys  
432 that are bounded by steep fault scarps (Profile P1; Figures 5a and 5f). Downstream, the  
433 streams change course and flow into the interacting rift segments of Lake Tanganyika (in  
434 Tanganyika Rift) and Lake Rukwa (in the Rukwa Rift) (Figures 5a and 5g). The longitudinal  
435 profiles of representative axial streams (Kalambo and R1, which flow in opposite directions)  
436 show steepening of the profile with associated waterfalls (e.g. Kalambo Waterfall) along both  
437 the eastern and western flanks of the RIZ. Additionally, at the flanks of the RIZ, the streams  
438 commonly show a significant decrease in channel width and sinuosity relative to the  
439 upstream sections that extend well into the RIZ (e.g., Kalambo River, Figure 5g).

440

### 441 ***3.4. Representative Type-2 Morphology Rift Interaction Zone: The North*** 442 ***Tanganyika-Rukwa Rift Interaction Zone (NTR-RIZ)***

443 The NTR-RIZ has an overlapping-oblique divergent geometry, and is located between the  
444 northwestern tip of the Rukwa rift and the central segment of the Tanganyika rift (Figures  
445 5a and 6a-b). Similar to the STR-RIZ, this northern RIZ has recorded significant seismic  
446 activity, including multiple  $M_w > 5.0$  events (Figure 5a).

447

#### 448 ***3.4.1. Pre-rift Basement Fabrics and Rift Faulting in the NTR-RIZ***

449 The basement fabrics of the NTR-RIZ show a dominant NW-SE trend observable on the  
450 aeromagnetic map (Figure 6a) with a mean of  $139^\circ \pm 5.2$  (Figure 6c). Also, the mapped faults  
451 in the RIZ (Figure 6b) show a prominent NW-trend with a mean of  $137^\circ \pm 3.4$  (Figure 6d),

452 parallel to the basement fabrics. The mean trends of both the basement fabrics and faults in  
453 this RIZ are slightly oblique to those of the South Tanganyika - Rukwa RIZ, suggesting an  
454 anticlockwise deflection in the trend of the structures. This deflection is apparent in the fault  
455 map of the RIZs (Figure 5a). In the region of STR-RIZ to NTR-RIZ transition, two prominent  
456 NE-dipping fault scarps, Ifume and Nkamba Faults (Figures 5a, 6a-b) extend from the  
457 northernmost segment of Ufipa Fault System into the hanging wall of the SW-dipping Mahale  
458 Fault in the Tanganyika Rift. The basement exposures along the hanging walls of the scarps  
459 suggest an absence of large fault displacement or subsidence. The Nkamba River (NR in  
460 Figure 5a) extends from a watershed divide in the footwall of the Ufipa Fault, flows westward  
461 across the fault scarps into Lake Tanganyika (Figure 5a). However, more importantly, we  
462 note that the Nkamba and Ifume fault scarps show similarity of dip direction with the Rukwa  
463 Rift's NE-dipping Ufipa Fault, antithetic to the Tanganyika Rift's Mahale Fault.

464 Overall, the faults within the NTR-RIZ form a network that extends northwestwards from  
465 the tip of the Rukwa Rift and links up with faults along the eastern boundary of the  
466 Tanganyika Rift (Figure 6b). The RIZ-orthogonal topographic profiles (Figures 6e-g) show  
467 that at the NW tip of the Rukwa Rift, the basin is defined by a broad sediment-filled valley  
468 (smooth DEM surface texture) bounded by a low-gradient ramp that transitions to low-relief  
469 rift shoulders (Profile P2; Figure 6e). Further northwest, into the RIZ (Profile P3; Figure 6f),  
470 the basin morphology is characterized by multiple narrow sediment-filled troughs (narrow  
471 zones of smooth DEM surface texture) bounded by steep fault scarps and higher relief  
472 shoulders.

473 Proximal to the Tanganyika Rift (Profile P4; Figure 6g), the surface morphology of the RIZ is  
474 characterized by ubiquitous basement exposures with rare occurrence of significant  
475 sediment accumulation (rougher DEM surface textures). Two moderate magnitude  
476 ( $M_w > 5.0$ ) earthquakes in the NTR-RIZ show strike-slip kinematics with at least one nodal  
477 plane trending parallel to the mean fault trend and mean basement fabric trend (Figures 5a,  
478 5d-e). However, near the Rukwa Rift tip, the events generally show oblique normal faulting  
479 (Figure 5a).

480

#### 481 *3.4.2. Axial Stream Morphology in the NTR-RIZ*

482 The Type-2 topographic morphology of the NTR-RIZ (Figure 6h) features a central  
483 topographic-high flanked to the northwest (towards the Tanganyika Rift) by a steep  
484 escarpment, and to the southeast by a gentle slope that extends into the axis of the Rukwa  
485 Rift. Several humps and steps occur along the gentle slope and are collocated with the  
486 prominent NE-SW trending ridges (Figure 6h) that were formed by paleo-shorelines of Lake  
487 Rukwa (Figure 5a; Delvaux et al.,1998).

488 Within the RIZ, the axial streams (Kavuu (KR) and Luegele (LR) Rivers) diverge away from  
489 the central topographic-high (shared catchment region) and drain into the interacting rift  
490 basins (Figure 6h). The Luegele River flows northwest over a distance of ~55 km and drains  
491 into the Tanganyika Rift. The Luegele River steepens at ~28-30 km along the profile (Figure  
492 6i) which is collocated with the steep escarpment that bounds the RIZ to the northwest.  
493 Within this steeper reach, the Luegele River is characterized by rapids (Luegele Rapids). We  
494 observe that although the channel width shows an abrupt decrease across the steep

495 elevation gradient, the sinuosity index of the channel shows an increase on the downslope  
496 segment of the river (Figure 6i). The Kavuu River flows southeastwards from the RIZ and  
497 drains into the Rukwa Rift (Figure 5a). Although the channel extends over a longer distance  
498 (> 260 km) and transects a gently sloping topography (Figure 6i), the sinuosity and width of  
499 the channel show systematic variations. Two prominent anomalies are observable on the  
500 stream profile; these include an abrupt elevation step that is collocated with the Ilyandi  
501 Ridge and a change to a steep gradient at the Maimba Ridge (Figure 6i). Furthermore, we  
502 observe that the Kavuu River attains peak sinuosity index (~1.58) and channel width just  
503 upstream of two of the ridges, the Ilyandi Ridge and Rungwa Ridge. Each of these ridges is  
504 located just downstream of a prominent small lake (e.g., Lake Katavi) or swamp (Figure 5a).  
505 However, overall, the sinuosity of the axial streams is higher than those of the STR-RIZ.

506

### 507 ***3.5. Representative Type-3 Morphology Rift Interaction Zone: The South Malawi-*** 508 ***Shire Rift Interaction Zone (SMS-RIZ)***

509 The SMS-TZ covers the region extending from the southernmost tip of the N-S-trending  
510 Malawi Rift (i.e., the Zomba Graben) and the eastern margin of the NW-SE-trending Shire Rift  
511 Zone (i.e., Lower Shire Graben) (Figures 4a and 7a). Based on the overall trend of the Malawi  
512 Rift relative to the Shire Rift, we describe this cross-over region to be an overlapping oblique  
513 divergent transfer zone.

514

#### 515 ***3.5.1. Pre-rift Basement Fabrics and Rift Faulting in the SMS-RIZ***

516 To better understand the distribution of metamorphic basement fabrics and faulting in the  
517 SMS-RIZ (Figures 7b-c), we analyze the structures in the northern and southern parts of the  
518 Zomba Graben separately. The North Zomba Graben is distal to the Shire Rift, and the South  
519 Zomba Graben is proximal. The metamorphic fabrics of the North Zomba Graben are defined  
520 by curvilinear magnetic fabrics (Figure 7b) trending NNE-SSW ( $014^{\circ}\pm 4.1$ ) (Figure 7di),  
521 parallel to the most prominent fault set (NNE-SSW,  $011^{\circ}\pm 5.4$ ; Figure 7dii). The secondary  
522 fault set (ENE-WSW,  $073^{\circ}$ ) corresponds to the ENE linking faults along the NNE-trending  
523 border faults. This secondary fault set also corresponds to the trend of a prominent ENE  
524 strike-slip fault to which the Shire River channel is aligned (blue arrows in Figure 7a and c),  
525 and which also aligns with a basement dike lineament and offsets the basement  
526 metamorphic fabrics (Figure 7b).

527 In the South Zomba Graben, the metamorphic fabrics show bimodal trends with NNE-SSW  
528 ( $029^{\circ}\pm 3.9$ ) and NW-SE ( $144^{\circ}\pm 4.2$ ) sets (Figure 7ei) in which only the NNE set shows strong  
529 correspondence to a prominent fault set (Figure 7eii). The faults in the South Zomba Graben  
530 show multimodal trends with NNE-SSW ( $023^{\circ}\pm 4.6$ ), NNW-SSE ( $164^{\circ}\pm 5.7$ ), and ENE-WSW  
531 ( $079^{\circ}$ ) (Figure 7eii). The border faults of the South Zomba Graben generally follow basement  
532 fabrics, and although most of the intra-basinal faults and fractures crosscut the pre-rift  
533 fabrics, some segments locally follow the basement fabrics (Figure 7c).

534 The border faults of the Zomba Graben exhibit synthetic geometry mostly prominent in the  
535 south Zomba Graben. In the northern Zomba Graben, the intra-basinal faults dominantly  
536 trend NNE-SSW, parallel to the trend of the graben (Figure 7dii). In the south Zomba Graben,  
537 intra-basinal deformation is characterized by a cluster of faults/mega-fractures (breaching

538 faults) generally trending NNW, and extend northwestward from the footwall of the Thyolo  
539 Fault, the border fault of the Shire Rift into the axis of the Zomba Graben (Figures 7a and 7c).  
540 The Thyolo Fault itself extends northwestwards, and in the region of overlap with the Zomba  
541 Graben, it rotates clockwise into a NNW-trend and continues as a mega-fracture through the  
542 axis of the Zomba Graben to link up with the western border fault system (Lisungwe Fault  
543 (LsF); Figures 7a and 7c).

544

### 545 *3.5.2. Basin Morphology and Axial Stream Morphology in the SMS-RIZ*

546 Within the SMS-RIZ (Figure 8a), the axial stream, the Shire River flows southward from Lake  
547 Malombe (Malombe Graben, Figures 8a-b), through the Zomba Graben and continues into  
548 the Shire Rift. The first-order trend of the Shire River is characterized by a systematic shift  
549 in the along-rift axial location of the stream. In the north (Malombe Graben), the river is  
550 located near the center of the rift (Figure 8c), whereas, in the North Zomba Graben, the river  
551 is located near the eastern border fault (Chingale Step Fault) (Figure 8d). From this location,  
552 the river deflects southwestwards such that its position is again at the rift axis within the  
553 central segment of the Zomba Graben (Figure 8e), but further south, is located near the  
554 western border fault of the graben (Lisungwe Fault, Figure 8f).

555 In addition, we observe that although the Malombe Graben is characterized by a graben  
556 (Figure 8b) to asymmetric graben (Figure 8c) geometries, the Zomba Graben presents an  
557 along-rift flip in the polarity of the basin morphology. In the North Zomba Graben the  
558 direction of the tilt of the basin is eastward (green arrow in Figure 8d) but flips to a westward  
559 tilt in the southern part of the rift (green arrow in Figures 8e-f). Essentially, the variations in

560 the along-rift location of the Shire River are consistent with the along-rift change in the  
561 polarity of the basin and location of the dominant border fault.

562 We also observe that the morphology of the Shire River transitions from a relatively flat  
563 elevation profile upstream within the Malombe Graben and North Zomba Graben (Upper  
564 Shire River), through a steep profile in the South Zomba Graben (Middle Shire River), to a  
565 flat topography in the Shire Rift (Lower Shire River; Figure 8g). Along the Upper Shire River,  
566 the channel width mostly varies between 33 - 187 m with a sinuosity index of  $\sim 1.17$  but  
567 decreases significantly to 15 - 130 m channel width and 1.04 sinuosity index in the Middle  
568 Shire River. Along the Lower Shire River, both the channel width and sinuosity index  
569 increase to values much higher than those of the Upper Shire River (60 - 215 m channel  
570 width and 1.28 sinuosity index; Figure 8g). Although the Upper Shire River is generally  
571 sinuous and curvilinear in geometry (Figure 8a), there exists two prominent localized zones  
572 of significantly high sinuosity patterns where the river exhibits anastomosing characteristics  
573 (anastomosing sections in Figures 8a and 8h). Whereas, the Middle Shire River exhibits  
574 major rectilinear and orthogonal geometries, some of which align with mapped fault and  
575 mega-fracture lineaments (e.g., Figure 8i). The Lower Shire River is highly sinuous  
576 throughout its length as it flows on the hanging wall of the Thyolo Fault (e.g., Figure 8j).

577

### 578 **3.6. Representative Type-4 Morphology Rift Interaction Zone: The Albertine-Rhino** 579 **Rift Interaction Zone (AR-RIZ, a.k.a. BRIZ)**

580 The AR-RIZ is defined by the NNW-trending Butiaba RIZ (BRIZ) which is located between the  
581 NE-trending Albertine Rift to the south and the NE-trending Rhino Rift to the north (Figures

582 4a and 9a). This RIZ, also known as Pakwach Basin (Zwaan et al., 2016), is an underlapping  
583 parallel divergent RIZ.

584

### 585 *3.6.1. Pre-rift Basement Fabrics and Rift Faulting in the BRIZ*

586 Within the BRIZ, the basement fabrics show a prominent ENE-WSW trend ( $066^{\circ}\pm 9.3$ ), with  
587 secondary NE-SW ( $033^{\circ}\pm 9.3$ ) and E-W ( $094^{\circ}\pm 8.0$ ) trends (Figure 9b). However, we observe  
588 that the BRIZ faults dominantly strike NNE-SSW ( $027^{\circ}\pm 5.4^{\circ}$ ), oblique to the trend of the RIZ  
589 (Figure 9c). Faulting in the BRIZ is characterized by two main fault networks, both of which  
590 extend from two of the three prominent splay faults at the northern tip of the Bunia border  
591 fault of the Albertine Rift (“Splay-1, -2, & -3” in Figure 9a). The westernmost strand (Splay-  
592 1) connects to a network of short tightly clustered en-echelon faults, bounding the BRIZ to  
593 the west and southwest which extends northwards to link up with the western border fault  
594 of the Rhino Rift (Figure 9a). The central splay (Splay-2) continues north into the Ragem  
595 Fault, which appears to be the most prominent fault within the BRIZ. The Ragem Fault extend  
596 across the BRIZ into the footwall of the eastern border fault of the Rhino Rift. The  
597 easternmost splay (Splay-3) also extends across the BRIZ and is linked up with the Ragem  
598 Fault through the Panyango Fault. Overall, fault segments of Splay-3 appear to bound the  
599 BRIZ to the east and northeast (Figures 9a and 9e). In the Rhino Rift, the northern  
600 termination of the border fault systems occur at the NW-trending Precambrian Aswa Shear  
601 Zone (Figure 9a).

602

### 603 *3.6.2. Basin Morphology and Axial Drainage Patterns in the BRIZ*

604 The Albert Nile and Victoria Nile Rivers represent the major axial drainage systems of the  
605 Albertine Rift. However, the Albert Nile River is the primary axial drainage system that  
606 drains both the Albertine and Rhino Rifts, and the BRIZ between them (Figure 9a). Although  
607 the first-order trend of the Albert Nile River is generally sub-parallel to the trend of the RIZ,  
608 we observe that the along-rift locations of the river are collocated with the dominant border  
609 fault locations. The river flows northwards from the Lake Albert which is bounded by the  
610 border faults of the Albertine Graben (Figures 9a and 9d). In the BRIZ, the basin surface  
611 morphology shows a consistent northeastward-tilt, and the Albert Nile channel flows along  
612 the northeastern boundary of the RIZ (Figure 9a, 9e, and 9f). Within the Rhino Rift, the basin  
613 morphology is characterized by a southeastward-tilt (towards the Rhino Fault), and the  
614 Albert Nile flows along the hanging wall of the Rhino Fault (Figures 9a and 9g). Further north,  
615 closer to the rift termination at the Aswa Shear Zone, the river deflects towards the  
616 northwestern border fault (Figure 9a).

617 Overall, the entire longitudinal elevation profile of the Albert Nile River describes a relatively  
618 'flat' topography with very wide segments (77 – 1,800 m width) characterized by large  
619 meanders and highly anastomosed morphology (Figure 10a-10e). We observe two broad  
620 partitions on the Albert Nile River morphology profile which consists of a northern and  
621 southern partition, separated by the Ragem Fault (Figures 10a and 10b). The southern  
622 partition consists of a single wide channel within a relatively narrower valley, featuring  
623 sparse anastomosing sections with wide stream branches (Figures 10a, 10b, 10c, 10d). The  
624 northern partition is characterized by a wider river valley of continuously anastomosing  
625 river segments with narrow stream branches and a high density of lakes (Figures 10a, 10b,  
626 10e). The morphology of the northern partition of the river extends along most of the entire

627 length of the Rhino Rift. On the hanging wall of the Ragem Fault, the river valley defines a  
628 roughly fault-parallel (NNE) trend, whereas, in the footwall of the fault, the river valley  
629 rotates into a fault-perpendicular (NNW) trend (Figure 10b).

630 Additionally, we observe an abrupt narrowing of the river channel across the Ragem Fault  
631 such that a wide lake (1.35 km-wide) ponds within the hanging wall of the fault and drains  
632 into a narrow (~300 m-wide) channel on the footwall of the fault (Figures 10a, 10b and 10d).  
633 Similarly, where the river crosses the Rhino, Panyango and Bunia Splay-3 faults, there is a  
634 change in the width of the river such that the wider sections occur on the hanging wall of the  
635 faults (Figures 10a, 10b-c, and 10e).

636

## 637 **4. Discussion**

### 638 **4.1. A New and Broader Classification of Rift Interaction Zones**

639 The existing geometrical classification of RIZs (Nelson et al., 1992) is useful, but is  
640 significantly lacking in that it does not encompass the variety of RIZ geometrical patterns  
641 that can be observed in modern continental rift systems. Also, the existing scheme is overly  
642 simplistic, and only considered the plan-view rift geometries (Nelson et al., 1992). The  
643 classification does not permit the analyses of complexities arising from multiphase extension  
644 with varying extension directions, and generally ignore the possible temporal evolution from  
645 one RIZ geometry into another. Here, we establish a unifying broader classification scheme  
646 that accommodates the plan-view geometries, polarity patterns (dip direction) of the large  
647 basin-bounding faults (border faults), and temporal transformation of the RIZ geometries  
648 (Figure 3).

649 Our new classification scheme features both paired rift RIZs (involving only 2 rift segments)  
650 and compound rift RIZs (involving >2 rift segments). Along the WB-EARS (Figure 4a), a few  
651 examples of the geometries shown in the new scheme include: Tip-to-tip collinear (Rukwa-  
652 North Malawi), Overlapping parallel divergent (Upemba-Kundelungu, Kundelungu–Luapula,  
653 South Tanganyika – Rukwa RIZs), Overlapping orthogonal divergent (Tanganyika-Mweru  
654 Wantipa RIZ), Overlapping oblique divergent (South Malawi-Shire and Luama–Tanganyika  
655 RIZs), Complex quadruple junction (Rukwa-Luangwa-North Malawi–Usangu RIZ).

656 In other continental rift systems, examples include Overlapping oblique divergent  
657 (Wetterau–Leine RIZ, European Cenozoic Rift System), Tip-to-tip oblique (South Viking–  
658 Witch Ground RIZ, North Sea Rift), Overlapping parallel divergent (Utsira High, North Sea  
659 Rift; Limagne–Bresse RIZ, European Cenozoic Rift System), Overlapping oblique convergent  
660 (Española–San Luis RIZ, Rio Grande Rift), Overlapping parallel convergent (Albuquerque–  
661 Española RIZ, Rio Grande Rift), Overlapping orthogonal divergent (Lower Rhine–Upper  
662 Rhine RIZ, European Cenozoic Rift System), and Underlapping parallel divergent (Upper  
663 Rhine-Bresse RIZ, European Cenozoic Rift System). All the overlapping parallel RIZs in the  
664 different continental rift settings examined show an x-offset rift axes separation <150 km,  
665 consistent with recent models (Neuharth et al., 2021) which suggest a limit of 300 km x-  
666 offset distance beyond which overlapping rift segments will likely not interact.

667 For each category of RIZ, we show the lateral extents of the cross-over region across which  
668 the breaching faults would develop and propagate. Also, we indicate the possible variations  
669 of the breaching distances across the cross-over regions, indicating the areas within the  
670 cross-over region where relatively shorter distances of fault propagation could facilitate

671 breaching. We note that the configuration of some of the RIZ geometries suggest a possible  
672 temporal transformation from one geometry to another. For example, in paired RIZs,  
673 depending on the boundary conditions (e.g., underlapping distance, extension direction,  
674 inherited structures), with continued extension, unfaulted underlapping RIZs can evolve into  
675 an overlapping geometry or faulted underlapping geometry (see modelling results in Allken  
676 at al., 2012; Zwaan and Schreurs, 2020). Also, stress rotation between rifting episodes in  
677 multiphase rift settings can lead to the transformation of a paired RIZ geometry into a  
678 compound RIZ geometry; an example of which is the Turkana Depression (Fairhead, 1988;  
679 Emishaw et al., 2019; Morley, 2020; Wang et al., 2021).

680 Most numerical and analog models of rift linkage have been limited in scope because they  
681 only investigated parallel RIZs (underlapping and overlapping parallel RIZs, e.g., Acocella et  
682 al., 1999; Corti, 2004; Allken at al., 2011, 2012; Zwaan et al., 2016; Zwaan & Schreurs, 2017,  
683 2020). An example of this limitation is the assumption that the Rukwa Rift represents a  
684 strike-slip strain transfer zone between the Tanganyika Rift and Malawi Rift (e.g., Zwaan &  
685 Schreurs, 2017) even though faults of the Rukwa Rift largely exhibit normal faulting  
686 kinematics (e.g., Morley et al., 1999; Morley, 2010; Lavayssière et al., 2019). Although models  
687 successfully reproduce the temporal transformation from a type of parallel RIZ into another,  
688 there remains the need to consider the wider variety of RIZ geometries as shown in our  
689 updated classification scheme. Overall, we clarify that the geometries shown in our new  
690 scheme are most representative of early-stage continental extension, as the complexity of  
691 reactivation and structural deformation increases with the progression of continental  
692 extension towards break-up.

693 In the following sections, within the framework of our RIZ geometrical classification for  
694 paired rift segments, we analyze and discuss the detailed characteristics of four  
695 representative RIZs along the Western Branch of the East African Rift System (WB-EARS,  
696 Figure 4a). Based on the structural and morphotectonic characteristics of each of the cross-  
697 over regions examined, we infer the likely stage of evolution of the RIZ, the patterns of breach  
698 faulting and the basement controls.

699

#### 700 **4.2. Rift Interactions at the South Tanganyika-Rukwa RIZ (STR-RIZ)**

701 The STR-RIZ is an excellent example of Overlapping parallel divergent RIZ (Figures 2 and  
702 5a). The prominent topographic-high and steep flank morphology of the Ufipa Horst (Type-  
703 1 morphology, Figure 4b), and the presence of waterfalls and rapids on the flanks (Figures  
704 4b, 5f-g) suggest that the Ufipa Horst is actively uplifting along both of its flanks. This uplift  
705 is caused by both the isostatic footwall uplift of the Ufipa Fault and eastern Tanganyika Rift  
706 faults, and a mantle-driven dynamic topography (Morley et al., 1999; Heilman et al., 2019).  
707 However, even in the absence of the dynamic topography, the zone remains a zone of uplift  
708 between the subsiding rift segments, as shown in a flexural cantilever model of the rifts and  
709 rift flanks (Morley et al., 1999).

710 The clear correlation between the trends of basement metamorphic fabrics and faults within  
711 the Ufipa Horst, and sub-orthogonality to the SHmin orientation (Figures 5d-e) indicate the  
712 local influence of the pre-rift basement fabrics on fault geometry and strain accommodation  
713 within the RIZ. In addition, the near-orthogonal orientation of the extension direction  
714 relative to the dominant basement fabric trends (Figures 5a and 5d-e) implies that the

715 deformation of the RIZ could be accommodated by normal fault exploitation of the pre-rift  
716 basement fabrics. However, the complexity of kinematics of the deformation in the STR-RIZ  
717 is demonstrated by the prominence of Cenozoic oblique-normal and strike-slip faulting, with  
718 minor reverse faulting, possibly associated by local SH<sub>min</sub> rotation (Delvaux et al., 2012;  
719 Lavayssière et al., 2019).

720 The mapped faults are parallel to the long axis of the Ufipa Horst with no major graben  
721 system connecting the Rukwa and Tanganyika Rifts (Figures 5b-c), and the crust which  
722 appears to have been intruded by magma, is relatively thicker than those of the flanking rifts  
723 (Hodgson et al., 2017; Lavayssière et al., 2019). The deformation of this RIZ is relatively less  
724 pronounced in comparison to the overlapping parallel NLNM-RIZ where the North Rukuru-  
725 Mwesia Rift and Henga Rift (NRR and HR in Figure 4a) represent a RIZ-parallel deformation  
726 of the cross-over region (Ring, 1995). Likewise, it is less pronounced in comparison to the  
727 deformation of the N-S-trending Limagne–Bresse RIZ by the NNW-trending Roanne-Forez  
728 graben system in the European Cenozoic Rift System (Dèzes et al., 2004). The breaching of  
729 the NLNM-RIZ and Limagne–Bresse RIZ is represented by the development of a cluster of  
730 narrower en-echelon rift basins within the cross-over zone, in which the rift cluster is  
731 parallel or sub-parallel to the interacting major rift segments. Whereas another overlapping  
732 parallel RIZ, the UK-RIZ (Figure 4a) presents a different case of breaching by a transverse  
733 structure (here in referred to as the “Lufira Fault, LF” in Figure 4a) with well-developed  
734 sediment-filled valley (Choubert et al., 1988) and a through-going axial stream (Lufira River)  
735 which physically link the Upemba and Kundelungu Rift basins. The N-S/NNW trend of the  
736 Lufira Fault is compatible with the SH<sub>max</sub> rotation from NE-SW trend along the Upemba Rift  
737 to a N-S trend adjacent to the location of the Lufira Fault (Delvaux and Barth, 2010).

738 Therefore, the absence of any of the possible breaching structural patterns in the STR-RIZ  
739 suggests that the structural domain is partially deformed, and its breaching is not significant.  
740 The maximum separation distance between the Southern Tanganyika and Rukwa Rifts is <92  
741 km (Figure 5f). Analog models (e.g., Zwaan and Schreurs, 2020) show that within a  
742 separation distance of <300 km, rift segments will interact. Thus, it is possible that the  
743 observed faulting within the RIZ (e.g., the Kanda and Kalambo-Mwimbi Fault Systems) is  
744 being driven by the interaction between the two rift segments, a previously reported  
745 dynamic mantle-related uplift within the Ufipa Horst (Morley et al., 1999; Heilman et al.,  
746 2019), or both. Overall, our preferred interpretation is that the STR-RIZ is a partially  
747 breached RIZ.

748

#### 749 ***4.3. Rift Interactions at the North Tanganyika-Rukwa RIZ (NTR-RIZ)***

750 The NTR-RIZ represents an overlapping oblique divergent RIZ. The shape of the topographic  
751 relief profile extending from North Tanganyika Rift to Rukwa Rift (Figure 6h) shows that, in  
752 contrast to the steeper NW flank of the NTR-RIZ (Tanganyika Rift), the SE flank (towards the  
753 Rukwa Rift) is characterized by a longer stretch of gently sloping topography. Along this long  
754 stretch of gentle topography, the first-order axial stream trends are parallel to the fault and  
755 basement fabric trends (indicating large-scale control of tectonic trends).

756 Multiple narrow troughs develop at the NW tip of the Rukwa Rift passing into the NTR-RIZ,  
757 delineating a young rift splay (Figures 6b and 6f). The Nkamba and Ifume fault scarps (at the  
758 STR-RIZ/NTR-RIZ transition zone) also show an association with this rift splay, indicated by  
759 their common NE-dip with the Rukwa Rift's Ufipa Fault and their eastern terminations in the

760 footwall of the fault. The narrow troughs defined by the splays are bounded by actively  
761 propagating fault networks that extend northwest across the RIZ towards the eastern  
762 margins of the Tanganyika Rift. Thus, we interpret that the development of the Type-2  
763 topographic relief shape across the NTR-RIZ is influenced by a progressive northwestward  
764 propagation of the NW tip of the Rukwa Rift towards the Tanganyika Rift (Figures 6b and 6e-  
765 g). Whereas the relative steepness of the northern flank of NTR-RIZ 2-D cross-over relief  
766 profile (Figure 6h) reflects an absence of pronounced southeastward propagation of rifting  
767 from the Tanganyika flank of the NTR-RIZ.

768 Several of the mapped faults in the NTR-RIZ extend from the tip of the Rukwa Rift into the  
769 interior of the RIZ. However, our interpretation of the northwestward propagation of the  
770 Rukwa Rift is supported by the anomalous clustering of earthquakes at the NW tip of the rift  
771 which indicates that active crustal deformation is partitioned to the southeastern section of  
772 the NTR-RIZ (Figure 5a; see clustering of relocated earthquakes in Lavayssière et al., 2019).  
773 Also, The Ifume and Nkamba Faults, representing the most-western splay of the NW Rukwa  
774 Rift tip exhibit moderate earthquake clustering (Figure 5a; Lavayssière et al-2019),  
775 indicating tectonic activity along the faults. Overall, the NTR-RIZ faults represent the RIZ  
776 breaching faults and are accommodating a mix of strike-slip and oblique-normal slip  
777 kinematics (Figures 5a, 6b, and 6f; Lavayssière et al., 2019). Among these faults, the Ifume  
778 and Nkamba Faults, and the NW-trending Mw5-hosting faults along-trend of the Kavuu River  
779 likely constitute the master strain transfer faults between the two rifts.

780 We interpret that the NTR-RIZ is a partially breached RIZ, in which the Rukwa Rift is the  
781 active propagator, and the north Tanganyika Rift is the 'receiving' segment. The active

782 propagation of the Rukwa Rift tip is accompanied by splaying of the rift tip into multiple  
783 narrower troughs. The moderate magnitude strike-slip faulting ( $M_w > 5$ ) in the interior of the  
784 NTR-RIZ (Figure 5a) is compatible with the WNW-ESE regional extension direction and  
785 counterclockwise rotation of fault and basement fabric trends from the STR-RIZ to NTR-RIZ  
786 (Figures 5d-e, 6c-d). However, the presence of oblique normal faulting earthquakes near the  
787 Rukwa Rift tip (Figure 5a; Lavayssière et al 2019) possibly indicates local stress rotations in  
788 the RIZ (Morley, 2010). Local rotations of the SHmin orientation into fault-orthogonal trends  
789 have also been highlighted in the northern Malawi Rift (Kolawole et al., 2018) and southern  
790 Malawi (Williams et al., 2019). Overall, the alignment of fault trends and basement fabric  
791 trends (Figures 5d-e) suggest that at gross-scale, the RIZ breaching is associated with an  
792 exploitation of the inherited basement fabrics. With progressive strain accommodation  
793 along the breaching faults, well-developed fault-bounded breaching valleys with permanent  
794 fluvial system could develop, first along the Ifume and Nkamba faults, and subsequently, the  
795 faults along-trend of the Kavuu River. We note that the Ifume River which appear to extend  
796 from the Rukwa Rift into Lake Tanganyika only served as a temporary fluvial link between  
797 the two lakes during an ancient phase of overflowing of Lake Rukwa (Cohen et al., 2013).

798 We suggest that the 1<sup>st</sup>-order trends, flow directions, and longitudinal relief gradients of the  
799 RIZ-sourced axial streams in the NTR-RIZ indicate a dominant direction of the NTR-RIZ  
800 breaching. The Kavuu River (axial stream) originates near the termination zone of one of the  
801 splay troughs where the distal upstream segment of the stream shows generally smaller  
802 channel width and lower sinuosity (Figure 6i). Whereas further SW, within the Rukwa Rift,  
803 the river exhibits higher sinuosity and larger channel width. Other geomorphic features  
804 influencing the local shape of the axial stream profile are associated with lake-level

805 fluctuations (Lake Rukwa paleo-shorelines; Figures 5a and 6i; Delvaux et al., 1998) which  
806 are controlled by coupled tectonics and paleoclimatic conditions (Delvaux et al., 2011).

807

#### 808 **4.4. Rift Interactions at the South Malawi-Shire RIZ (SMS-RIZ)**

809 The border faults of the Zomba Graben are the southern continuation of the Malawi Rift  
810 border fault systems (Figure 7a). Thus, being the southernmost segment of the rift, the  
811 Zomba Graben represents the RIZ between the Malawi Rift and the Shire Rift. In the northern  
812 part of the Zomba Graben (distal to the Shire Rift), the intra-basinal and border faults are  
813 mostly parallel or sub-parallel and trend NNE, except for a few NE and ENE steps along the  
814 border faults (Figure 7a and 7dii). The alignment of the fault trends with the orientation of  
815 the pre-rift basement fabrics indicates a control of basement fabrics on fault geometries  
816 (Figure 7c, 7di and 7dii). Whereas basement fabrics and rift faulting in the South Zomba  
817 Graben appear to be relatively more complex, and the intra-basinal faults define an NNW-  
818 trending fault/mega-fracture cluster which is oblique to the NE-trend of the Zomba Graben  
819 and border faults (Figures 7a, 7c). This intra-basinal fault cluster extends NNW along the  
820 Lukhubula fault system in the footwall of the Thyolo Fault (Shire Rift active border fault) into  
821 the axis of the South Zomba Graben, exhibiting soft- and hard-linkage patterns with the  
822 Zomba Graben border faults (Lisungwe, Zomba, and Chingale Step Faults) and the North  
823 Zomba intra-basinal faults (Mlungusi and Mtsimukwe Faults).

824 The clockwise rotation of the northwestern tip of the Thyolo Fault from a NW trend to NNW  
825 trend appears to have been guided by a pre-existing basement shear zone (Figure 7c and  
826 inset; Morel, 1958), but is also well-oriented to be reactivated in the current ENE extension

827 direction. Also, we note that although the breaching fault cluster in South Zomba Graben  
828 generally trend NNW, some of the segments locally crosscut- while others follow the  
829 basement fabrics (Figure 7c). Although the current extension direction (Figure 7a) is  
830 favorable for the reactivation of the NNE- and NW-trending border faults of the Zomba  
831 Graben and Shire Rift (Williams et al., 2019), the NNW-trend of the breaching fault cluster  
832 segments is even more optimally-oriented for reactivation in this regional stress field.  
833 Therefore, we infer that the breach faulting of the SMS-RIZ exhibits a partial control of pre-  
834 rift basement structures, but a stronger control of the tectonic extension direction. In  
835 summary, we suggest that there exists an appreciable structural linkage between the border  
836 faults of the Shire Rift and Zomba Graben, and that the deformation is compatible with the  
837 current stress field and in some places, associated with local exploitation of pre-rift  
838 basement fabrics.

839 The consistency between the along-rift alternation of basin polarity (basin tilt direction, e.g.,  
840 Mack et al., 2006) and the along-rift changes in the location of the main axial stream (Shire  
841 River) indicates the first-order control of rift structure on axial drainage pattern in the  
842 Zomba Graben (Figures 8b-f). The alignment of a segment of the Shire River with a collocated  
843 buried fault and dike (white arrows in Figures 7a and 7c) may also indicate a secondary  
844 structural control on the stream geometry. However, more importantly, the morphology of  
845 the RIZ relief profile (south-facing ramp/step; Type-3 morphology) indicates a  
846 unidirectional southward flow pattern across the RIZ (Figure 8g), along-trend of which the  
847 pre-rift basement is broadly exposed at the rift floor and is flanked to the east and west by  
848 the graben border faults (Figures 8a and 8i). This zone of exposed basement on the rift floor  
849 is collocated with the Middle Shire River where the axial stream longitudinal profile becomes

850 steeper and is dominated by waterfalls, rapids, narrowed channel, and fracture-controlled  
851 stream segments (Figures 8g and 8i).

852 The waterfalls and rapids mostly cluster in the northern part of the area of the rift-floor  
853 basement exposure where the Shire River follows the limb of a plunging fold structure (see  
854 Figures 7b-c, and 8a and 8g). At a large-scale, there is no observable basement lithologic  
855 contact (Figures 7b-c) cross-cutting the river channel at the location of the waterfalls,  
856 however, it is possible that locally, lithologic contacts influence their development. Overall,  
857 the mega-scale 'topographic step' in the Middle Shire River, itself represents the most  
858 prominent knickpoint along the entire course of the Shire River. We suggest that the  
859 waterfalls likely developed as the stream attempts to adjust to a new longitudinal drainage  
860 profile (supported by observations in Bloomfield, 1965; Dulanya, 2017). Therefore, these  
861 observations all together, indicate that although the SMS-RIZ is breached, the breaching is  
862 most likely a recent event.

863 The southern Malawi Rift evolved through the episodic southward propagation of the  
864 Malawi Rift (Scholz et al., 2020), subsequently leading to its tectonic interaction with the  
865 eastern sub-basin (Lower Shire sub-basin) of the Shire Rift Zone. The North Zomba Graben  
866 is dominated by paleo-lake sedimentary deposits (Matope Beds and associated lacustrine  
867 clays) of Neogene age or younger which directly overlie the Precambrian basement  
868 unconformity surface, and are overlain by the alluvial sediments of the Shire River  
869 (Bloomfield and Garson, 1965; Thomas et al 2009; Lyons et al 2015; Dulanya, 2017;  
870 Wedmore et al 2020). This shallow paleo-lake (or swamp) developed within a structural-low  
871 land area (fault-bounded?) surrounded by basement uplifts from which sediments were

872 sourced into the lake (Dulanya, 2017). In essence, the paleo-lake was restricted to the south  
873 by an elevated basement area, which separated the lake from the Shire Rift. Based on paleo-  
874 environmental reconstruction and consideration of likely provenance of the paleo-lake  
875 sediments, it was concluded that linkage of the Upper and Lower Shire River segments (i.e.,  
876 linkage of the Zomba Graben and Shire Rift depositional environments) is a 'recent' feature  
877 (Dulanya, 2017). The observations of a previously restricted depocenter in the North Zomba  
878 Graben are consistent with our analyses, emphasizing that the present-day location of the  
879 South Zomba Graben (Middle Shire River segment) must have been an elevated basement  
880 region in pre-Quaternary times. Thus, the progressive brittle deformation, erosion, and  
881 subsidence of the uplifted cross-over region (in the Quaternary) facilitated the continuous  
882 south-directed flow of the axial stream (Shire River) from the Lakes Malawi and Malombe,  
883 through the south Zomba area, into the Lower Shire sub-basin of the Shire Rift.

884 We suggest that the breaching of the SMS-RIZ is facilitated by both the NW-NNW propagation  
885 of the Thyolo Fault (and the Lukhubula Fault System in its footwall) and the concurrent  
886 southward propagation of the Zomba Graben border faults, largely guided by the current  
887 extension direction. An early-rift localization of significant intra-basinal strain in the Zomba  
888 Graben has been highlighted but is inferred to be possibly controlled by a deeper lower-  
889 crustal mechanical heterogeneity along the rift axis (Wedmore et al., 2020). However, the  
890 basement fabrics (which represent exhumed lower-crustal structures) do not show the  
891 presence of a discrete pre-rift terrain boundary along the rift axis (Figure 7b); rather the  
892 fabrics show a north-plunging fold structure. Although, the large fold structure extends  
893 across the entire rift width, the large-scale aeromagnetic character of the basement fabrics  
894 changes across the western border fault (Lisungwe Fault) and more significantly across the

895 eastern border fault system (Chingale Step and Zomba Faults) (Figures 7b-c; also see  
896 Nyalugwe et al., 2019a, 2020). Most of the length of the Lisungwe Fault (LsF) appear to have  
897 propagated along a boundary of contrasting basement fabrics (NE-SW and WNW-ESE fabrics  
898 in the hanging wall, NW-SE and N-S fabrics in the footwall). Thus, the prominent mechanical  
899 weaknesses of the exhumed basement occur primarily along the border fault zones and not  
900 the intrabasinal domain of the Zomba Graben. Therefore, we suggest that this early-stage  
901 intra-basinal strain localization in the Zomba Graben can also be explained by the recent  
902 breaching of the RIZ and migration of strain into the axis of the Zomba Graben through the  
903 breaching fault/mega-fracture clusters.

904

#### 905 **4.5. Rift Interactions at the Albertine–Rhino RIZ (AR-RIZ, a.k.a. BRIZ)**

906 The Butiaba Rift Interaction Zone (BRIZ) represents the RIZ between the Albertine and  
907 Rhino Rifts. The BRIZ is bounded by a tight cluster of short en-echelon faults to the southwest  
908 and relatively longer fault segments to the southeast and northeast (Figure 9a). Although the  
909 basement fabrics show a multimodal trend (Figure 9b), a secondary NNE-trending set is  
910 parallel to the dominant fault trend (Figure 9c). We observe that two major breaching fault  
911 systems extend from the NW border fault of the Albertine Rift (Bunia Fault), across the BRIZ,  
912 and soft-link or hard-link with the border faults of the Rhino Rift. These two systems include  
913 the tight cluster of short en-echelon faults that appear to link up with the western Luku  
914 border fault of the Rhino Rift, and a system of fault splay consisting of three ‘large’ fault  
915 strands that extend towards the southern tip and footwall of the Rhino border fault of the  
916 Rhino Rift (Figure 9a). These BRIZ breaching fault systems are sub-orthogonal to the crustal

917 stretching direction, are locally parallel to a pre-rift fabric trend, and oblique to the trend of  
918 the BRIZ (Figure 9a and 9c). Also, the extension direction is moderately oblique to the rift  
919 trends, consistent with analog modelling results (Zwaan et al., 2016). Overall, these  
920 geometrical relationships suggest that the brittle deformation of the BRIZ exploited the  
921 basement fabrics in an oblique rifting tectonic setting.

922 The axial stream longitudinal profile is very flat in this region, and the river itself is  
923 characterized by generally large channel widths (Figure 10a), suggesting a low energy  
924 equilibrated axial stream. The morphology of this axial stream profile relative to those of the  
925 other representative RIZs analyzed in this study is quite unique and indicative of the  
926 evolutionary stage of the RIZ. Seismic reflection imaging of a part of the BRIZ that is proximal  
927 to the Albertine Rift reveals ~2 km sedimentary fill (Simon et al., 2017), indicating a  
928 relatively significant basin subsidence in the RIZ. This magnitude of subsidence in the BRIZ  
929 is important, considering that prior to the structural deformation and subsidence across a  
930 RIZ, the cross-over region must have been an elevated basement area (see analog models in  
931 Zwaan et al., 2016). These observations lead us to infer that the Albertine – Rhino RIZ is  
932 indeed a breached RIZ, and that any paleo-intervening basement-high is faulted (footwall  
933 blocks of Ragem Fault and Bunia Fault Splay-3) and buried, and the axial stream now simply  
934 flows across its own floodplain.

935 We suggest that the Ragem Fault (northern splay-2 of the Bunia Fault) and the splay-3 of the  
936 Bunia Fault represent the master strain transfer faults in the BRIZ. However, it is much likely  
937 that as continental extension progresses, the present structure of the RIZ will continue to  
938 evolve. Recent seismicity in the RIZ suggests continued reactivation of the breaching faults.

939 If the Ragem Fault continues to propagate further northward into the footwall of the Rhino  
940 Rift, prominent overlapping geometries may develop between the Rhino and Albertine Rifts.  
941 The change in the channel geometry, channel width, and the partitioning of morphology  
942 anomalies of the of the Albert Nile River across the major RIZ faults (Ragem, Panyango, and  
943 Splay-3 faults; Figures 10a-e), and recent earthquakes (Figure 9a), demonstrate that the  
944 BRIZ faults are still active. The findings also support a continued structural control on the  
945 large-scale axial stream morphology in a breached RIZ along young continental rifts.

946

#### 947 **4.6. The Stages of Rift Linkage in Non-Magmatic Continental Rift Interaction Zones**

##### 948 *4.6.1. Evolutionary Stages of Rift Segment Interaction and Linkage across RIZs*

949 To assess the stage of breaching of a RIZ (i.e., stage of linkage of the associated interacting  
950 rift segments), we consider: 1) the presence or absence of faults extending from one rift  
951 segment to the other rift segment, and 2) the presence of an established physical linkage of  
952 the depositional environments of the two rifts (i.e., are the basins open to each other?). Based  
953 on the observed fault patterns in the representative RIZs, the extents and flow directions of  
954 the associated axial streams, and long-wavelength topographic relief shapes, we present four  
955 possible sequential stages of RIZ breaching and rift linkage in active continental rift systems  
956 (left panel of Figure 11). These stages include unbreached, partially breached, recently  
957 breached, and breached RIZs. Further, based on the observed directionality of axial stream  
958 flow and rift-related sediment accumulation zones around the analyzed RIZs, we present an  
959 idealized stratigraphic evolution of the sedimentary stratigraphy of the RIZs (middle and  
960 right panels of Figure 11).

961 Prior to rift linkage, the intervening RIZ is essentially a relatively elevated basement region  
962 with steep flanks relative to the axes of the interacting rift basins (unbreached RIZ separating  
963 unlinked rift segments, Stage-1; Figure 11a). At this stage, the axial streams of the two rifts  
964 with sources in the cross-over region are not linked, such that a bi-directional pattern of  
965 sediment dispersal (2-D perspective along cross-over profile) from the RIZ into the rift  
966 basins will likely dominate. However, with the progressive lateral propagation of the rift tips,  
967 the breaching faults extend further into the RIZ, grabens and half-grabens begin to localize  
968 within the RIZ, and with continued erosion of the elevated areas, localized zones of  
969 subsidence and sediment accumulation begin to extend from the rift tips into the RIZ. Thus,  
970 an unbreached RIZ may evolve into a narrowed cross-over basement-high with fault  
971 networks that extend between the interacting rift tips but in which a through-going well-  
972 developed rift valley is yet to develop across the RIZ, a stage which we describe as a “partially  
973 breached RIZ” (partially linked rifts, Stage-2; Figure 11b). The NTR-RIZ, and the Luano-Kafue  
974 RIZ (LK-RIZ) exhibit characteristics that demonstrate this stage of rift linkage. As a note of  
975 caution, we emphasize that the cross-over topographic relief geometries of a Stage-2 RIZ is  
976 likely strongly dependent on the directionality of propagation of the RIZ breaching and the  
977 spatial variation of basement erodibility.

978 With continued propagation of the breaching faults and deepening of grabens within the  
979 deforming RIZ, the rift bounding faults of the interacting rift segments establish connection  
980 and one or more well-developed rift valleys are established across the RIZ. As the rift linkage  
981 creates a continuous rift valley floor connecting the interacting rift basins, a reversal of the  
982 antecedent axial streams sourced from the RIZ may occur, resulting in the development of a  
983 common axial stream that flows unidirectionally between the newly-linked rift segments. At

984 this initial stage of successful establishment of rift linkage, we refer to the RIZ as a “recently  
985 breached RIZ” (recent rift linkage, Stage-3; Figure 11c). The SMS-RIZ (Figure 4a) exhibits  
986 characteristics that can be interpreted to represent this stage of rift linkage. We clarify that  
987 'recent' as used in the context of "recently breached RIZs" is qualitative, primarily relevant  
988 to modern active continental rift environments.

989 The transition from Stage 2 to Stage 3 facilitates the evolution of the interacting rifts from  
990 hydrologically closed basins to open ones as their depositional systems become linked (e.g.,  
991 Gawthorpe and Leeder, 2000). Also, we highlight the possible prominence of capturing  
992 and/or reversals of antecedent axial streams flowing into the interacting rift basins as the  
993 RIZ cross-over region transitions from Stage 2 to Stage 3. However, it should be noted that  
994 apart from strain rates on breaching faults, how quickly a Stage-2 RIZ (partially breached)  
995 transitions into Stage 3 can be significantly determined by basement structure and  
996 lithological heterogeneity, which often impact the rates of fluvial erodibility and drainage  
997 divide mobility patterns within the uplifted cross-over region (e.g., Annandale, 1995;  
998 Zondervan et al., 2020). Also, the fluvial erodibility and drainage divide mobility within the  
999 deforming RIZ prior to linkage, and the rate of sediment filling in the interacting basins at  
1000 the Stage 3 will potentially influence the transition from one stage to another.

1001 Finally, with the continued coalescence of the linked breaching and border fault systems of  
1002 the interacting rifts, the RIZ cross-over topography becomes progressively worn down by  
1003 the axial drainage system and its transverse streams as unidirectional flow of the axial  
1004 stream dominates. Also, the axial stream longitudinal profile attains the form of a low energy  
1005 equilibrated axial drainage system. We refer to this stage as “breached RIZ” (Figure 11d).

1006 Thus, in humid continental rift settings where sedimentation rates are keeping up with strain  
1007 rates on faults, the breaching of RIZs and structural linkage of interacting rift segments are  
1008 important for persistent drainage network connectivity and sediment transport between the  
1009 interacting rift segments.

1010 We note the common occurrence of the Type-3-4 morphology at the RIZs separating active  
1011 EARS and unreactivated Mesozoic Karoo rifts (e.g., Figure 4e). The exception is the UK-RIZ  
1012 where the interacting rifts although are EARS segments, contain Mesozoic Karoo  
1013 sedimentary rocks (Choubert et al., 1988). Thus, we infer that the Type-3-4 morphology  
1014 indicates a RIZ that is breached, in which the breaching may or may not have occurred in the  
1015 most recent phase of extension. However, more importantly, the morphology represents a  
1016 breached RIZ in which the axial stream has not yet equilibrated. Along the WB-EARS, where  
1017 a Type-3-4 cross-over profile connects a failed Mesozoic rift with an overlapping active EARS  
1018 segment, the Mesozoic rift basin is often located in the elevated part of the profile which is  
1019 in the rift flank of the active rift and is explainable by the flexural uplift of the flanks of the  
1020 active rift segment. Therefore, due to the uplift of the rift flank, the sedimentary or volcanic  
1021 rift-fill of the failed rift will generally undergo erosion and incision by streams as the deposits  
1022 are reworked into the linked actively subsiding rift basin. However, if a Type-3-4 cross-over  
1023 morphology is observed across an RIZ between two active rift segments, this may indicate  
1024 an imbalance of sediment supply rate relative to strain rate between the two linked active  
1025 rift segments, thus, creating an overfilled basin in one segment, and an underfilled one in the  
1026 other.

1027 We emphasize that defining the breach stage of an active RIZ solely by the cross-over  
1028 topographic morphology only could be misleading. For example, although the Zambezi-  
1029 Kafue RIZ (ZK-RIZ) exhibits a Type-3 morphology, and the axial stream (Kafue River) flows  
1030 unidirectionally across the RIZ, there no evidence of graben or half graben development  
1031 along the axial stream valley. Thus, in this case, the fluvial linkage of the Kafue and Zambezi  
1032 Rifts is likely not related to a structural breaching of the RIZ. We speculate that the  
1033 development of Type-3 morphology across the ZK-RIZ is related to Holocene-age dynamic  
1034 topographic uplift in the vicinity of the Kafue Rift (Daly et al., 2020) possibly resulting in the  
1035 sediment overfilling-to-spill in the rift, or a combination of this and a partial structural  
1036 breaching of the ZK-TZ.

1037 The simplified models presented in Figure 11 summarize our observations along the WB-  
1038 EARS, and idealizations in aspects for which we do not have direct observations (e.g., buried  
1039 subsurface stratigraphy of breached RIZs). The models assume 1) a humid continental  
1040 setting, 2) orthogonal extension, 3) the erodibility of the pre-rift basement is relatively  
1041 uniform, 4) sediment supply into the interacting rift basins keeps up with strain rates on  
1042 faults, and 5) no significant influence of dynamic topography within the deforming RIZs.  
1043 Although our models are based on regions of active early-stage (stretching phase)  
1044 continental rifting in which at least one of the interacting rift pairs is active, the observations  
1045 are relevant for buried rift interaction zones in ancient rift settings. Our study suggests that  
1046 for a given directionality of breaching, paired RIZs that are not fault-bounded or are fault-  
1047 bounded on only one flank should exhibit a distinct long-wavelength 2-D topographic relief  
1048 shapes. When the assessment of the long-wavelength 2-D topographic relief shape across the  
1049 RIZ is combined with analyses of the breaching fault patterns, the stage of RIZ breaching can

1050 be inferred (Figure 11). Therefore, given the assumptions made on the models, the 2-D  
1051 topographic profiles across an unbreached RIZ exhibit a shape that is similar to Type-1  
1052 morphology (depending on if the RIZ is fault-bounded or not), and profiles across an RIZ that  
1053 is already breached or is in the final stages of breaching should exhibit shapes similar to  
1054 Type-3, Type-3-4, or Type-4.

1055 The overlapping parallel RIZs along the WB-EARS generally have a lateral rift-orthogonal  
1056 separation distance of  $\leq 100$  km, consistent with recent analog models (Allken et al., 2011,  
1057 2012; Zwaan and Schreurs, 2020) which suggest an upper limit of 300 km separation  
1058 distance, below which rift segments will likely not interact. However, the deformation  
1059 patterns in various overlapping parallel RIZs in natural rift settings show that this RIZ  
1060 geometry may be unique, in that the attainment of breaching may involve the development  
1061 of 1.) cross-faulting that connects the interacting rift segment tips, 2.) cross-faulting that  
1062 extend across the intervening horst block (i.e., flanks of interacting segments), and/or 3.)  
1063 localization of a cluster of narrower en-echelon rift basins (i.e., subsidiary rift basins) within  
1064 the horst block. However, in the case of the development of such subsidiary rift basins (e.g.,  
1065 NLNM-RIZ in Figure 4a, and Limagne–Bresse RIZ), the breaching of the RIZ must involve the  
1066 structural connectivity of the subsidiary basins with at least one of the interacting rift  
1067 segments and transport of the sediments between both.

1068 Since the linkage of interacting rift segments is manifested in the physical linkage of their  
1069 intra-basinal and/or border fault segments, we hypothesize that post-linkage, interacting  
1070 rifts may show a record of accelerated strain and subsidence across the breached RIZ  
1071 (Figures 11d and 12; Gawthorpe and Leeder, 2000). Studies have shown that the linkage and

1072 coalescence of propagating fault segments often lead to increased strain accommodation and  
1073 basin subsidence rates along the newly linked faults (e.g., Gupta et al., 1998; Gawthorpe and  
1074 Leeder, 2000; Taylor et al., 2004; Cowie et al., 2005). For example, in the Whakatane Graben,  
1075 New Zealand, the post-linkage displacement rate of the major normal faults increased by up  
1076 to threefold (Taylor et al., 2004). The unavailability of high-resolution data on fault  
1077 displacement rates at the representative WB-EARS RIZs analyzed in our study makes it  
1078 currently difficult to test this hypothesis. Therefore, there is a need to better understand the  
1079 significance of the temporal variations of breaching fault displacement rates for the  
1080 evolution of RIZs. Overall, we emphasize that post-linkage, coalesced rift basins may  
1081 preserve a buried record of paleo-RIZs that indicate the location of an initial phase of  
1082 separated rift segments, progressive breaching of the intervening zones, and subsequent  
1083 linkage of the segments (Figure 12).

1084

#### 1085 ***4.7. Lateral Rift Segment Propagation and Directionality of RIZ Breaching***

##### 1086 *4.7.1. What Drives the Lateral Propagation and Interaction of Continental Rift Segments?*

1087 At the larger rift system-scale, continental rift propagation is driven by gravitational stresses  
1088 and extension gradients imposed by rotational and orthogonal plate extension, assuming a  
1089 homogenous continental crust (Corti et al., 2007; Mondy et al., 2018; Molnar et al., 2018;  
1090 Zwaan and Schreurs, 2020). Also, rotational rifting may play important roles in driving rift  
1091 segment propagation during late-stage rift settings where transitional crust dominates (e.g.,  
1092 the Afar region, Kidane et al., 2003; Zwaan and Schreurs, 2020). However, at the relatively  
1093 less understood segment-scale of rift propagation in juvenile rift settings, our study suggests

1094 that anomalous earthquake clustering at the rift tips indicates local stress concentrations at  
1095 the propagating rift tips (e.g., NTR-RIZ, Figure 5). Another example of this is the anomalous  
1096 clustering of earthquakes at the northern and southern tips of the Turkana Rift (Musila et al.,  
1097 2020). We argue that similar to the mechanics of fracture propagation (e.g., Kranz, 1979),  
1098 such stress concentrations at and ahead of the tips of active rift segments play important  
1099 roles in driving the propagation of breaching faults from the rift tip into the associated RIZ.  
1100 Further, we find that the geometries of the propagating breaching faults are modulated by  
1101 both the extension direction and inherited (pre-rift) basement fabrics. We speculate that the  
1102 focusing of magmatism at rift interaction zones (e.g., Rungwe, Toro-Ankole, and Kivu  
1103 Volcanic Provinces in Figure 4a; Njinju et al., 2019a,b), in combination with magma-driven  
1104 faulting, reflects an important contribution of magmatism to lateral rift propagation into  
1105 deforming RIZs (Heilman et al., 2019).

1106

#### 1107 *4.7.2. Directional Propagation of RIZ Breaching and Rift Linkage*

1108 The lateral separation geometry of interacting continental rift segments (underlap/overlap  
1109 angles and distance) determines if and how they will interact spatially (e.g., Tentler and  
1110 Acocella, 2010; Zwaan et al., 2016; Zwaan and Schreurs, 2020; Neuharth et al., 2021). Thus,  
1111 with continued tectonic extension, an isolated rift segment may progressively propagate  
1112 laterally until its 'breaching distance' (distance from another rift segment) is small enough  
1113 to permit interaction and development of breaching faults in the RIZ cross-over area. Our  
1114 observations at the representative non-magmatic RIZs and observations along other  
1115 segments of the East African Rift System reveal three distinct styles of rift propagation

1116 associated with RIZ breaching (Figures 12a-b). In one case, we observe that only one of two  
1117 interacting rift segments acts as the propagating segment (i.e., the ‘propagator’) such that  
1118 the other ‘non-propagating’ segment represents the ‘receiver’, demonstrating a  
1119 unidirectional style of RIZ breaching and rift linkage (Figure 12a). For example, in the NTR-  
1120 RIZ (Figure 6), the Rukwa Rift represents the propagator, and the Tanganyika Rift represents  
1121 the receiver.

1122 In another case, we find evidence that suggests that both interacting segments propagated  
1123 towards one another, indicating a bi-directional style of RIZ breaching (Figure 12a). An  
1124 example of bi-directional RIZ breaching is the SMS-RIZ (Figures 7 and 8). In a third case,  
1125 strain localizes within the interior of the RIZ as a narrower rift basin which propagates  
1126 outwards to link with the major interacting rift segments (Figure 12b). An example of this  
1127 intra-RIZ outward breaching is the Turkana Depression which represents the zone of  
1128 interaction between the Main Ethiopian Rift and the Kenya Rift (Wang et al., 2021). Within  
1129 the Turkana Depression RIZ, the Turkana Rift appears to have developed as a single coherent  
1130 tectonic element that localizing most of the intra-RIZ strain and is facilitating rift linkage  
1131 across the Turkana Depression (Knappe et al., 2020; Musila et al., 2020).

1132 Also, it is important to note that in areas of multiphase rifting where a younger rift segment  
1133 may propagate towards an older failed rift segment, the younger active rift represents a  
1134 propagator, and the ‘inactive’ (or partially active) older rift segment largely represents a  
1135 receiver. Further, we suggest that the geometrical configuration of certain RIZ classes  
1136 (Figure 3) promote the dominance of unidirectional breach propagation over bi-directional  
1137 propagation. For example, overlapping oblique and overlapping orthogonal RIZs would

1138 almost always experience unidirectional breach propagation. Whereas overlapping and  
1139 underlapping parallel RIZs may accommodate both unidirectional and bi-directional breach  
1140 propagation patterns.

1141

#### 1142 *4.7.3. Rift-Tip Structures and Overlap Rift-Flank Interactions*

1143 Models of interaction between parallel rift pairs (i.e., parallel RIZs) have demonstrated how  
1144 the obliquity or orthogonality of extension direction can influence the patterns of rift-tip  
1145 interactions and geometry of breaching faults in homogeneous media, and in the presence of  
1146 a connecting pre-existing fault (e.g., Acocella et al., 1999; Aanyu and Koehn, 2011; Zwaan et  
1147 al., 2016; Zwaan and Schreurs, 2017, 2020). Model results and the natural examples  
1148 examined in our study show that the breaching of RIZs is facilitated by more complex  
1149 patterns of structural deformation that link the interacting rift basins.

1150 On a large-scale, we find that RIZ breaching is commonly facilitated by propagating rift-tip  
1151 (e.g., in tip-to-tip collinear, and underlapping RIZs) and/or overlap rift-flank deformation  
1152 (e.g., in some overlapping oblique and parallel divergent RIZs). Along the WB-EARS, we  
1153 observe that propagating rift-tips are characterized by 1) rift splay creating a pattern of  
1154 smaller and narrower graben and/or half-grabens (e.g., rift bifurcations, rift trifurcations  
1155 etc.), 2) rotation of the propagating border fault tip, and/or 3) network of fault clusters, that  
1156 extend into deforming RIZs. An example of overlap rift-flank deformation is the breaching of  
1157 the UK-RIZ, NLNM-RIZ, and SMS-RIZ (Figures 4a and 12a). Whereas examples of rift splay  
1158 include splay troughs at the NW Rukwa Rift tip, bifurcation of the SE Rukwa Rift tip,  
1159 trifurcation (or greater) of the NW Luama Rift tip, bifurcation of the northern Edward Rift

1160 tip, splay faulting at the northern Albertine Rift tip (Figures 4a and 13a). An example of  
1161 border fault tip rotation is the clockwise rotation of the NW tip of the Thyolo border fault in  
1162 the SMS-RIZ. Also, examples of RIZ breaching by fault cluster networks include the BRIZ and  
1163 SMS-RIZ (Figures 7a and 9a).

1164 We suggest that rift splay and border fault rotation are analogous to the geometries of fault  
1165 networks that have been observed at the laterally propagating fault tips (e.g., Kim et al.,  
1166 2004; Perrin et al., 2016; Phillips et al., 2019). Although rift splay was previously presented  
1167 as a type of rift segment geometry (Nelson et al., 1992), we argue here that rift splays and  
1168 border fault rotation at rift tips represent genetic characteristics of the lateral propagation  
1169 of rift segment tips. Thus, such structures, although not the RIZ itself, could suggest the  
1170 termination zone of a rift segment, or that a propagating rift segment is approaching an  
1171 interaction zone with another rift segment. Numerical models show the development of rift  
1172 tip splays and/or border fault rotation at RIZs in areas of lateral propagation and interaction  
1173 of rift segments (e.g., Zwaan et al., 2016; Zwaan and Schreurs, 2020; Neuharth et al., 2021).

1174 Thus, the preservation of the rift-tip structures highlighted in this study within the syn-rift  
1175 sequences of composite rift basins (i.e., coalesced segmented rifts) may provide insight into  
1176 previous rift-tip termination zones and zones of interaction with another rift segment prior  
1177 to linkage. For example, the buried bifurcation zone in the central Malawi Rift (vicinity of the  
1178 Likoma-Lipichilli Horst; Specht and Rosendahl, 1989) is collocated with the inferred earlier  
1179 termination zone of the northern Malawi Rift during the long-term southward propagation  
1180 of the Malawi Rift (Scholz et al; 2020).

1181 An example of buried border fault rotation zone is in the central Tanganyika Rift where the  
1182 rift is segmented across the Kavala Island Ridge - a RIZ which was breached and buried as  
1183 seen in seismic interpretations (Wright et al., 2020). The vicinity of the Kavala Island Ridge  
1184 (Kalemie area, central Tanganyika Rift) shows a relatively lower tectonic extension relative  
1185 to the northern Ruzizi-Kigoma and southern Marungu-Mpulungu sub-segments (Wright et  
1186 al., 2020); indicating that the central Tanganyika area is a paleo-RIZ between the northern  
1187 and southern sub-segments prior to the breaching and subsidence of the Kavala Island ridge.  
1188 The Rwenzori RIZ between the Edward and Albertine Rifts show both well-developed  
1189 bifurcation and border fault rotation patterns (Koehn et al., 2008).

1190 At zones of rift slays, it appears that at least one of the splay branches (splay trough) may  
1191 eventually 'fail' while one or more branches continue to localize most of the tectonic strain  
1192 and facilitate a successful linkage with the interacting rift segment. For example, the Songwe  
1193 Trough of the SE Rukwa Rift bifurcation has localized greater strain and breaching of the  
1194 Rukwa-North Malawi RIZ (Mbozi block) than the Msongano Trough (Heilman et al., 2019).  
1195 Additionally, the Malombe Graben of the Southern Malawi Rift bifurcation is a better-  
1196 developed bifurcation branch than the Makanjira Trough as evidenced by the continuation  
1197 of the rift valley floor, axial stream linkage (Shire River), and localization of a major lake  
1198 (Lake Malombe) along the Malombe Graben (Figures 7a, 8a and 8c; see also Dulanya, 2017).

1199 Overall, our analyses show that although RIZs may differ in both their geometries and  
1200 evolutionary stages, there exist distinct long-wavelength 2-D cross-over relief profile  
1201 geometries that are unique to each of the evolutionary stages within a given erodibility  
1202 structure, breaching propagation directionality, strain rate, and sediment-supply rate across

1203 the RIZ. We envision that our observations in this study provide predictive models for the  
1204 geometry and temporal evolution of paleo-RIZs preserved in the stratigraphic record of  
1205 mature continental rifts and passive margin basins. However, we acknowledge that further  
1206 refinement of these models should be undertaken with additional studies of both ancient and  
1207 modern systems.

1208

#### 1209 **4.8 Implications for Early-Stage Continental Rift Growth in East Africa**

1210 Along the eastern Africa rift zones analyzed in this study, based on the long wavelength  
1211 cross-over relief morphology, fluvial isolation/linkage of interacting rifts, and the general  
1212 breaching fault patterns at the RIZs, we find that at least 60 % of the RIZs exhibit  
1213 characteristics of breaching (Figures 13a and 13b). The unbreached and partially breached  
1214 RIZs account for up to ~37 % of the RIZs. We characterize all magmatic RIZs as “breached”  
1215 because of the lithospheric-scale deformation associated with magmatism. Several of the  
1216 Mesozoic rift segments (pre-EARS) show characteristics of breaching across the RIZs (fault  
1217 connectivity and proximity/overlapping of rift-fill e.g., Kariba-Zambezi, Ruhuhu–Malawi,  
1218 Maniamba-Malawi, Luangwa-Zambezi, and Shire-Zambezi RIZs; Figure 13a). The  
1219 development and lateral propagation of the Cenozoic rift segments have facilitated their  
1220 linkage with the Mesozoic rift segments (Delvaux, 1989). Overall, we note that the northern  
1221 regions of the WB-EARS and the southern regions of the EB-EARS appear to be dominated  
1222 by breached RIZs, whereas the rift segments further south show more of partially breached,  
1223 recently breached, and unbreached RIZs (Figure 13a). The apparent southward and  
1224 southwest-ward increase in the occurrence of unbreached, partially breached, and recently

1225 breached RIZs reflects the proposition of an active southwest-ward propagation of the East  
1226 African Rift System (Daly et al., 2020).

1227 Cenozoic continental extension in the EARS initiated ~40 Ma (Boone et al., 2019), and its  
1228 Western Branch (WB-EARS) evolved ~25 Ma (Roberts et al., 2012), such that by the Middle  
1229 Miocene to Pliocene, most of the rift segments had been established (Simon et al., 2017;  
1230 Scholz et al., 2020). However, the predominance of breached RIZs along these juvenile  
1231 branches of the East African Rift System (Figure 12a), suggest that the early-stage  
1232 establishment of the EARS segments is associated with considerable RIZ breaching and rift  
1233 linkage. This is supported by previous observation of early linkage of rift faults along the East  
1234 African Rift System (Morley, 1999).

1235 Although the EARS is actively growing, the early-development of most of its segments is  
1236 consistent with observations of early-stage rapid establishment of segments in the East  
1237 Greenland rift system (i.e., within the first 20 % of rift life; Rotevatn et al., 2018). Therefore,  
1238 we propose that the continued southward and southwest-ward growth of the EARS (Ebinger,  
1239 1989; Chorowicz, 2005; Daly et al., 2020; Zwaan and Schreurs, 2020; Ngalamo et al., 2020)  
1240 will likely record continued episodes of lateral propagation of the rift tips, linkage across the  
1241 RIZs, intensified deformation and burial of previously breached (paleo-RIZs) and recently  
1242 breached RIZs.

1243

#### 1244 **4.9 Outstanding Questions**

1245 It was suggested that small scale tensile fractures are possible analogs of actively  
1246 propagating continental rift segments (Nelson et al., 1992). Heilman et al. (2019) further

1247 speculated that the laterally propagating rift tips are zones of stress concentration with a  
1248 distinct ‘process zone’, and that RIZs may be areas of overlap between the process zones of  
1249 rift segments that are in proximity of one another. While the geometries and aspects of the  
1250 kinematics of micro-scale fractures may appear to be similar to those of continental rifts, it  
1251 is not yet known if all the elements of the linear elastic mathematical solutions for fracture  
1252 tip propagation are applicable and relevant to the scale of rift basins.

1253 Studies in different continental rift settings have highlighted that RIZs, magmatic focusing,  
1254 and rift linkage are often collocated (e.g., Aldrich, 1986; Ebinger, 1989; Nelson et al., 1992;  
1255 Acocella et al., 1999; Wilson, 1999; Muirhead et al., 2015; Heilman et al., 2019). However,  
1256 since the RIZ breaching faults are relatively younger and often not as well developed as the  
1257 major faults of the interacting rift segments, questions remain on this proposed association.  
1258 Further, we raise another question on the relationship between the successful branches of a  
1259 rift splay and the localization of RIZ magmatism. We observe that the higher strain Songwe  
1260 Trough of the SE Rukwa Rift bifurcation hosts the Rungwe Volcanic Province (Figure 4a;  
1261 Heilman et al., 2019), whereas the Toro Ankole Volcanic Province is in the Lake George  
1262 Graben of the northern Edward Rift bifurcation (Figures 4a and 13a). Also, there is a need to  
1263 better understand the mechanisms that facilitate magmatic focusing into RIZs with thick  
1264 crusts in young continental rift settings (e.g., lower crustal intrusions in South Tanganyika –  
1265 Rukwa RIZ; Hodgson et al., 2017). In addition, there is a need to better understand the  
1266 absence of magmatism in breached RIZs where no surface or deeper magmatism have been  
1267 observed (e.g., Albertine - Rhino Rift’s BRIZ). Future studies should also investigate the  
1268 influence of short-wavelength dynamic topography on RIZ evolution.

1269 Although magmatic RIZs generally show elevated geothermal anomalies, local elevated  
1270 geothermal gradients and heat flow is also observed to localize at active non-magmatic RIZs  
1271 (e.g., SMS-TZ, Njinju et al., 2019a; Walker Lane-Northern Great Basin Transfer Zone, Faulds  
1272 et al., 2010). Thus, interesting questions remain on the relationship between the temporal  
1273 evolution of RIZs and the associated crustal thermal state in active rift settings. Future  
1274 studies should investigate the significance of RIZs and their breach state for geothermal  
1275 system development in active rift settings.

1276 There is a relatively faster crustal stretching rate (2.7 - 2.9 mm/yr) near the partially-  
1277 breached Tanganyika-Rukwa RIZ compared to the 1.5 mm/yr crustal stretching rate near  
1278 the recently-breached South Malawi-Shire RIZ (Saria et al., 2014). However, since the  
1279 tectonic strain is typically distributed across several faults within an active rift basin, and rift  
1280 segment propagation being facilitated by stress concentrations at the rift tip, there remain  
1281 outstanding questions on the factors that preferentially localize tectonic stresses at the rift  
1282 tips, away from the rift axis. Also, we suggest that there is a need to better understand the  
1283 partitioning of seismic versus aseismic strain across actively deforming RIZs, the relevance  
1284 of these modes of strain accommodation in magmatic and non-magmatic RIZs and  
1285 implications for rift linkage.

1286

## 1287 **Conclusions**

1288 We review rift interaction zone (RIZ) geometries, and in the magma-poor, juvenile western  
1289 Branch of the East African Rift System, we investigated the stages of rift linkage and the  
1290 associated physiographic, structural, and broad-scale sedimentation patterns. We examine

1291 representative non-magmatic RIZs in the region and explore the relationships between the  
1292 breaching faults, basement structure, and axial stream patterns. Our main results are:

1293 1.) A new and broader rift interaction zone classification that encompasses a wider range of  
1294 plan-view RIZ geometries and dip polarity of the interacting border faults.

1295 2.) Although RIZs may differ in both their geometries and evolutionary stages, there exist  
1296 distinct long-wavelength 2-D topographic relief geometries, directionality of axial stream  
1297 flow, and breaching fault patterns that characterize RIZs at the various stages of rift linkage.

1298 3.) These stages include unbreached RIZ (associated with unlinked rifts), partially breached  
1299 RIZ (partially linked rifts), recently breached RIZ (recently linked rifts), and breached RIZ  
1300 (linked rifts). Post linkage of the rift segments, a coalesced rift forms, and the zone of rift  
1301 linkage which is buried beneath the younger rift-fill is referred to as a paleo-RIZ.

1302 4.) At deforming RIZs, breaching may propagate in a single direction i.e., unidirectional  
1303 (distinct propagator and receiver segments), or in a bi-directional manner (both interacting  
1304 segments act as propagators and receivers), which may also modulate the cross-over relief  
1305 shape. Also, we find that breaching may propagate outwards from the RIZ in the form of a  
1306 narrow intra-RIZ subsidiary rift basin.

1307 5.) Depending on the RIZ geometry, breaching is commonly facilitated by overlap rift-flank  
1308 deformation and/or distinct rift-tip structures. Propagating rift-tip structures observed in  
1309 the study areas include rift splay, border fault rotation (rift-tip rotation), and fault cluster  
1310 networks.

1311 6.) The lateral propagation of the RIZ breaching faults at the rift tips and flanks, facilitated  
1312 by local stress concentrations, is modulated by both the extension direction and inherited  
1313 basement structures.

1314 7.) At least 60 % of the RIZs along the western, southwestern, and southeastern branches of  
1315 the EARS exhibit breached rift interaction zone characteristics, indicating the early linkage  
1316 of the rift segments. In addition, unbreached and partially breached RIZs are largely located  
1317 in the southern and southwestern parts of the rift system, likely indicating a progressive  
1318 lateral rift propagation and coalescence to the south and southwest of the rift system.

1319 Our findings offer a broader insight into the geometrical complexity and structural evolution  
1320 of rift interaction zones, and provide first-order predictions of large-scale sedimentation  
1321 patterns of humid early-stage continental rift environments. Further, the models proposed  
1322 in this study provide testable hypotheses for linking rift architecture and patterns of early-  
1323 stage (stretching phase) rift sedimentation applicable to ancient rift basins. However, we  
1324 acknowledge that further refinement of these models should be undertaken with additional  
1325 studies of both ancient and modern rift systems.

1326

## 1327 **Acknowledgements**

1328 We thank the South African Development Community (SADC) for providing the Tanzania  
1329 aeromagnetic dataset used in this study. Thanks to Geological Survey of Malawi for providing  
1330 the 2013 aeromagnetic datasets used in this study. None of the authors have a conflict of  
1331 interest to declare. We also thank the editor Atle Rotevatn, reviewers Christopher Morley,  
1332 Jack Williams, and three additional anonymous reviewers for their constructive comments

1333 that have helped to improve the quality of the manuscript. Also, thanks to Frank Zwaan for  
1334 useful comments on the preprint of this paper (available on <https://eartharxiv.org>).

1335

### 1336 **Data Availability**

1337 The Global Multi-Resolution Topography (GMRT) dataset used in this study is public domain  
1338 and is freely available through the GeoMapApp (Ryan et al., 2009). The southern Malawi  
1339 Total Magnetic Intensity (TMI) dataset is archived at the Interdisciplinary Earth Data  
1340 Alliance (IEDA) at doi:10.1594/IEDA/324860 (Nyalugwe et al., 2019b).

1341

### 1342 **Conflicts of Interest Statement**

1343 Author Folarin Kolawole is currently employed by BP America. However, this study and the  
1344 initial manuscript drafts were developed and completed during his stay at the University of  
1345 Oklahoma, prior to joining BP. The remaining authors declare that the research was  
1346 conducted in the absence of any commercial or financial relationships that could be  
1347 construed as a potential conflict of interest.

1348

### 1349 **Author Contributions**

1350 FK conceptualized and developed the project. FK performed the structural mapping and  
1351 analyses. FK, MF, and TA performed the drainage mapping. FK and MF performed the

1352 drainage analysis. FK and MF wrote the manuscript. MJS and EAA edited and improved the  
1353 manuscript. All authors read and approved the final manuscript.

1354 **References**

- 1355 Aanyu, K. and Koehn, D., 2011. Influence of pre-existing fabrics on fault kinematics and rift  
1356 geometry of interacting segments: analogue models based on the Albertine Rift (Uganda),  
1357 Western Branch-East African Rift System. *Journal of African Earth Sciences*, 59(2-3), 168-  
1358 184.
- 1359 Acocella, V., Faccenna, C., Funicello, R. and Rossetti, F., 1999. Sand-box modelling of  
1360 basement-controlled transfer zones in extensional domains. *Terra Nova-Oxford*, 11(4),  
1361 pp.149-156.
- 1362 Aldrich, M.J., 1986. Tectonics of the Jemez Lineament in the Jemez Mountains and Rio Grande  
1363 Rift. *J. Geophys. Res.* 91, 1753–1762.
- 1364 Allen, P.A., 2008. From landscapes into geological history. *Nature*, 451(7176), 274-276.
- 1365 Allken, V., Huismans, R.S. and Thieulot, C., 2011. Three - dimensional numerical modeling of  
1366 upper crustal extensional systems. *Journal of Geophysical Research: Solid Earth*, 116(B10).
- 1367 Allken, V., Huismans, R.S. and Thieulot, C., 2012. Factors controlling the mode of rift  
1368 interaction in brittle - ductile coupled systems: A 3D numerical study. *Geochemistry,*  
1369 *Geophysics, Geosystems*, 13(5).
- 1370 Annandale, G.W., 1995. Erodibility. *Journal of hydraulic research*, 33(4), 471-494.
- 1371 Arkani-Hamed, J. (1988). Differential reduction-to-the-pole of regional magnetic anomalies.  
1372 *Geophysics*, 53(12), 1592–1600. <https://doi.org/10.1190/1.1442441>.
- 1373 Barnes, J.B., Densmore, A.L., Mukul, M., Sinha, R., Jain, V. and Tandon, S.K., 2011. Interplay  
1374 between faulting and base level in the development of Himalayan frontal fold topography.  
1375 *Journal of Geophysical Research: Earth Surface*, 116(F3).
- 1376 Behn, M.D., Lin, J., 2000. Segmentation in gravity and magnetic anomalies along the U.S. east  
1377 coast passive margin; implications for incipient structure of the oceanic lithosphere. *J.*  
1378 *Geophys. Res.* 105 (11), 25769–25790.
- 1379 Bloomfield, K., and Garson, M. S. 1965. The geology of the kirk range – Lisungwe valley area.  
1380 *Bulletin of the Geological Survey of Malawi* 17, Government Printer, Zomba.
- 1381 Boone, S.C., Kohn, B.P., Gleadow, A.J., Morley, C.K., Seiler, C. and Foster, D.A., 2019. Birth of  
1382 the East African Rift System: Nucleation of magmatism and strain in the Turkana Depression.  
1383 *Geology*, 47(9), 886-890.
- 1384 Bosworth, W., 1985. Geometry of propagating continental rifts. *Nature*, 316(6029), 625-627.
- 1385 Braile, L., Keller, G., Wendlandt, R., Morgan, P., & Khan, M. (2006). Chapter 5 The east african  
1386 rift system. *Continental Rifts: Evolution, Structure, Tectonics Developments in Geotectonics*.
- 1387 Childs, C., Holdsworth, R. E., Jackson, C. A.-L., Manzocchi, T., Walsh, J. J. & Yielding, G. (eds)  
1388 2017. *The Geometry and Growth of Normal Faults*. Geological Society, London, Special  
1389 Publications, 439, 79–107.

- 1390 Chorowicz, J., 2005. The east African rift system. *Journal of African Earth Sciences*, 43(1-3),  
1391 pp.379-410.
- 1392 Choubert, G., Faure-Muret, A., Chanteux, P., Roche, G., Simpson, E.S.W., Shackleton, L.,  
1393 Ségoufin, J., Seguin, C. and Sougy, J., 1988. International geological map of Africa. Scale 1: 5  
1394 000 000, Commission for the Geological Map of the World (CGMW), Unesco, Paris.
- 1395 Cochran, J.R., Martinez, F., 1988. Evidence from the northern Red Sea on the transition from  
1396 continental to oceanic rifting. *Tectonophysics* 153 (1-4), 25-53.
- 1397 Cohen, A. S., Bocxlaer, B. V., Todd, J. A., Mcglue, M., Michel, E., Nkotagu, H. H., ... Delvaux, D.  
1398 (2013). Quaternary ostracodes and molluscs from the Rukwa Basin (Tanzania) and their  
1399 evolutionary and paleobiogeographic implications. *Palaeogeography, Palaeoclimatology,*  
1400 *Palaeoecology*, 392, 79-97.
- 1401 Collanega, L., Corti, G., Breda, A., Massironi, M. and Keir, D., 2020. 3D Extension at Plate  
1402 Boundaries Accommodated by Interacting Fault Systems. *Scientific Reports*, 10(1), 1-12.
- 1403 Corti, G. (2012). Evolution and characteristics of continental rifting: Analog modeling-  
1404 inspired view and comparison with examples from the East African Rift System.  
1405 *Tectonophysics*, 522, 1-33.
- 1406 Corti, G., Cioni, R., Franceschini, Z., Sani, F., Scaillet, S., Molin, P., Isola, I., Mazzarini, F., Brune,  
1407 S., Keir, D. and Erbello, A., 2019. Aborted propagation of the Ethiopian rift caused by linkage  
1408 with the Kenyan rift. *Nature communications*, 10(1), 1-11.
- 1409 Cowie, P.A., Underhill, J.R., Behn, M.D., Lin, J. and Gill, C.E., 2005. Spatio-temporal evolution of  
1410 strain accumulation derived from multi-scale observations of Late Jurassic rifting in the  
1411 northern North Sea: A critical test of models for lithospheric extension. *Earth and Planetary*  
1412 *Science Letters*, 234(3-4), 401-419.
- 1413 Daly, M.C., Chorowicz, J. and Fairhead, J.D., 1989. Rift basin evolution in Africa: the influence  
1414 of reactivated steep basement shear zones. *Geological Society, London, Special Publications*,  
1415 44(1), 309-334.
- 1416 Daly, M.C., Green, P., Watts, A.B., Davies, O., Chibesakunda, F. and Walker, R., 2020. Tectonics  
1417 and Landscape of the Central African Plateau, and their implications for a propagating  
1418 Southwestern Rift in Africa. *Geochemistry, Geophysics, Geosystems*, 21, p.e2019GC008746.
- 1419 Delvaux, D., 1989. The Karoo to Recent rifting in the western branch of the East-African Rift  
1420 System: A bibliographical synthesis. *Mus. roy. Afr. centr., Tervuren (Belg.), Dépt. Géol. Min.,*  
1421 *Rapp. ann*, 1990 (1991), 63-83.
- 1422 Delvaux, D. and Barth, A., 2010. African stress pattern from formal inversion of focal  
1423 mechanism data. *Tectonophysics*, 482(1-4), pp.105-128.
- 1424 Delvaux, D., Kervyn, F., Vittori, E., Kajara, R.S.A. and Kilembe, E., 1998. Late Quaternary  
1425 tectonic activity and lake level change in the Rukwa Rift Basin. *Journal of African Earth*  
1426 *Sciences*, 26(3), pp.397-421.

- 1427 Delvaux, D., Kervyn, F., Macheyeke, A. S., & Temu, E. B. (2012). Geodynamic significance of the  
1428 TRM segment in the East African Rift (W - Tanzania): Active tectonics and paleostress in the  
1429 Ufipa plateau and Rukwa basin. *Journal of Structural Geology*, 37, 161–180.  
1430 <https://doi.org/10.1016/j.jsg.2012.01.008>
- 1431 Dèzes, P., Schmid, S.M. and Ziegler, P.A., 2004. Evolution of the European Cenozoic Rift  
1432 System: interaction of the Alpine and Pyrenean orogens with their foreland lithosphere.  
1433 *Tectonophysics*, 389(1-2), 1-33.
- 1434 Drury, S. A. (2001). *Image interpretation in geology*, 3rd Edition, Blackwell Science Inc.,  
1435 Malden, MA.
- 1436 Dulanya, Z., 2017. A review of the geomorphotectonic evolution of the south Malawi rift.  
1437 *Journal of African Earth Sciences*, 129, pp.728-738.
- 1438 Ebinger, C.J., 1989. Tectonic development of the western branch of the East African rift  
1439 system. *Geological Society of America Bulletin*, 101(7), pp.885-903.
- 1440 Ebinger, C.J. (2012). Evolution of the Cenozoic East African rift system. *Regional Geology and*  
1441 *Tectonics: Phanerozoic Rift Systems and Sedimentary Basins*, 132–162.
- 1442 Emishaw, L. and Abdelsalam, M.G., 2019. Development of Late Jurassic - Early Paleogene and  
1443 Neogene - Quaternary Rifts Within the Turkana Depression, East Africa From Satellite  
1444 Gravity Data. *Tectonics*, 38(7), 2358-2377.
- 1445 Fairhead, J.D., 1988. Mesozoic plate tectonic reconstructions of the central South Atlantic  
1446 Ocean: the role of the West and Central African rift system. *Tectonophysics*, 155(1-4), 181-  
1447 191.
- 1448 Faults, J.E. and Varga, R.J., 1998. The role of accommodation zones and transfer zones in the  
1449 regional segmentation of extended terranes. *Geological Society of America Special Papers*,  
1450 323, pp.1-45.
- 1451 Faults, J., Coolbaugh, M., Bouchot, V., Moek, I. and Oguz, K., 2010, April. Characterizing  
1452 structural controls of geothermal reservoirs in the Great Basin, USA, and Western Turkey:  
1453 developing successful exploration strategies in extended terranes. In *World Geothermal*  
1454 *Congress 2010*, 11-p.
- 1455 Fossen, H., SchulRIZ, R.A., Rundhovde, E., Rotevatn, A. and Buckley, S.J., 2010. Fault linkage  
1456 and graben stepovers in the Canyonlands (Utah) and the North Sea Viking Graben, with  
1457 implications for hydrocarbon migration and accumulation. *AAPG bulletin*, 94(5), 597-613.
- 1458 FriRIZ, H., Abdelsalam, M., Ali, K. A., Bingen, B., Collins, A. S., Fowler, A. R., et al. (2013). Orogen  
1459 styles in the East African Orogen: A review of the Neoproterozoic to Cambrian tectonic  
1460 evolution. *Journal of African Earth Sciences*, 86, 65–106.
- 1461 Gawthorpe, R.L. and Leeder, M.R., 2000. Tectono-sedimentary evolution of active extensional  
1462 basins. *Basin Research*, 12(3-4), 195-218.

- 1463 Gupta, S., Cowie, P.A., Dawers, N.H. and Underhill, J.R., 1998. A mechanism to explain rift-  
1464 basin subsidence and stratigraphic patterns through fault-array evolution. *Geology*, 26(7),  
1465 pp.595-598.
- 1466 GTK Consortium (2012), Explanation of the geology of sheets NA-36-1 and NA-36-5 (Arua  
1467 and Pakwach) 1:250,000, Uganda. Department of Geological Survey and Mines (DGSM),  
1468 Entebbe. 115p.
- 1469 Hans Nelson, C., Karabanov, E.B., Colman, S.M. and Escutia, C., 1999. Tectonic and sediment  
1470 supply control of deep rift lake turbidite systems: Lake Baikal, Russia. *Geology*, 27(2),  
1471 pp.163-166.
- 1472 Heron, P.J., Peace, A.L., McCaffrey, K.J.W., Welford, J.K., Wilson, R., van Hunen, J. and  
1473 Pysklywec, R.N., 2019. Segmentation of rifts through structural inheritance: Creation of the  
1474 Davis Strait. *Tectonics*, 38(7), pp.2411-2430.
- 1475 Hodgson, I., Illsley - Kemp, F., Gallacher, R. J., Keir, D., Ebinger, C. J., & Mtelela, K. (2017).  
1476 Crustal structure at a young continental rift: A receiver function study from the Tanganyika  
1477 Rift. *Tectonics*, 36, 2806–2822.
- 1478 Hovius, N. (1998). Controls on sediment supply by large rivers. In: Relative role of eustasy,  
1479 climate and tectonism in continental rocks: Tulsa, Oklahoma. (Ed. By Shanley, K.W. &  
1480 McCabe, P. J). SEPM Special Publication, 59, 2–16.
- 1481 Jackson, C.A.L., Gawthorpe, R.L., Carr, I.D. and Sharp, I.R., 2005. Normal faulting as a control  
1482 on the stratigraphic development of shallow marine syn-rift sequences: the Nukhul and  
1483 Lower Rudeis Formations, Hammam Faraun fault block, Suez Rift, Egypt. *Sedimentology*,  
1484 52(2), pp.313-338.
- 1485 Katumwehe, A.B., Abdelsalam, M.G. and Atekwana, E.A., 2015. The role of pre-existing  
1486 Precambrian structures in rift evolution: The Albertine and Rhino grabens, Uganda.  
1487 *Tectonophysics*, 646, pp.117-129.
- 1488 Katumwehe, A.B., Abdelsalam, M.G., Atekwana, E.A. and Laó-Dávila, D.A., 2016. Extent,  
1489 kinematics and tectonic origin of the Precambrian Aswa Shear Zone in eastern Africa.  
1490 *Gondwana Research*, 34, pp.241-253.
- 1491 Kidane, T., Courtillot, V., Manighetti, I., Audin, L., Lahitte, P., Quidelleur, X., Gillot, P.Y., Gallet,  
1492 Y., Carlot, J. and Haile, T., 2003. New paleomagnetic and geochronologic results from  
1493 Ethiopian Afar: Block rotations linked to rift overlap and propagation and determination of  
1494 a ~ 2 Ma reference pole for stable Africa. *Journal of Geophysical Research: Solid Earth*,  
1495 108(B2).
- 1496 Kim, Y.S., Peacock, D.C. and Sanderson, D.J., 2004. Fault damage zones. *Journal of structural  
1497 geology*, 26(3), pp.503-517.
- 1498 Koehn, D., Aanyu, K., Haines, S. and Sachau, T., 2008. Rift nucleation, rift propagation and the  
1499 creation of basement micro-plates within active rifts. *Tectonophysics*, 458(1-4), 105-116.

- 1500 Kolawole, F., Atekwana, E.A., Laó-Dávila, D.A., Abdelsalam, M.G., Chindandali, P.R., Salima, J.  
 1501 and Kalindekafe, L., 2018. Active deformation of Malawi rift's north basin Hinge zone  
 1502 modulated by reactivation of preexisting Precambrian Shear zone fabric. *Tectonics*, 37(3),  
 1503 pp.683-704.
- 1504 Kranz, R.L., 1979, February. Crack-crack and crack-pore interactions in stressed granite. In  
 1505 *International Journal of Rock Mechanics and Mining Sciences & Geomechanics Abstracts*  
 1506 (Vol. 16, No. 1, pp. 37-47). Pergamon.
- 1507 Lambiase, J.J. and Bosworth, W., 1995. Structural controls on sedimentation in continental  
 1508 rifts. *Geological Society, London, Special Publications*, 80(1), 117-144.
- 1509 La Rosa, A., Pagli, C., Keir, D., Sani, F., Corti, G., Wang, H. and Possee, D., 2019. Observing  
 1510 Oblique Slip During Rift Linkage in Northern Afar. *Geophysical Research Letters*, 46(19),  
 1511 10782-10790.
- 1512 Lavayssière, A. J., Drooff, C. J., Ebinger, C. J., Gallacher, R. J., Illsley-Kemp, F. J., Oliva, S. J., &  
 1513 Keir, D. J. (2019). Depth Extent and Kinematics of Faulting in the Southern Tanganyika Rift,  
 1514 Africa. *Tectonics*, 38(3), 842–862. doi: 10.1029/2018tc005379.
- 1515 Lazarus, E. D., and Constantine, J. A. (2013). Generic theory for channel sinuosity.  
 1516 *Proceedings of the National Academy of Sciences*, 110(21), pp.8447-8452.
- 1517 Lyons, R. P., Scholz, C. A., Cohen, A. S., King, J. W., Brown, E. T., Ivory, S. J., et al. (2015).  
 1518 Continuous 1.3-million-year record of East African hydroclimate, and implications for  
 1519 patterns of evolution and biodiversity. *Proceedings of the National Academy of Sciences of*  
 1520 *the United States of America*, 112(51), 15,568-15,573.
- 1521 Ma, G. Q., Du, X. J., Li, L. L., & Meng, L. S. (2012). Interpretation of magnetic anomalies by  
 1522 horizontal and vertical derivatives of the analytic signal. *Applied Geophysics*, 9(4), 468–474.  
 1523 <https://doi.org/10.1007/s11770-012-0350-4>.
- 1524 Mack, G.H., Seager, W.R., Leeder, M.R., Perez-Arlucea, M. and Salyards, S.L., 2006. Pliocene  
 1525 and Quaternary history of the Rio Grande, the axial river of the southern Rio Grande rift, New  
 1526 Mexico, USA. *Earth-Science Reviews*, 79(1-2), pp.141-162.
- 1527 Mardia, K. V., and Jupp, P. E., 2009. *Directional statistics*. Vol. 494, John Wiley & Sons, West  
 1528 Sussex, England.
- 1529 Molnar, N.E., Cruden, A.R. and Betts, P.G., 2018. Unzipping continents and the birth of  
 1530 microcontinents. *Geology*, 46(5), pp.451-454.
- 1531 Mondy, L.S., Rey, P.F., Duclaux, G. and Moresi, L., 2018. The role of asthenospheric flow during  
 1532 rift propagation and breakup. *Geology*, 46(2), pp.103-106.
- 1533 Molnar, N.E., Cruden, A.R. and Betts, P.G., 2019. Interactions between propagating rifts and  
 1534 linear weaknesses in the lower crust. *Geosphere*, 15(5), 1617-1640.
- 1535 Morley, C.K., 1999, Aspects of Transfer Zone Geometry and Evolution in East African Rifts, in  
 1536 C.K. Morley ed., *Geoscience of Rift Systems—Evolution of East Africa: AAPG Studies in*  
 1537 *Geology No. 44*, 161–171.

- 1538 Morley, C. K. (2010). Stress re-orientation along zones of weak fabrics in rifts: An explanation  
1539 for pure extension in 'oblique' rift segments? *Earth and Planetary Science Letters*, 297(3),  
1540 667–673.
- 1541 Morley, C.K., 2020. Early syn-rift igneous dike patterns, northern Kenya Rift (Turkana,  
1542 Kenya): Implications for local and regional stresses, tectonics, and magma-structure  
1543 interactions. *Geosphere*, 16(3), 890-918.
- 1544 Morley, C. K., Cunningham, S. M., Harper, R. M. and Wescott, W. A. (1992). Geology and  
1545 geophysics of the Rukwa rift, East Africa. *Tectonics*, 11(1), pp.69-81.
- 1546 Morley, C.K., Nelson, R.A., Patton, T.L. and Munn, S.G., 1990. Transfer zones in the East African  
1547 rift system and their relevance to hydrocarbon exploration in rifts. *AAPG bulletin*, 74(8),  
1548 1234-1253.
- 1549 Muirhead, J.D., Kattenhorn, S.A. and Le Corvec, N., 2015. Varying styles of magmatic strain  
1550 accommodation across the East African Rift. *Geochemistry, Geophysics, Geosystems*, 16(8),  
1551 pp.2775-2795.
- 1552 Muirhead, J. D., Wright, L. J., & Scholz, C. A. (2019). Rift evolution in regions of low magma  
1553 input in East Africa. *Earth and Planetary Science Letters*, 506, 332–346.
- 1554 Musila, M., Ebinger, C. J., Mwangi, S., Kianji, G., Ayele, A., Mariita, N., Bastow, I. D., Bendick, R.  
1555 O., 2020. Kinematics of linkage between the Main Ethiopian and Eastern rifts in the Turkana  
1556 Depression. AGU Fall Meeting abstract #T024-0004.
- 1557 Nelson, R.A., Patton, T.L. and Morley, C.K., 1992. Rift-segment interaction and its relation to  
1558 hydrocarbon exploration in continental rift systems (1). *AAPG bulletin*, 76(8), pp.1153-1169.
- 1559 Neuharth, D., Brune, S., Glerum, A., Heine, C. and Welford, J.K., 2021. Formation of continental  
1560 microplates through rift linkage: Numerical modelling and its application to the Flemish Cap  
1561 and Sao Paulo Plateau. *Geochemistry, Geophysics, Geosystems*, p.e2020GC009615.
- 1562 Ngalamo, J.F.G., Kolawole, F., Sobh, M. and Atekwana, E.A. (2020). Partitioning of Extension  
1563 at the Propagating Tips of Continental Rifts: Insights from the Central and East African Rift  
1564 Systems. AGU Fall Meeting Abstract #T028-06.
- 1565 Njinju, E.A., Kolawole, F., Atekwana, E.A., Stamps, D.S., Atekwana, E.A., Abdelsalam, M.G. and  
1566 Mickus, K.L., 2019a. Terrestrial heat flow in the Malawi Rifted Zone, East Africa: Implications  
1567 for tectono-thermal inheritance in continental rift basins. *Journal of Volcanology and  
1568 Geothermal Research*, 387, p.106656.
- 1569 Njinju, E.A., Atekwana, E.A., Stamps, D.S., Abdelsalam, M.G., Atekwana, E.A., Mickus, K.L.,  
1570 Fishwick, S., Kolawole, F., Rajaonarison, T.A. and Nyalugwe, V.N., 2019b. Lithospheric  
1571 structure of the Malawi rift: implications for magma - poor rifting processes. *Tectonics*,  
1572 38(11), pp.3835-3853.
- 1573 Nyalugwe, V.N., Abdelsalam, M.G., Atekwana, E.A., Katumwehe, A., Mickus, K.L., Salima, J.,  
1574 Njinju, E.A. and Emishaw, L., (2019a). Lithospheric structure beneath the Cretaceous Chilwa  
1575 Alkaline Province (CAP) in southern Malawi and northeastern Mozambique. *Journal of  
1576 Geophysical Research: Solid Earth*, 124(11), pp.12224-12240.

- 1577 Nyalugwe, V.; Abdelsalam, M.; Atekwana, E.; Katumwehe, A.; Mickus, K.; Salima, J.; Njinju, E.  
 1578 and L. Emishaw, (2019b). 2013 Total Magnetic Intensity (TMI) gridded aeromagnetic data  
 1579 of southern Malawi 34 45 E – 36 00 E and 14 45 S and 16 15 S (investigator Mohamed  
 1580 Abdelsalam). Integrated Earth Data Applications (IEDA). doi:10.1594/IEDA/324860.
- 1581 Nyalugwe, V.N., Abdelsalam, M.G., Katumwehe, A., Mickus, K.L. and Atekwana, E.A., 2020.  
 1582 Structure and tectonic setting of the Chingale Igneous Ring Complex, Malawi from  
 1583 aeromagnetic and satellite gravity data: Implication for Precambrian terranes collision and  
 1584 Neogene-Quaternary rifting. *Journal of African Earth Sciences*, 163, p.103760.
- 1585 Pagli, C., Yun, S.H., Ebinger, C., Keir, D. and Wang, H., 2019. Strike-slip tectonics during rift  
 1586 linkage. *Geology*, 47(1), pp.31-34.
- 1587 Perrin, C., Manighetti, I. and Gaudemer, Y., 2016. Off-fault tip splay networks: A genetic and  
 1588 generic property of faults indicative of their long-term propagation. *Comptes Rendus*  
 1589 *Geoscience*, 348(1), pp.52-60.
- 1590 Phillips, T.B. and McCaffrey, K.J., 2019. Terrane Boundary Reactivation, Barriers to Lateral  
 1591 Fault Propagation and Reactivated Fabrics: Rifting Across the Median Batholith Zone, Great  
 1592 South Basin, New Zealand. *Tectonics*, 38(11), pp.4027-4053.
- 1593 Ring, U., 1995. Tectonic and lithological constraints on the evolution of the Karoo graben of  
 1594 northern Malawi (East Africa). *Geologische Rundschau*, 84(3), 607-625.
- 1595 Roberts, E.M., Stevens, N.J., O'Connor, P.M., Dirks, P.H.G.M., Gottfried, M.D., Clyde, W.C.,  
 1596 Armstrong, R.A., Kemp, A.I.S. and Hemming, S., 2012. Initiation of the western branch of the  
 1597 East African Rift coeval with the eastern branch. *Nature Geoscience*, 5(4), pp.289-294.
- 1598 Rosendahl, B.R., 1987. Architecture of continental rifts with special reference to East Africa.  
 1599 *Annual Review of Earth and Planetary Sciences*, 15, p.445.
- 1600 Rotevatn, A., Kristensen, T.B., Ksienzyk, A.K., Wemmer, K., Henstra, G.A., Midtkandal, I.,  
 1601 Grundvåg, S.A. and Andresen, A., 2018. Structural inheritance and rapid rift-length  
 1602 establishment in a multiphase rift: The East Greenland rift system and its Caledonian  
 1603 orogenic ancestry. *Tectonics*, 37(6), pp.1858-1875.
- 1604 Ryan, W. B. F., S.M. Carbotte, J. Coplan, S. O'Hara, A. Melkonian, R. Arko, R.A. Weissel, V.  
 1605 Ferrini, A. Goodwillie, F. Nitsche, J. Bonczkowski, and R. Zemsky (2009), Global Multi-  
 1606 Resolution Topography (GMRT) synthesis data set, *Geochem. Geophys. Geosyst.*, 10, Q03014.
- 1607 Roberts, E.M., Stevens, N.J., O'Connor, P.M., Dirks, P.H.G.M., Gottfried, M.D., Clyde, W.C.,  
 1608 Armstrong, R.A., Kemp, A.I.S. and Hemming, S., 2012. Initiation of the western branch of the  
 1609 East African Rift coeval with the eastern branch. *Nature Geoscience*, 5(4), pp.289-294.
- 1610 Saria, E., Calais, E., Stamps, D.S., Delvaux, D. and Hartnady, C.J.H., 2014. Present-day  
 1611 kinematics of the East African Rift. *Journal of Geophysical Research: Solid Earth*, 119(4),  
 1612 pp.3584-3600.
- 1613 Simon, B., Guillocheau, F., Robin, C., Dauteuil, O., Nalpas, T., Pickford, M., Senut, B., Lays, P.,  
 1614 Bourges, P. and Bez, M., 2017. Deformation and sedimentary evolution of the Lake Albert Rift  
 1615 (Uganda, East African rift system). *Marine and Petroleum Geology*, 86, pp.17-37.

- 1616 Scholz, C.A., Shillington, D.J., Wright, L.J., Accardo, N., Gaherty, J.B. and Chindandali, P., 2020.  
 1617 Intrarift fault fabric, segmentation, and basin evolution of the Lake Malawi (Nyasa) Rift, East  
 1618 Africa. *Geosphere*, 16(5), 1293-1311.
- 1619 Soreghan, M.J. and Cohen, A.S., 1996. Textural and compositional variability across littoral  
 1620 segments of Lake Tanganyika: the effect of asymmetric basin structure on sedimentation in  
 1621 large rift lakes. *AAPG bulletin*, 80(3), pp.382-408.
- 1622 Soreghan, M.J., Scholz, C.A. and Wells, J.T., 1999. Coarse-grained, deep-water sedimentation  
 1623 along a border fault margin of Lake Malawi, Africa; seismic stratigraphic analysis. *Journal of*  
 1624 *Sedimentary Research*, 69(4), pp.832-846.
- 1625 Specht, T.D. and Rosendahl, B.R., 1989. Architecture of the Lake Malawi rift, east Africa.  
 1626 *Journal of African Earth Sciences (and the Middle East)*, 8(2-4), pp.355-382.
- 1627 Taylor, S.K., Bull, J.M., Lamarche, G. and Barnes, P.M., 2004. Normal fault growth and linkage  
 1628 in the Whakatane Graben, New Zealand, during the last 1.3 Myr. *Journal of Geophysical*  
 1629 *Research: Solid Earth*, 109(B2).
- 1630 Thomas D. S. G., Bailey, R., Shaw, P. A., Durcan, J. A., & Singarayer, J. S. (2009). Late  
 1631 Quaternary highstands at Lake Chilwa, Malawi: Frequency, timing and possible forcing  
 1632 mechanisms in the last 44 ka. *Quaternary Science Reviews*, 28, 526–539.
- 1633 Tiercelin, J.J., Soreghan, M., Cohen, A.S., Lezzar, K.E. and Bouroulllec, J.L., 1992. Sedimentation  
 1634 in large rift lakes: example from the Middle Pleistocene—Modern deposits of the Tanganyika  
 1635 Trough, East African Rift System. *Bull. Centres Rech. Explor.-Prod. Elf Aquitaine*, 16, pp.83-  
 1636 111.
- 1637 Vittori, E., Delvaux, D. and Kervyn, F., 1997. Kanda fault: A major seismogenic element west  
 1638 of the Rukwa Rift (Tanzania, East Africa). *Journal of Geodynamics*, 24(1-4), pp.139-153.
- 1639 Wang, L., Maestrelli, D., Corti, G., Zou, Y. and Shen, C., 2021. Normal fault reactivation during  
 1640 multiphase extension: Analogue models and application to the Turkana depression, East  
 1641 Africa. *Tectonophysics*, p.228870.
- 1642 Wedmore, L., Biggs, J., Williams, J., Fagereng, A., Dulanya, Z., Mphepo, F. and Mdala, H. (2020).  
 1643 Active fault scarps in southern Malawi and their implications for the distribution of strain in  
 1644 incipient continental rifts. *Tectonics*, 39, e2019TC005834.
- 1645 Westerhof, A.B., Härmä, P., Isabirye, E., Katto, E., Koistinen, T., Kuosmanen, E., Lehto, T.,  
 1646 Lehtonen, M.I., Mäkitie, H., Manninen, T. and Mänttari, I. (2014). Geology and geodynamic  
 1647 development of Uganda with explanation of the 1:1,000,000 scale geological map. Geological  
 1648 survey of Finland.
- 1649 Williams, J.N., Fagereng, Å., Wedmore, L.N., Biggs, J., Mphepo, F., Dulanya, Z., Mdala, H. and  
 1650 Blenkinsop, T., 2019. How do variably striking faults reactivate during rifting? Insights from  
 1651 southern Malawi. *Geochemistry, Geophysics, Geosystems*, 20(7), pp.3588-3607.
- 1652 Wilson, T.J., 1999. Cenozoic structural segmentation of the Transantarctic Mountains rift  
 1653 flank in southern Victoria Land. *Global and Planetary Change*, 23(1-4), 105-127.

1654 Woolley, A.R., 2001. Alkaline Rocks and Carbonatites of the World. Part 3: Africa. The  
1655 Geological Society, London, p. 372.

1656 Wright, L.J., Muirhead, J.D. and Scholz, C.A., 2020. Spatio-temporal variations in upper crustal  
1657 extension across the different basement terranes of the Lake Tanganyika Rift, East Africa.  
1658 Tectonics.

1659 Zondervan, J.R., Stokes, M., Boulton, S.J., Telfer, M.W. and Mather, A.E., 2020. Rock strength  
1660 and structural controls on fluvial erodibility: Implications for drainage divide mobility in a  
1661 collisional mountain belt. Earth and Planetary Science Letters, 538, p.116221.

1662 Zwaan, F., Schreurs, G., Naliboff, J., & Buiter, S. J. (2016). Insights into the effects of oblique  
1663 extension on continental rift interaction from 3D analogue and numerical models.  
1664 Tectonophysics, 693, 239–260.

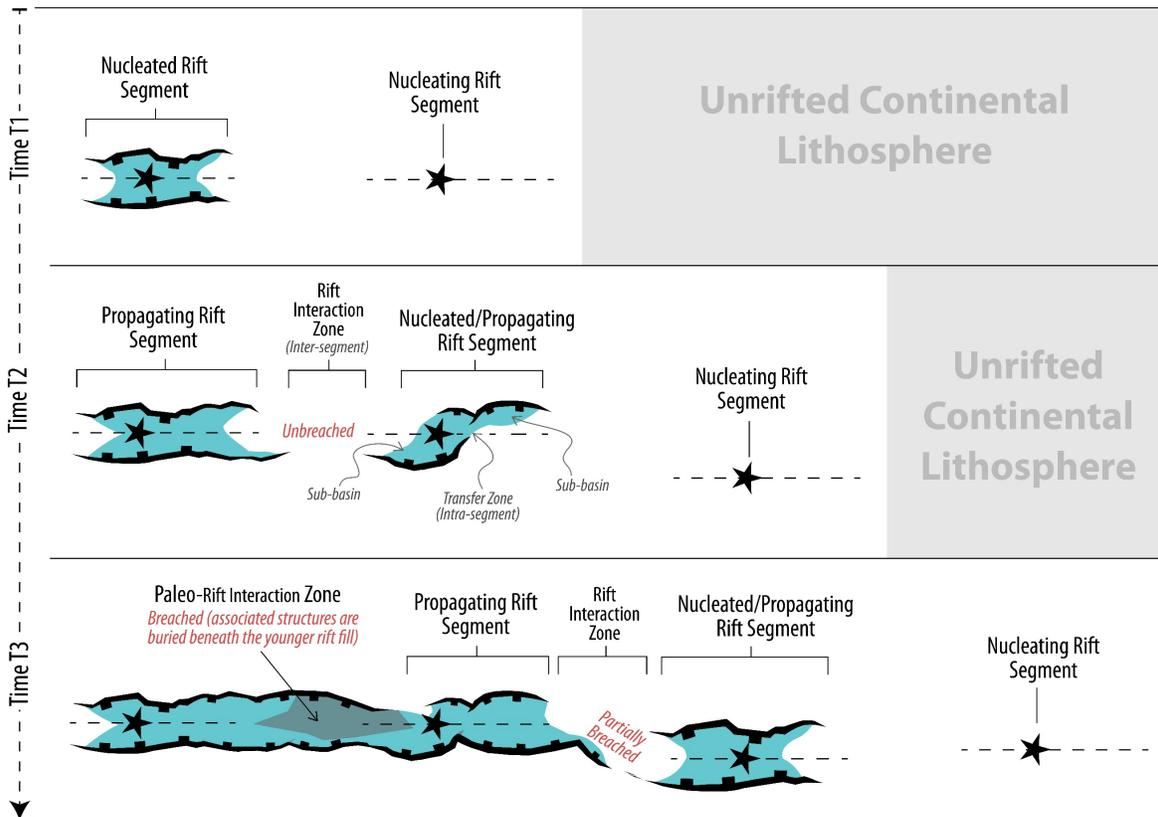
1665 Zwaan, F. and Schreurs, G., 2020. Rift segment interaction in orthogonal and rotational  
1666 extension experiments: Implications for the large-scale development of rift systems. Journal  
1667 of structural geology, 140, p.104119.

1668

1669

1670

1671



1673 **Figure 1:** Simple model of nucleation and growth of rift segments along continental rift  
 1674 systems (modified after Nelson et al., 1992). Rift axes are represented by the black  
 1675 stars/dashed lines. Note that this cartoon only features collinear and underlapping parallel  
 1676 rift segments. For each zone of rift segment interaction, the cartoon illustrates the pre- and  
 1677 post-linkage geometries of the rift zones. Also, note that schematic represents rift  
 1678 segmentation at the early stages (stretching stage) of continental rifting; the black stars only  
 1679 represent hypothetical zones of rift nucleation (not spreading center as implied in Nelson et  
 1680 al., 1992).

1681  
 1682  
 1683  
 1684  
 1685  
 1686

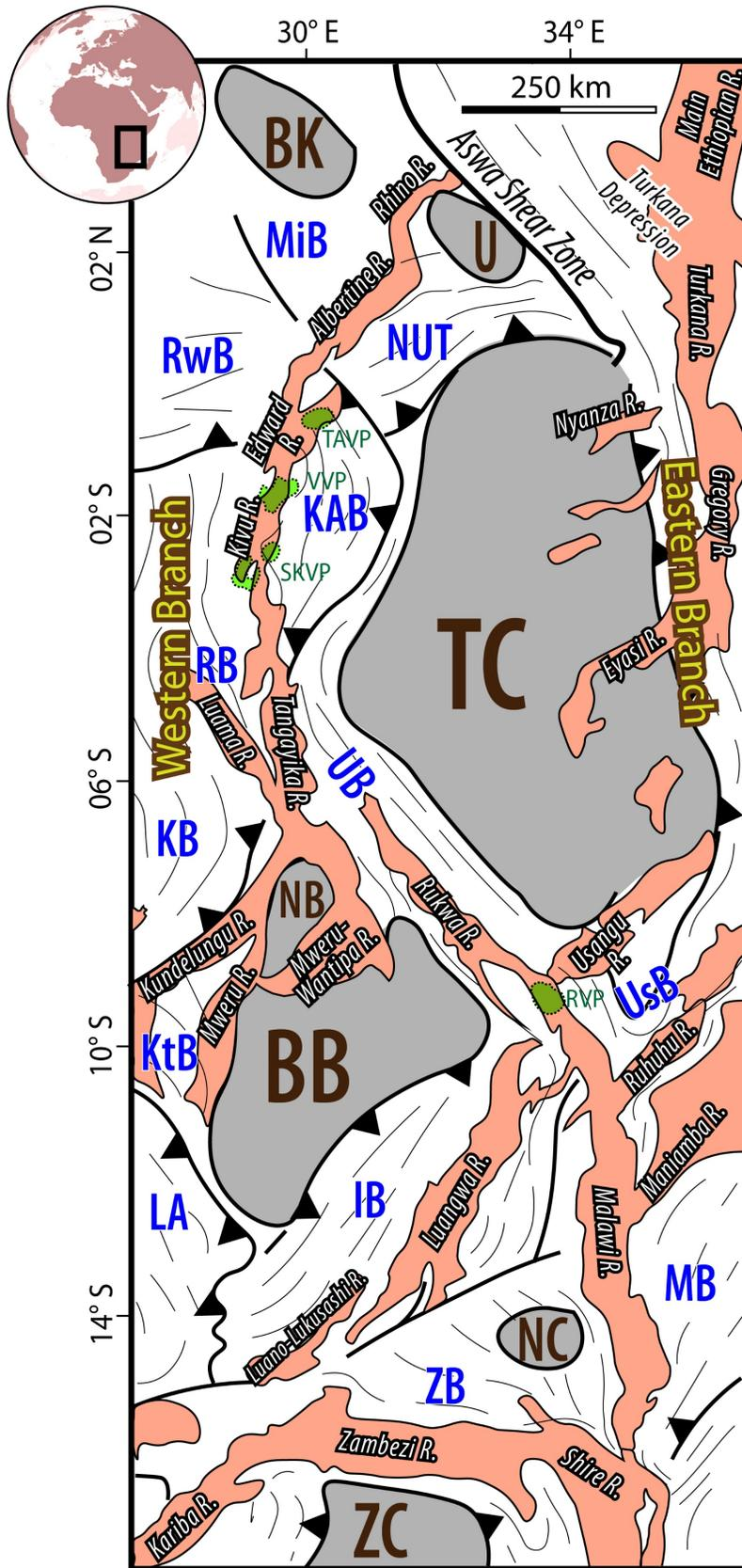
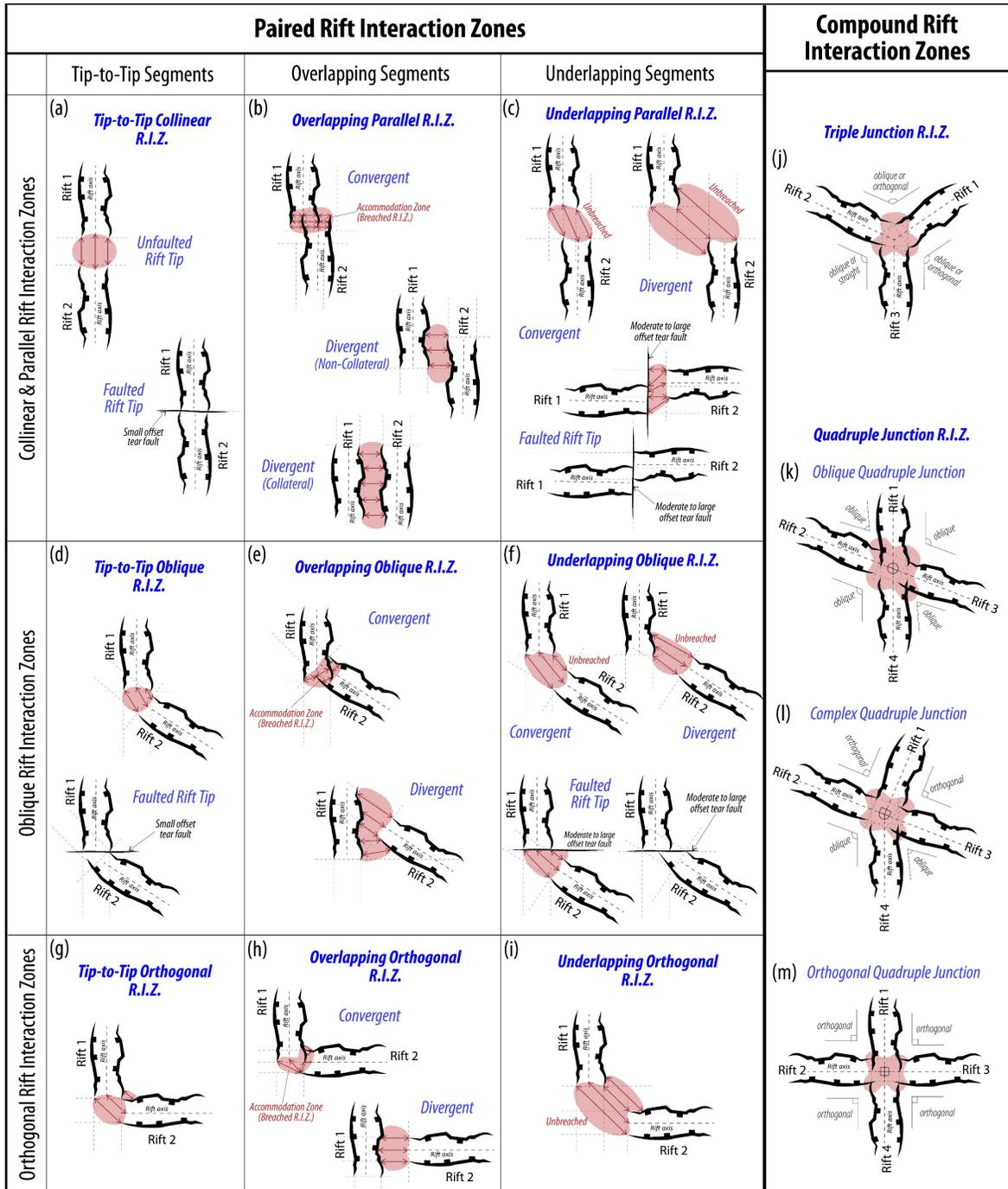


**Figure 2:** Map of eastern Africa showing the Precambrian basement orogenic belts with their large-scale fabric trends, cratonic blocks (grey), and rift basins (pink; includes both Mesozoic and Cenozoic rifts) modified after Daly et al. (1989). The cratons include the BB (Bangweulu Block), BK (Bomukibalia Block), NC (Niassa Craton), TC (Tanzanian Craton), U (Uganda Craton), and ZC (Zimbabwe Craton). The mobile belts include IB (Irumide Belt), KAB (Karagwe-Ankole Belt), KB (Kibaran Belt), LA (Lufillian Arc), MB (Mozambique Belt), MiB (Madi-Igisi Belt), NB (North Bangweulu Microplate), NUT (North Uganda Terrane), RB (Ruzizian Belt), RwB (Ruwendzori Belt), UB (Ubendian Belt), UsB (Usagaran Belt), ZB (Zambezi Belt). Active volcanic centers along the Western Branch of the East African Rift System (green polygons) are RVP (Rungwe Volcanic Province), SKVP (South Kivu Volcanic Province), TAVP (Toro-Ankole Volcanic Province), VVP (Virunga Volcanic Province).

1726  
1727  
1728  
1729  
1730  
1731  
1732  
1733  
1734  
1735  
1736  
1737  
1738  
1739  
1740  
1741  
1742  
1743  
1744  
1745  
1746



 Rift-bounding fault       Cross-over region between interacting rift segments, across which breaching faults may develop.       Breaching Distance: Lateral extents between the primary structural domains of the interacting rifts (border fault & intrabasin zones).

1747 **Figure 3:** Classification of rift interaction zones (RIZ). The structures are not drawn to scale,  
1748 but they are illustrated to represent rift segment-scale features. This broader classification  
1749 is based on a review and update of the previously published classification by Nelson et al.  
1750 (1992), other geometries observable in several continental rift systems (including the East  
1751 African Rift System). Note that the rift segments, although presented as grabens, can also be  
1752 half-grabens. The faults shown are basin-bounding fault systems.



1780 RIZ): Butiaba Rift Interaction Zone (Albertine-Rhino RIZ), CSZ: Chisi Suture Zone, CLCM-RIZ:  
1781 Central Luangwa-Central Malawi Rift Interaction Zone, ER: Eyasi Rift, GR: Gregory Rift, HR:  
1782 Henga Rift, KbR: Kabompo Rift, KdR: Kundelungu Rift, KfR: Kafue Rift, KH: Kabumbi Horst,  
1783 KL-RIZ: Kundelungu-Luapula Rift Interaction Zone, KM-RIZ: Kundelungu-Mweru Trasfer  
1784 Zone, KR: Kivu Rift, Kr: Kariba Rift, LkR: Lukusashi Rift; LGG: Lake George Graben, LK-RIZ:  
1785 Luano-Kafue Rift Interaction Zone, LL-RIZ: Luangwa-Luano Rift Interaction Zone, LpR:  
1786 Luapula Rift, LsR: Luansanza Rift, LT-RIZ: Luama-Tanganyika Rift Interaction Zone, LuF:  
1787 Lufira Fault, LuL-RIZ: Luano-Lukusashi Rift Interaction Zone; LuR: Luano Rift, LR: Luangwa  
1788 Rift, LmR: Luama Rift, MG: Malombe Graben, MgSZ: Mughesse Shear Zone, MH: Mbozi Horst,  
1789 MkT: Makanjira Trough, MM-RIZ: Maniamba-Malawi Rift Interaction Zone, MnR: Maniamba  
1790 Rift (a.k.a. Metangula Rift), MR: Malawi Rift, MSZ: Mwembeshi Shear Zone, MT: Msongano  
1791 Trough, MRIZ: Mweru Wantipa Rift Interaction Zone, MuR: Muchili Rift, MwR: Mweru Rift,  
1792 MWR: Mweru-Wantipa Rift, MyR: Manyara Rift, NLNM-RIZ: North Luangwa-North Malawi  
1793 Rift Interaction Zone, NR: Nyanza Rift, NRR: North Rukuru-Mwesia Rift, NTR-RIZ: North  
1794 Tanganyika-Rukwa Rift Interaction Zone, RH: Rwenzori Horst, RhR: Rhino Rift, RM-RIZ:  
1795 Ruhuhu-Malawi Rift Interaction Zone, RR: Rukwa Rift, RuR: Ruhuhu Rift, RVP: Rungwe  
1796 Volcanic Province, SG: Semiliki Graben, SH: Shire Horst, SKVP: South Kivu Volcanic Province,  
1797 SMS-RIZ: South Malawi-Shire Rift Interaction Zone, SRZ: Shire Rift Zone, SSZ: Sanangoè Shear  
1798 Zone, ST: Songwe Trough, STR-RIZ: South Tanganyika-Rukwa Rift Interaction Zone, SU-RIZ:  
1799 Shire-Urema Rift Interaction Zone, TkR: Turkana Rift, TM-RIZ: Tanganyika-Mweru Wantipa  
1800 Rift Interaction Zone, TR: Tanganyika Rift, TAVP: Toro-Ankole Volcanic Province, UH:  
1801 Ubwari Horst, UK-RIZ: Upemba-Kundelungu Trasfer Zone (Kundelungu Horst), UpR:  
1802 Upemba Rift, UR: Usangu Rift, UrR: Urema Rift, VVP: Virunga Volcanic Province, WR:  
1803 Wembere Rift, ZK-RIZ: Zambezi-Kafue Rift Interaction Zone, ZKr-RIZ: Zambezi-Kariba Rift  
1804 Interaction Zone, ZS-RIZ: Zambezi-Shire Rift Interaction Zone, ZR: Zambezi Rift. Map Source:  
1805 Global Multi-Resolution Topography (GMRT) digital elevation model (Ryan et al., 2009). (b  
1806 – f) GMRT Topographic profiles across some of the non-magmatic WB-EARS rift interaction  
1807 zones, highlighting the major categories of long-wavelength cross-over relief geometries  
1808 (red curves) that are observed.

1809

1810

1811

1812

1813

1814

1815

1816

1817

1818  
 1819  
 1820  
 1821  
 1822  
 1823  
 1824  
 1825  
 1826  
 1827  
 1828  
 1829  
 1830  
 1831  
 1832  
 1833  
 1834  
 1835  
 1836  
 1837  
 1838  
 1839  
 1840  
 1841  
 1842  
 1843  
 1844  
 1845  
 1846  
 1847  
 1848  
 1849  
 1850  
 1851  
 1852  
 1853  
 1854  
 1855  
 1856  
 1857  
 1858  
 1859  
 1860  
 1861

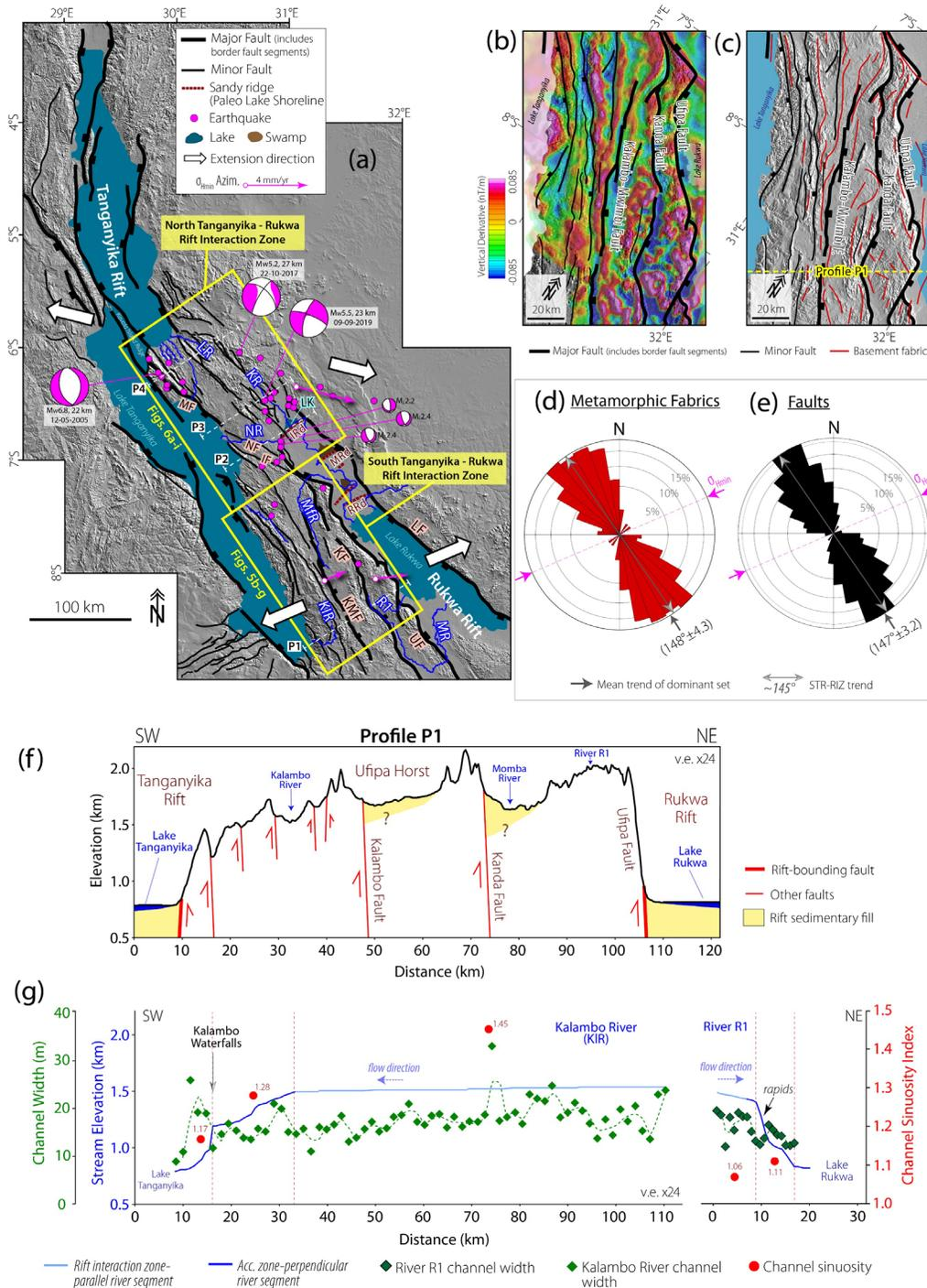


**Figure 5: South Tanganyika-Rukwa Rift Interaction Zone, STR-RIZ (Parallel Overlapping Divergent RIZ).** (a.) Satellite Digital Elevation Model (DEM) hillshade map of the Tanganyika Rift and the Rukwa Rift. Earthquake epicenters (Mw3.7 - 7.3) and focal mechanism solutions are from USGS and Global CMT catalogs, and Lavayssiere et al. (2019). Crustal stretching velocity (green arrows) with 95% uncertainty ellipses are from Stamps et al. (2018). IRd = Ilyandi Ridge, IF = Ifume Fault, KF = Kanda Fault System, KIR = Kalambo

1862 River, KMF = Kalambo-Mwimbi Fault System, KR = Kavuu River, LF = Lupa Fault, LK = Lake  
1863 Katavi, LR = Luegele River, MF = Mahale Fault, MfR = Mfuizi River, MR = Momba River, MRd  
1864 = Maimba Ridge, NF = Nkamba Fault, NR = Nkamba River, RRd = Rungwa Ridge, UF = Ufipa  
1865 Fault. Locations of the paleo-lake shore ridges are from Delvaux et al. (1998). Tanganyika  
1866 Rift faults are from Muirhead et al. (2018). (b) Filtered aeromagnetic grid of the STR-RIZ,  
1867 overlaid on the hillshade DEM showing the magnetic fabrics of the basement. (c) Satellite  
1868 DEM hillshade map overlaid with interpretation of the interpreted basement fabrics. (d)  
1869 Frequency-azimuth distribution of the aeromagnetic basement fabrics in Figure 3c. (e)  
1870 Frequency-azimuth distribution of the mapped faults along the rift interaction zone (Figure  
1871 3c). (f) Rift-orthogonal topographic profile across the rift interaction zone. (g) Longitudinal  
1872 stream profiles for representative axial streams in the rift interaction zone (Kalambo River  
1873 and an unnamed river R1).

1874  
1875

1876

1877

1878

1879

1880

1881

1882

1883

1884

1885

1886

1887

1888

1889

1890



1916 **Figure 6: North Tanganyika–Rukwa Rift Interaction Zone, NTR-RIZ (Overlapping**  
1917 **Oblique Divergent RIZ).** (a.) Filtered aeromagnetic grid of the NTR-RIZ, overlaid on satellite  
1918 digital elevation model (DEM) hillshade map showing the magnetic fabrics of the basement.  
1919 (b) Satellite digital elevation model (DEM) hillshade map overlaid with interpretations of the  
1920 interpreted basement fabrics. (c) Frequency-azimuth distribution of the aeromagnetic  
1921 basement fabrics in Figure 4b. (d) Frequency-azimuth distribution of the mapped faults  
1922 along the rift interaction zone (Figure 4b). (e – g) Rift-orthogonal topographic profiles  
1923 showing the southeast to northwest transition from a single broad rift geometry, through a  
1924 multi-trough geometry, and attenuating into a zone of diffused faulting. (h) Interaction zone-  
1925 parallel topographic profile showing the salient anomalies that characterize the morphology  
1926 of the rift interaction zone. (i) Longitudinal stream profiles for the main axial streams that  
1927 intersect the profile transect (Kavuu and Luegele Rivers).

1928

1929

1930

1931

1932

1933

1934

1935

1936

1937

1938

1939

1940

1941

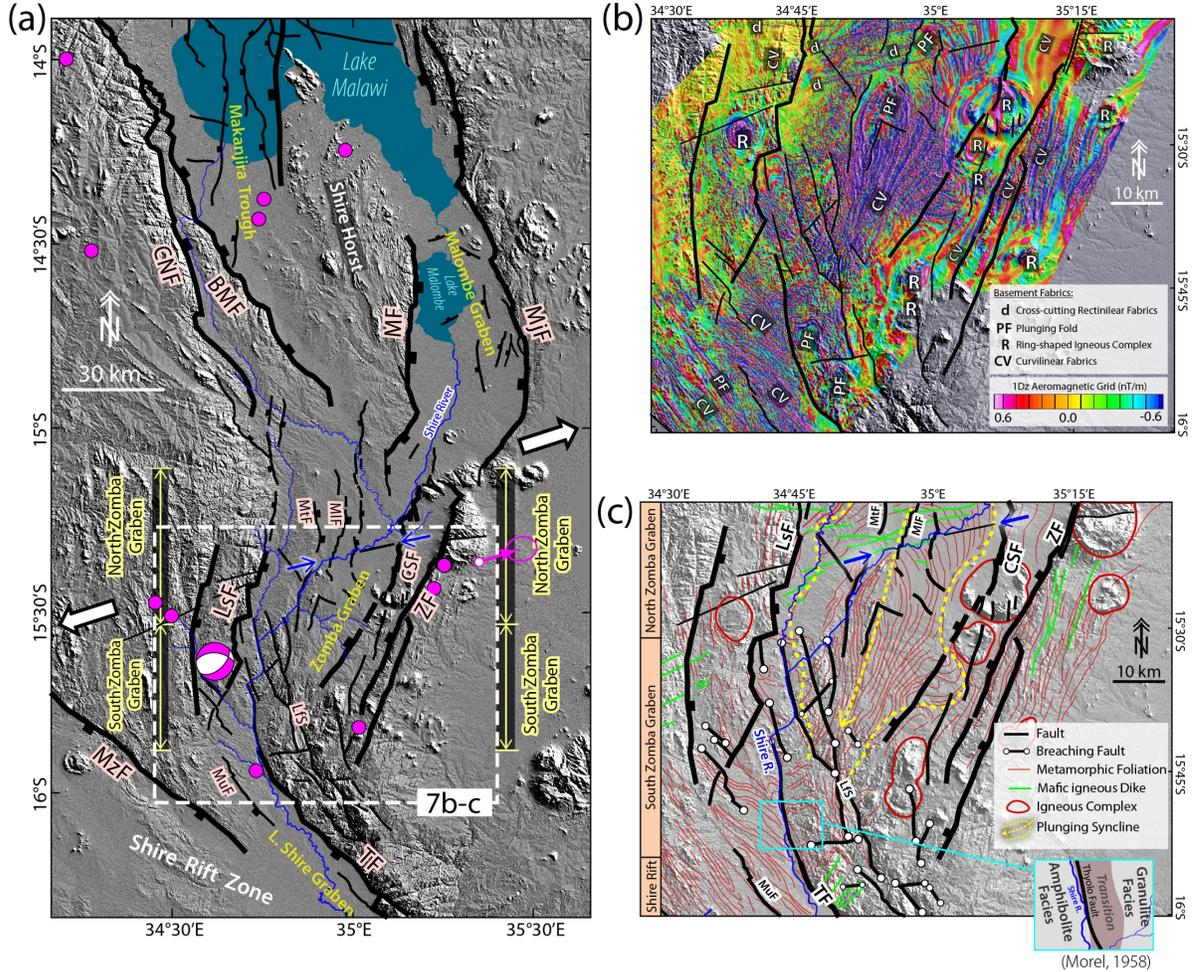
1942

1943

1944

1945

1946  
1947  
1948  
1949  
1950  
1951  
1952  
1953  
1954  
1955  
1956  
1957  
1958  
1959  
1960  
1961  
1962  
1963  
1964  
1965  
1966  
1967



1968 **Figure 7: South Malawi–Shire Rift Interaction Zone, SMS-RIZ (Overlapping Oblique**  
1969 **Divergent RIZ).** (a.) Satellite Digital Elevation Model (DEM) hillshade map with fault  
1970 interpretations of the southern Malawi Rift and the northeastern part of the Shire Rift Zone.  
1971 Fault lineaments are obtained from the satellite DEM and filtered aeromagnetic data  
1972 interpretation (this study), and previously published satellite DEM and field study  
1973 (Wedmore et al., 2020). Crustal stretching velocity (green arrow) with 95% uncertainty

1974 ellipse is from Stamps et al. (2018). BMF = Bilila-Mtakataka Fault, CNF = Chirobwe-Ncheu  
1975 Fault, LfS = Lukhubula Fault System, LsF = Lisungwe Fault, MF = Malombe Fault, Mlf =  
1976 Mlungusi Fault, MtF = Mtsimukwe Fault, MuF = Mtumba Fault, MjF = Mwanjage Fault, MzF =  
1977 Mwanza Fault, TF = Thyolo Fault, CSF = Chingale Step Fault, ZF = Zomba Fault. (b) Satellite  
1978 DEM Hillshade map overlaid with filtered aeromagnetic grid of the rift interaction zone. (c)  
1979 Interpretation of basement fabrics and faults from 7a and 7b. (d - e) Frequency-azimuth  
1980 distribution of the rift faults and the inherited pre-rift basement metamorphic fabrics in the  
1981 northern (North Zomba) and southern (South Zomba) domains of the rift interaction zone.

1982

1983

1984

1985

1986

1987

1988

1989

1990

1991

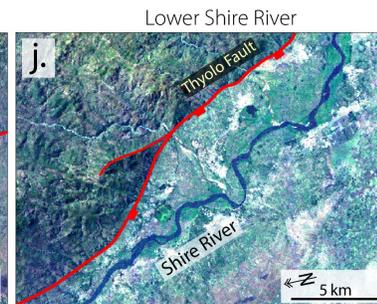
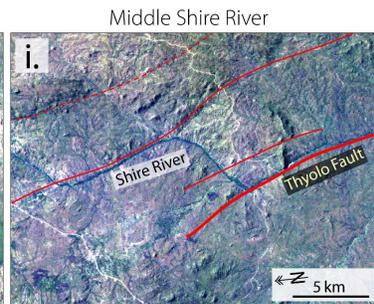
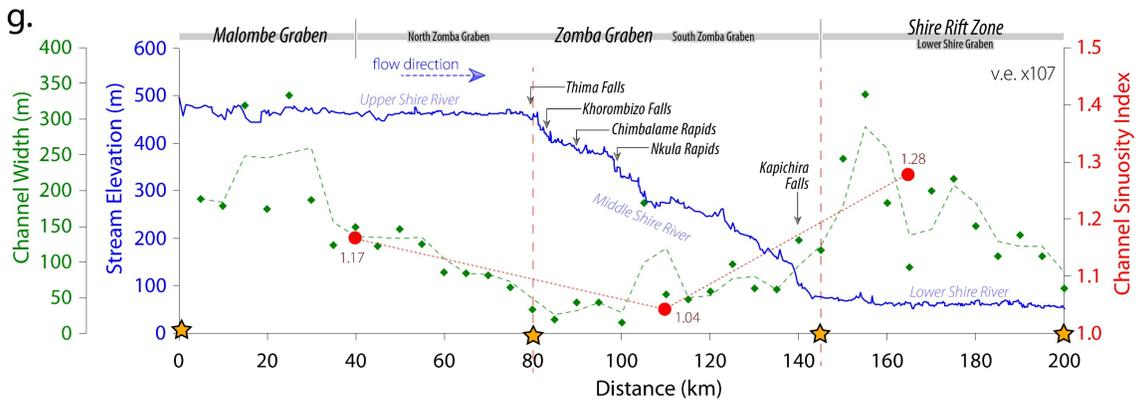
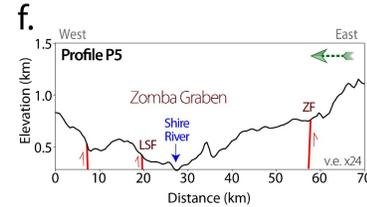
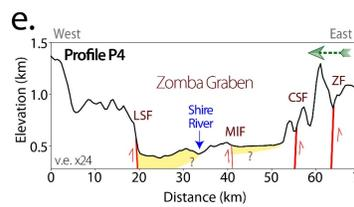
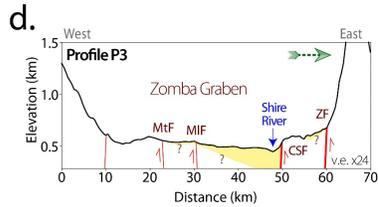
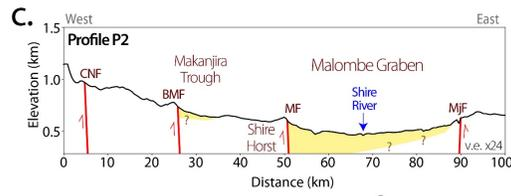
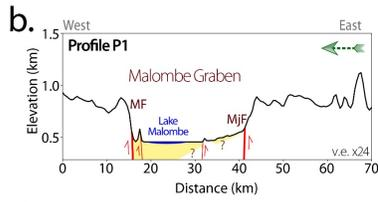
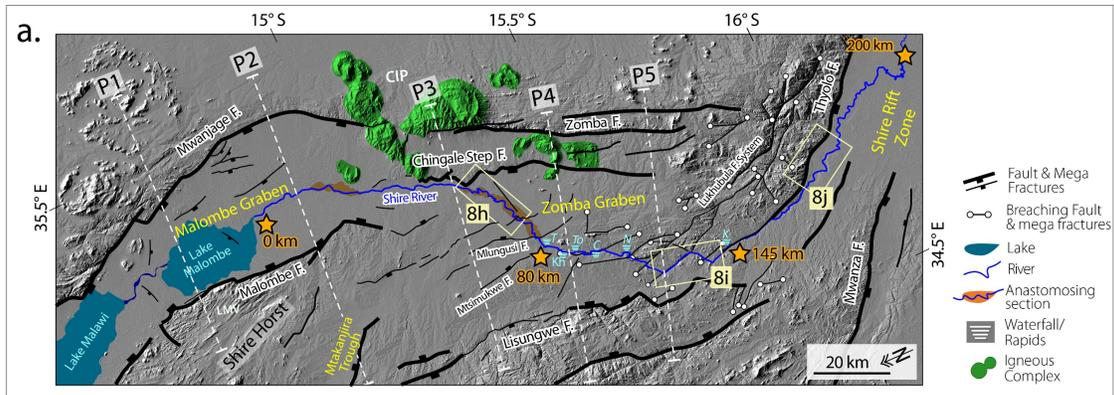
1992

1993

1994

1995

1996



1998 **Figure 8: Axial drainage system of the South Malawi–Shire Rift Interaction Zone, SMS-**  
1999 **RIZ.** (a.) Satellite digital elevation model (DEM) hillshade map overlaid with faults and the  
2000 axial stream channel (Shire River). C = Chimalame (or Machimbeya, or Chilemba) Rapids,  
2001 CIP = Chilwa Igneous Province, K = Kapichira Falls, Kh = Khorombizo (or Kholombidzo) Falls,  
2002 LMV = Lake Malombe Vents, N = Nkula Rapids, T = Thima Rapids, To = Toni Rapids. (b - f)  
2003 Rift-orthogonal topographic profiles showing a north to south variation in rift polarity and  
2004 the associated location of the Shire River. (g) Shire River stream profile, channel width, and  
2005 sinuosity index estimates. (h – j) Landsat TM false color composites (321RGB) of the (h)  
2006 Upper, (i) Middle, and (j) Lower courses of the Shire River. Overall, the unidirectionality of  
2007 flow and morphology of the axial stream across the rift interaction zone cross-over region,  
2008 linkage of interacting rift border faults by a cluster of breaching fault/fractures, exposure of  
2009 pre-rift basement at the rift-floor (Figure 8i), and an unequilibrated stream profile (Figure  
2010 8g) suggest a recent breaching of the rift interaction zone.

2011

2012

2013

2014

2015

2016

2017

2018

2019

2020

2021

2022

2023

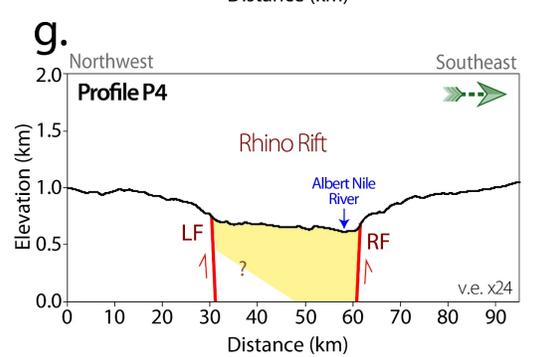
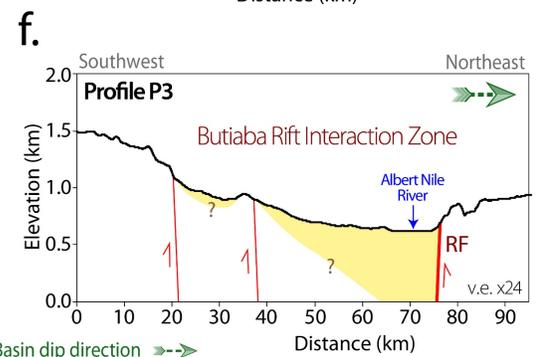
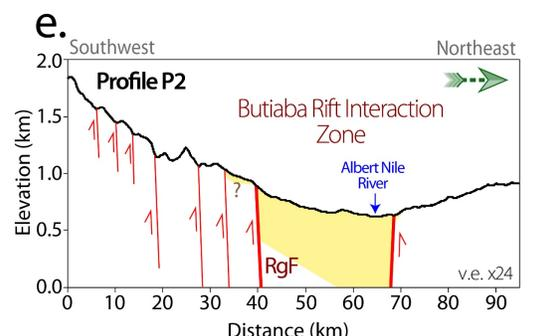
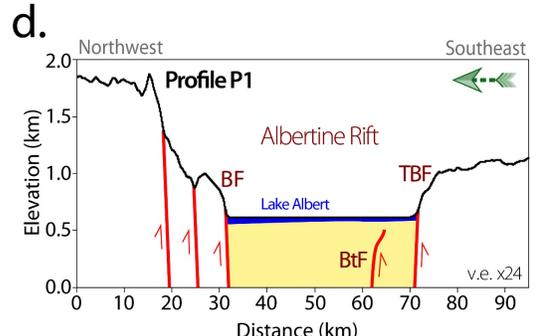
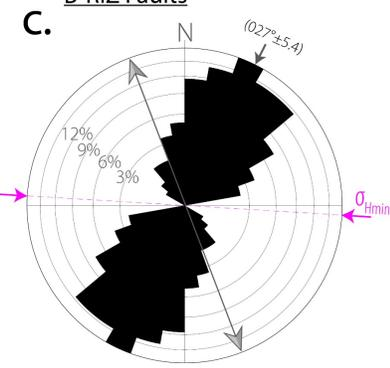
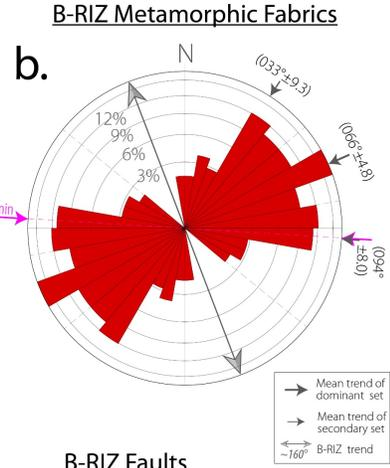
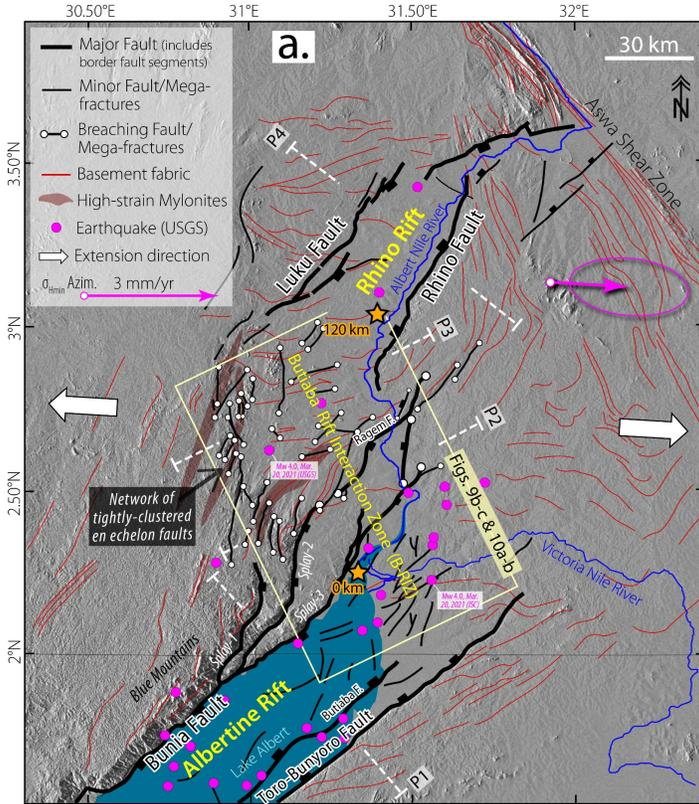
2024

2025

2026

2027

2028  
2029  
2030  
2031  
2032  
2033  
2034  
2035  
2036  
2037  
2038  
2039  
2040  
2041  
2042  
2043  
2044  
2045  
2046  
2047  
2048  
2049  
2050  
2051  
2052



2053 **Figure 9: Albertine–Rhino Rift Interaction Zone, AR-RIZ, a.k.a. Butiaba Rift Interaction**  
2054 **Zone, BRIZ (Underlapping Parallel Divergent RIZ).** (a.) Satellite digital elevation model  
2055 (DEM) hillshade map overlaid with interpretations of fault and basement fabrics in the  
2056 Albertine and Rhino Rifts. Fault lineaments are interpreted from satellite DEM and filtered  
2057 aeromagnetic data (this study; Supplementary Figure 3), and from seismic reflection data  
2058 (Simon et al., 2017). We also interrogated and included faults segments from other previous  
2059 studies (GTK Consortium, 2012; Westerhof et al., 2014; Katumwehe et al., 2015). The  
2060 locations of highly strained mylonites are obtained from Westerhof et al. (2014). Crustal  
2061 stretching velocity (green arrow) with 95% uncertainty ellipse is from Saria et al. (2014). (b  
2062 – c) Frequency-azimuth distribution of the basement fabrics (b) and faults (c) in the rift  
2063 interaction zone. (d - g) Rift-orthogonal topographic profiles showing a southwest to  
2064 northeast variation in rift polarity in relation to the location of the axial stream. BF = Bunia  
2065 Fault, BtF = Butiaba Fault, LF = Luku Fault; RF = Rhino Fault, RgF = Ragem Fault, TBF = Toro-  
2066 Bunyoro Fault. Note that the thickness of the rift sedimentary deposits shown in the  
2067 topographic profiles are not drawn to scale. Although, there is a discrepancy in the location  
2068 of the recent Mw4 earthquake as recorded in global earthquake catalogs, we note that the  
2069 two estimated locations are within the BRIZ.

2070

2071

2072

2073

2074

2075

2076

2077

2078

2079

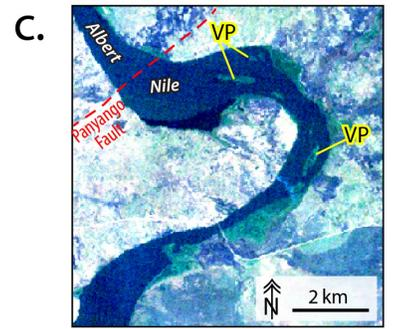
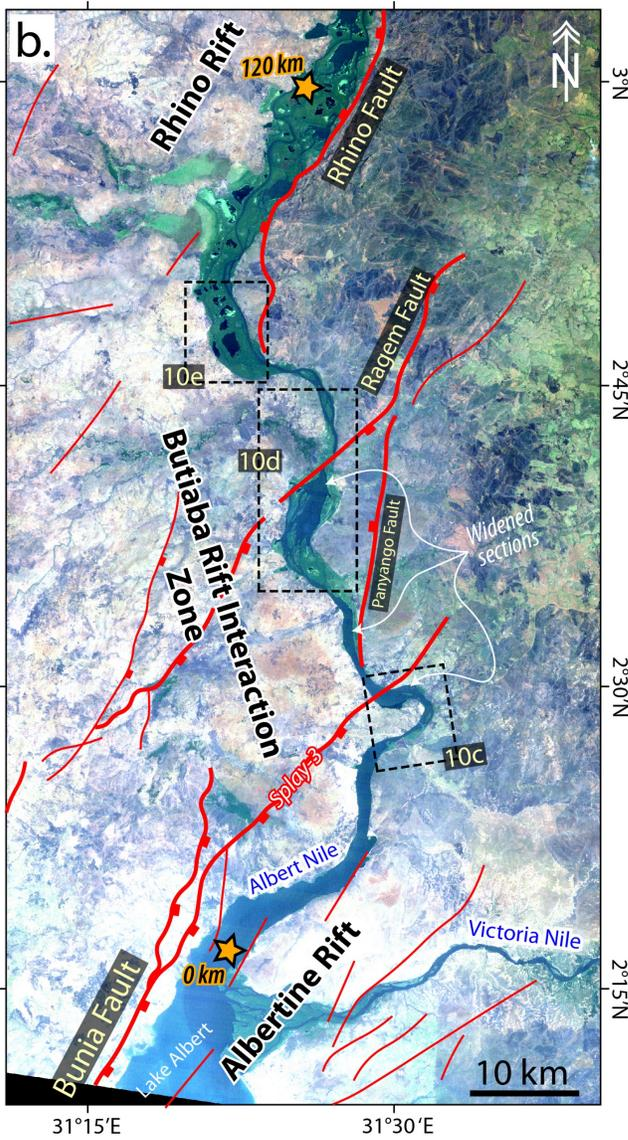
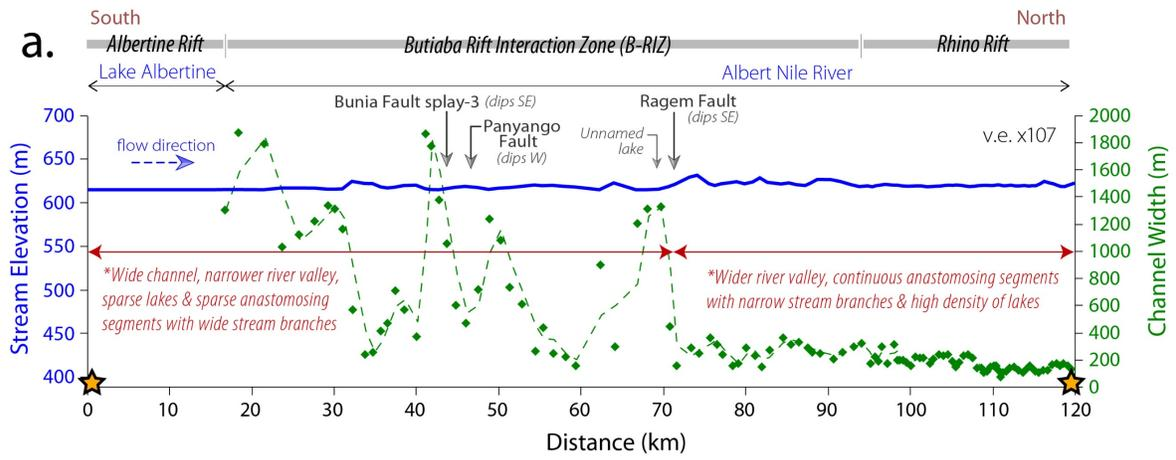
2080

2081

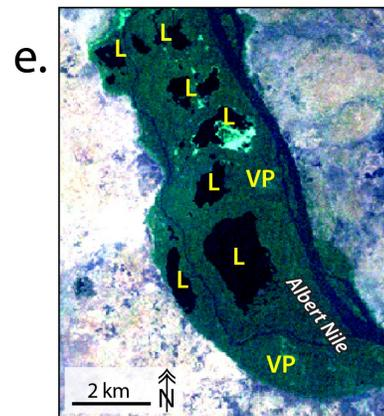
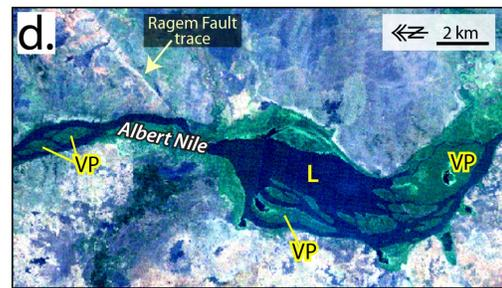
2082

2083

2084



VP = Vegetated point bar L = lake



2086 **Figure 10: Axial drainage system of the Albertine–Rhino Rift Interaction Zone (Butiaba**  
2087 **Rift Interaction Zone).** (a.) The Albert Nile River stream profile, and along-channel stream  
2088 width. At the anastomosing segments of the river, the profile represents a single branch of  
2089 the river with open waters (i.e., not covered by wetland vegetation). (b - e) Landsat TM false  
2090 color composite (321RGB) images showing the sinuous and anastomosing morphology of  
2091 the Albert Nile River within the rift interaction zone. L = Lake, VP = vegetated point bar.

2092

2093

2094

2095

2096

2097

2098

2099

2100

2101

2102

2103

2104

2105

2106

2107

2108

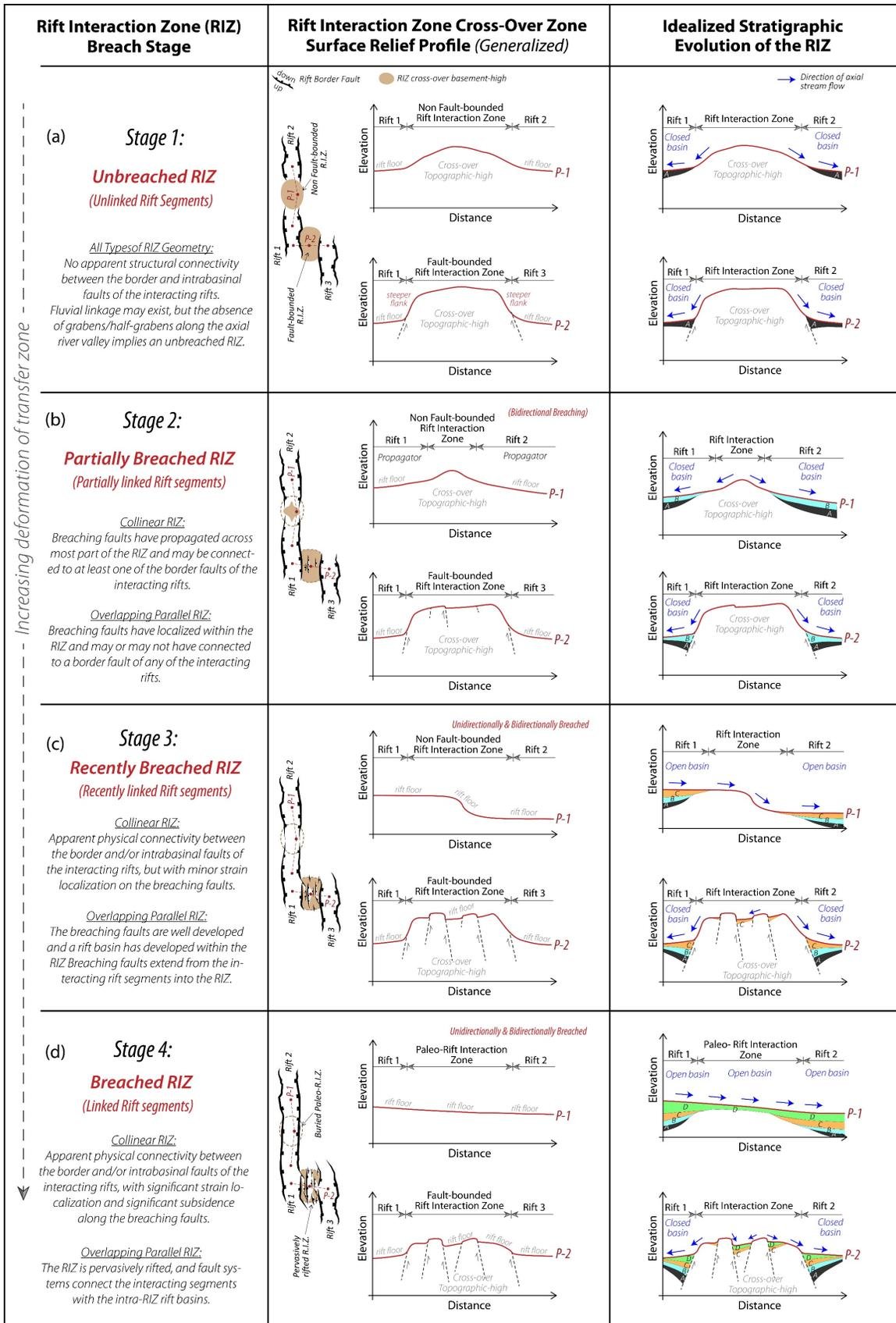
2109

2110

2111

2112

2113  
2114  
2115  
2116  
2117  
2118  
2119  
2120  
2121  
2122  
2123  
2124  
2125  
2126  
2127  
2128  
2129  
2130  
2131  
2132  
2133  
2134  
2135  
2136  
2137  
2138



2139 **Figure 11: Models of the stages of evolution of non-magmatic rift interaction zones.** (a –  
2140 d) Summary cartoons based on the general observations of breaching fault patterns, long-  
2141 wavelength topographic relief, and axial drainage patterns of rift interaction zones along the  
2142 western branch of the East African Rift System (WB-EARS). We present only the tip-to-tip  
2143 parallel and overlapping parallel divergent rift interaction zone geometries as examples, to  
2144 illustrate our observations and idealized models. The models assume: 1) a humid continental  
2145 setting, 2) orthogonal extension, 3) the erodibility of the pre-rift basement is relatively  
2146 uniform (in the case of the WB-EARS rift interaction zones studied), 4) sediment supply in  
2147 the interacting basins keeps up with strain rates on faults, and 5) no active dynamic topography  
2148 in the deforming rift interaction zone. The geometry of the breaching faults as presented, are  
2149 simplified and do necessarily indicate the kinematics of the breaching structures. Also, note  
2150 that the topographic relief shapes of Stages 2 (and possibly Stage 3) are implied to strongly  
2151 depend on the directionality of propagation of rift linkage assuming that basement  
2152 erodibility is uniform. Although our models are based on regions of active early-stage  
2153 (stretching phase) continental rifting in which at least one of the interacting rift pairs is  
2154 active, the observations are relevant for buried rift interaction zones in ancient rift settings.

2155

2156

2157

2158

2159

2160

2161

2162

2163

2164

2165

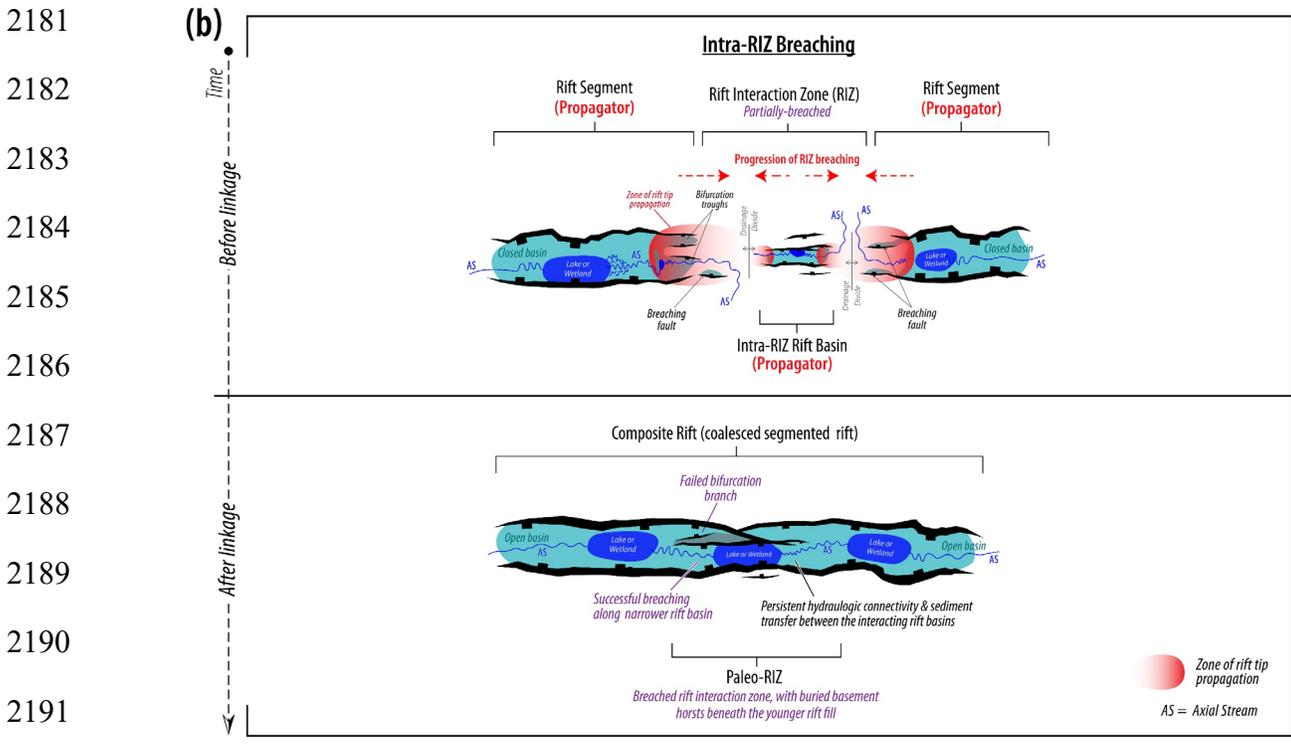
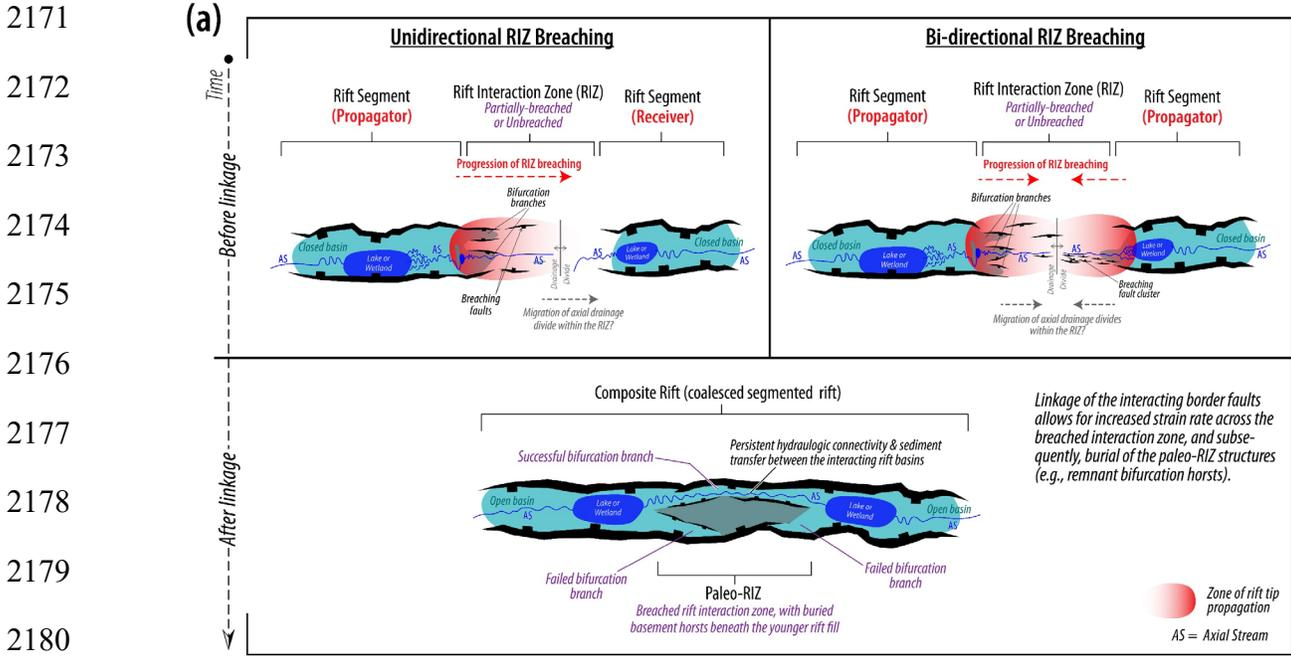
2166

2167

2168

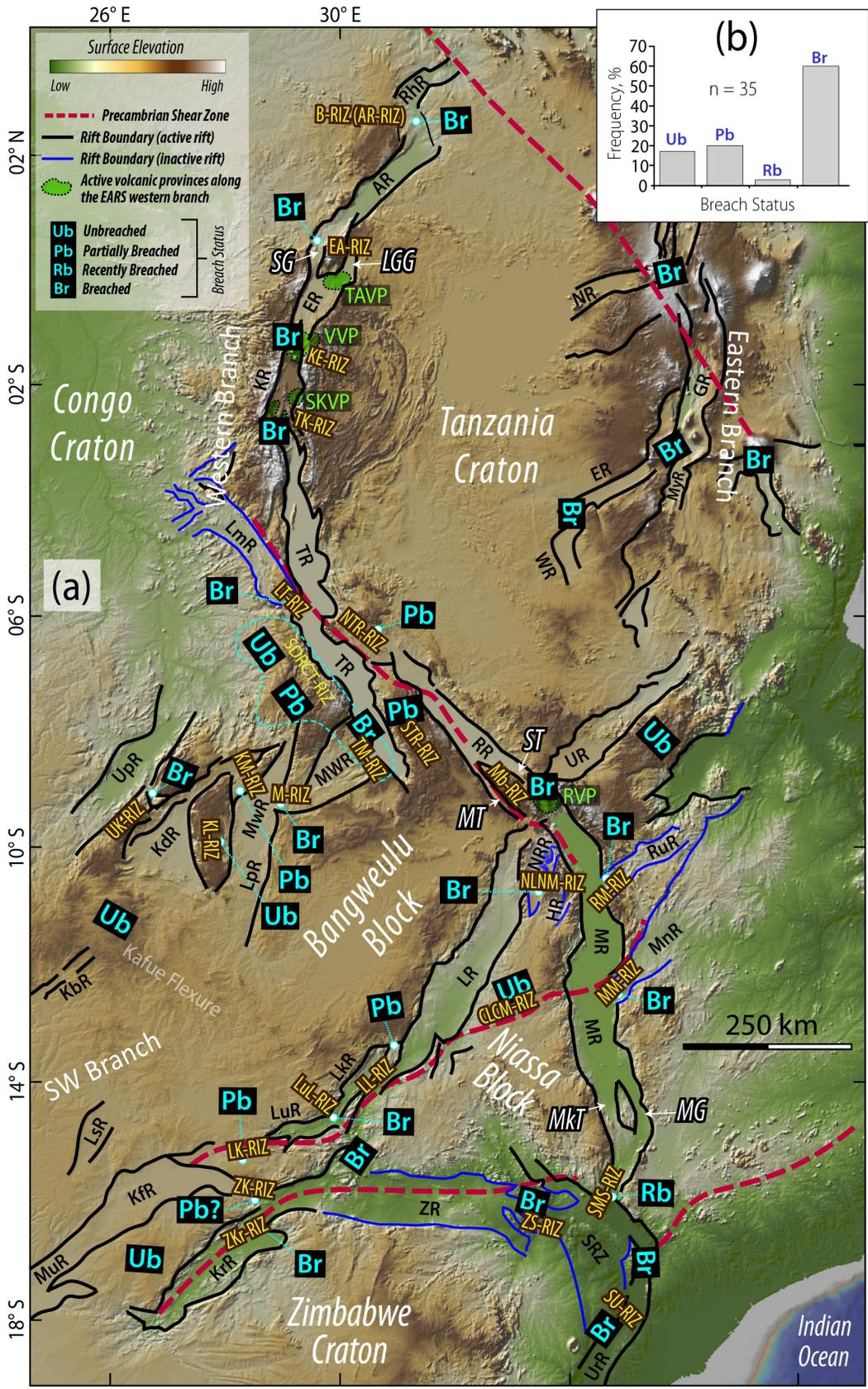
2169

2170



2193 **Figure 12: Directional propagation of rift interaction zone breaching, and rift-tip**  
 2194 **interactions.** Using an active collinear rift interaction zone as a simple example, these  
 2195 cartoons show directionality of rift interaction zone breaching and rift tip splay as an  
 2196 example of rift-tip interactions. Other rift tip interactions discussed in the study include  
 2197 border fault rotation and fault cluster networks.

2198  
 2199  
 2200  
 2201  
 2202  
 2203  
 2204  
 2205  
 2206  
 2207  
 2208  
 2209  
 2210  
 2211  
 2212  
 2213  
 2214  
 2215  
 2216  
 2217  
 2218  
 2219  
 2220  
 2221  
 2222  
 2223



2224 **Figure 13: *Breach-state of rift interaction zones in eastern Africa.*** (a) Map showing the  
2225 inferred breach state of the rift interaction zones along the western, SW, and SE branches of  
2226 the East African Rift System, inferred from the general conventions of rift interaction zone  
2227 cross-over structure and physiography proposed in this study. Also note that we  
2228 characterize all magmatic rift interaction zones as “breached” because of the lithospheric-  
2229 scale deformation associated with magmatism. SDRCT-RIZ = South DRC Rift Zone -  
2230 Tanganyika Rift Interaction Zone. See Figure 4a for the explanations of the abbreviated rift  
2231 and interaction zone labels. Map Source: Global Multi-Resolution Topography (GMRT) digital  
2232 elevation model (Ryan et al., 2009). (b) Histogram of the distribution of the inferred breach  
2233 states of the rift interaction zones in Figure 13a.

2234

2235

2236

2237

2238

2239